



Michigan Technological University
Create the Future Digital Commons @ Michigan Tech

Dissertations, Master's Theses and Master's
Reports - Open

Dissertations, Master's Theses and Master's
Reports

2012

Comparison of magnetic properties and petrography between dykes and lava flows from La Cienega, New Mexico and Thunder Bay area, Canada

Elise A. Desplas
Michigan Technological University

Follow this and additional works at: <https://digitalcommons.mtu.edu/etds>

 Part of the [Geology Commons](#)


Copyright 2012 Elise A. Desplas

Recommended Citation

Desplas, Elise A., "Comparison of magnetic properties and petrography between dykes and lava flows from La Cienega, New Mexico and Thunder Bay area, Canada", Master's Thesis, Michigan Technological University, 2012.

<https://doi.org/10.37099/mtu.dc.etds/317>

Follow this and additional works at: <https://digitalcommons.mtu.edu/etds>

 Part of the [Geology Commons](#)

COMPARISON OF MAGNETIC PROPERTIES AND PETROGRAPHY BETWEEN
DYKES AND LAVA FLOWS FROM LA CIENEGA, NEW MEXICO AND
THUNDER BAY AREA, CANADA

By

Elise A. Desplas

A THESIS

Submitted in partial fulfillment of the requirements for the degree of

MASTER OF SCIENCE

(Geology)

MICHIGAN TECHNOLOGICAL UNIVERSITY

2012

© 2012 Elise A. Desplas

This thesis, “Comparison of Magnetic Properties and Petrography between Dykes and Lava Flows from La Cienega, New Mexico and Thunder Bay area, Canada” is hereby approved in partial fulfillment of the requirements for the Degree of MASTER OF SCIENCE IN GEOLOGY

Department of Geological and Mining Engineering and Sciences

Signatures:

Thesis Advisor

Dr. Aleksey V. Smirnov

Department Chair

Dr. Wayne D. Pennington

Date

Table of content

List of Figures	v
List of Tables	x
Acknowledgment	xi
Abstract	xii
1. Introduction.....	1
2. Background.....	4
2.1. Virtual Dipole Moment.....	4
2.2. Basics of magnetism	6
2.3. Basics of SEM.....	10
3. Geological setting	12
3.1. Thunder Bay, Canada.....	12
3.2. La Cienega, New Mexico	13
4. Methods.....	16
4.1. Hysteresis properties	16
4.2. Thermomagnetic curves.....	18
4.3. Optical microscope	19
4.4. Scanning Electron Microscope	20

5.	Results / Discussion	21
5.1.	Hysteresis properties	21
	Thunder Bay, Canada.....	21
	La Cienega, New-Mexico	23
	Day-plot	24
5.2.	Thermomagnetic curves.....	27
	Thunder Bay, Canada.....	27
	La Cienega, New-Mexico	30
5.3.	Optical microscope	34
	Thunder Bay, Canada.....	34
	La Cienega, New-Mexico	45
5.4.	Scanning Electron Microscope	52
	Thunder Bay, Canada.....	52
	La Cienega, New-Mexico	59
6.	Conclusions.....	67
7.	References.....	69
8.	Appendices.....	74

List of Figures

Figure 2.1: VDM distribution obtained from dykes and lava flows.....	5
Figure 2.2: Age distribution of dykes and lava flows.....	5
Figure 2.3: Diamagnetic and paramagnetic material	6
Figure 2.4: Hysteresis loop for a ferromagnetic sample.....	7
Figure 2.5: Domain states in ferromagnetic grains.....	8
Figure 2.6: Fe-Ti oxides ternary diagram	9
Figure 2.7: Composition of titanomagnetite	10
Figure 2.8: Depth of the interaction of primary electron with sample atoms	11
Figure 3.1: DEM of the study area in Thunder Bay area.....	12
Figure 3.2: Schematic of the sampling locations	13
Figure 3.3: Field photo of La Cienega volcano	15
Figure 4.1: Photo of the AGM	16
Figure 4.2: Paramagnetic slope correction of hysteresis loop	17
Figure 4.3: Photo of the Kappabridge.....	18
Figure 4.4: Photo of the SEM JEOL 6400.....	20
Figure 5.1: Hysteresis loops of Thunder Bay lava flow	21
Figure 5.2: Hysteresis loops of Thunder Bay dyke	22
Figure 5.3: Hysteresis loops of La Cienega samples	23
Figure 5.4: Day-plot.....	25
Figure 5.5: Thermomagnetic curves of Thunder Bay samples	27
Figure 5.6: Thermomagnetic curves of Thunder Bay samples at different temperature ..	29

Figure 5.7: Thermomagnetic curves of La Cienega samples.....	30
Figure 5.8: Thermomagnetic curves of NM-CMB1 sample.....	32
Figure 5.9: Thermomagnetic curves of La Cienega samples at different temperatures ..	33
Figure 5.10: TB-CM1 optical microscope image, objective x10	34
Figure 5.11: TB-CM1 optical microscope image, objective x50	35
Figure 5.12: TB-CM2 optical microscope image, objective x5	36
Figure 5.13: TB-CM2 optical microscope image, objective x50	36
Figure 5.14: TB-CM3 optical microscope image, objective x5	37
Figure 5.15: TB-CM3 optical microscope image, objective x20	37
Figure 5.16: TB-CM3 optical microscope image, objective x20	38
Figure 5.17: TB-CM3 optical microscope image, objective x50	38
Figure 5.18: TB-CN1 optical microscope image, objective x5	39
Figure 5.19: TB-CN1 optical microscope image, objective x20	39
Figure 5.20: TB-CN1 optical microscope image, objective x100	40
Figure 5.21: TB-CN5 optical microscope image, objective x5	41
Figure 5.22: TB-CN5 optical microscope image, objective x20	41
Figure 5.23: TB-CN5 optical microscope image, objective x20	42
Figure 5.24: TB-CN5 optical microscope image, objective x10	42
Figure 5.25: TB-CN5 optical microscope image, objective x50.	43
Figure 5.26: TB-CN7 optical microscope image, objective x10	44
Figure 5.27: TB-CN7 optical microscope image, objective x50	44
Figure 5.28: NM-CM3A optical microscope image, objective x5	45

Figure 5.29: NM-CM3A optical microscope image, objective x10	45
Figure 5.30: NM-CM3A optical microscope image, objective x100	46
Figure 5.31: NM-CM3A optical microscope image, objective x50	46
Figure 5.32: NM-CMB1 optical microscope image, objective x5	47
Figure 5.33: NM-CMB1 optical microscope image, objective x20	47
Figure 5.34: NM-CMB1 optical microscope image, objective x100	48
Figure 5.35: NM-CMB2 optical microscope image, objective x10	49
Figure 5.36: NM-CMB2 optical microscope image, objective x50	49
Figure 5.37: NM-CMB3 optical microscope image, objective x5	50
Figure 5.38: NM-CMB3 optical microscope image, objective x50	50
Figure 5.39: NM-CMB3 optical microscope image, objective x50	51
Figure 5.40: BEI of TB-CM1 sample	52
Figure 5.41: BEI of TB-CM1 sample	53
Figure 5.42: BEI of TB-CN2 sample	55
Figure 5.43: BEI of TB-CN3 sample	56
Figure 5.44: BEI of TB-CN3 sample	57
Figure 5.45: BEI of TB-CN5 sample	58
Figure 5.46: BEI of NM-CM3A sample	60
Figure 5.47: BEI of NM-CMB1 sample	61
Figure 5.48: BEI of NM-CMB1 sample	63
Figure 5.49: BEI of NM-CMB2 sample	64
Figure 5.50: BEI of NM-CMB2 sample	65

Figure 8.1: Appx 8.1 EDS spectra TB-CM1 darkest phase.....	74
Figure 8.2: Appx 8.1 EDS spectra TB-CM1 lightest phase.....	75
Figure 8.3: Appx 8.2 EDS spectra TB-CN2 homogeneous dark phase.....	76
Figure 8.4: Appx 8.2 EDS spectra TB-CN2 homogeneous light phase	77
Figure 8.5: Appx 8.2 EDS spectra TB-CN2 dark exsolutions.....	78
Figure 8.6: Appx 8.3 EDS spectra TB-CN3 darkest phase	79
Figure 8.7: Appx 8.3 EDS spectra TB-CN3 lightest phase	80
Figure 8.8: Appx 8.4 EDS spectra TB-CN3 darkest phase	81
Figure 8.9: Appx 8.4 EDS spectra TB-CN3 medium phase.....	82
Figure 8.10: Appx 8.4 EDS spectra TB-CN3 lightest phase	83
Figure 8.11: Appx 8.5 EDS spectra TB-CN5 darkest phase	84
Figure 8.12: Appx 8.5 EDS spectra TB-CN5 lightest phase	85
Figure 8.13: Appx 8.5 EDS spectra TB-CN5 exsolutions.....	86
Figure 8.14: Appx 8.6 EDS spectra NM-CM3A darkest phase.....	87
Figure 8.15: Appx 8.6 EDS spectra NM-CM3A medium phase	88
Figure 8.16: Appx 8.6 EDS spectra NM-CM3A lightest phase	89
Figure 8.17: Appx 8.7 EDS spectra NM-CMB1 darkest mineral.....	90
Figure 8.18: Appx 8.7 EDS spectra NM-CMB1 lightest mineral	91
Figure 8.19: Appx 8.8 EDS spectra NM-CMB1 darkest phase.....	92
Figure 8.20: Appx 8.8 EDS spectra NM-CMB1 lightest phase.....	93
Figure 8.21: Appx 8.9 EDS spectra NM-CMB1 dark, large exsolution.....	94
Figure 8.22: Appx 8.9 EDS spectra NM-CMB1 dark, thin exsolutions.....	95

Figure 8.23: Appx 8.9 EDS spectra NM-CMB1 lightest phase.....	96
Figure 8.24: Appx 8.10 EDS spectra NM-CMB2 darkest phase.....	97
Figure 8.25: Appx 8.10 EDS spectra NM-CMB2 medium phase	98
Figure 8.26: Appx 8.10 EDS spectra NM-CMB2 fractured, lightest phase	99
Figure 8.27: Appx 8.11 EDS spectra NM-CMB2 darkest phase.....	100
Figure 8.28: Appx 8.11 EDS spectra NM-CMB2 second darkest.....	101
Figure 8.29: Appx 8.11 EDS spectra NM-CMB2 second lightest phase	102
Figure 8.30: Appx 8.11 EDS spectra NM-CMB2 lightest phase.....	103
Figure 8.31: Appx 8.12 Copyright permission for Figure 3.1	104
Figure 8.32: Appx 8.12 Copyright permission for Figure 3.3	104

List of Tables

Table 3.1: Locations of La Cienega samples	14
Table 4.1: Sample weights for the thermomagnetic analysis.....	19
Table 5.1: Magnetic properties ^a of rock samples.....	24

Acknowledgment

I would like to thank my advisor Aleksey Smirnov without whom this project could not be possible, Gregory Waite and Jaroslaw Drelich for being part of my committee, all members on the INVOGE program for permitting me this great experience in Michigan Tech. Of course this study would not be the same without the guidance, support and help from Elisa Piispa. I also would like to thank Kari Anderson for the reviewing in a very short time, Patrick Bowen and Felicia Nip for their help using the SEM, Ruth Kramer for her guidance during the polishing, and all other person in Michigan Tech who made this year a unique experience.

Abstract

Data on the evolution of geomagnetic paleointensity are crucial for understanding the geodynamo and Earth's thermal history. Although basaltic flows are preferred for paleointensity experiments, quickly cooled mafic dykes have also been used. However, the paleointensity values obtained from the dykes are systematically lower than those from lava flows. This bias may originate from the difference in cooling histories and resultant magnetic mineralogies of extrusive and intrusive rocks. To explore this hypothesis, the magnetic mineralogy of two feeder dyke-lava flow systems, from Thunder Bay (Canada) and La Cienega (New-Mexico), has been studied using magnetic and microscopy methods. Within each system, the flow and dyke show different stages of deuteric oxidation of titanomagnetite, but the oxidation stages also differ between the two systems. It is concluded that the tested hypothesis is viable, but the relationships between the magnetic and mineralogical properties of flows and dykes are complex and need a further investigation.

1. Introduction

Data on the long-term evolution of the strength of Earth's magnetic field (paleointensity) are crucial for understanding the evolution of the geodynamo and thermal history of our planet. The ideal objects for paleointensity determinations are quickly-cooled basaltic lava flows. However, suitable basaltic sequences are not always available for investigations due to erosion, weathering, deformation, and/or metamorphism hindering the preservation and measurement of paleointensity signal. As an alternative to basaltic flows, quickly cooled shallow intrusions such as mafic dykes and sills have been increasingly used for paleointensity studies, especially for the Precambrian time. However, the paleointensity values obtained from the dykes/sills have been noticed to be systematically lower than those obtained from lava flows. This difference is observed from very young as well as very old rocks and therefore cannot be explained by the differential alteration of older rocks. The reason for the paleofield discrepancy remains unclear and represents one of the outstanding problems in paleomagnetism. Here, a hypothesis is proposed that the difference in paleofield values between the extrusive and intrusive rocks originates from the differences in their cooling histories and resultant magnetic mineralogies.

The magnetic properties of basaltic rocks are dominated by the amount and type of primary Fe-Ti oxides. These oxides have a composition range of two solid solutions (Buddington and Lindsey 1964; Carmichael and Nicholls 1967): the series of titanomagnetite ($\text{Fe}_{3-x}\text{Ti}_x\text{O}_4$) with a composition between magnetite (Fe_3O_4) and ulvospinel (Fe_2TiO_4) and the series of titanohematite ($\text{Fe}_{2-x}\text{Ti}_x\text{O}_3$) with a composition between hematite (Fe_2O_3) and ilmenite (FeTiO_3). The average composition of titanomagnetite formed during initial crystallization is around $x = 0.6$, denoted TM60 (Petersen 1976).

The composition of titanomagnetite can be determined by measuring its Curie temperature, T_c . The study of synthetic titanomagnetites (Ishikawa and Akimoto 1957)

showed that the Curie temperature of titanomagnetite decreases with the amount of titanium; pure magnetite (TM0) has a Curie temperature of $\sim 577^{\circ}\text{C}$ and ulvöspinel around -152°C (Haggerty 1978; Lattard et al. 2006). The titanohematite series exhibits a similar behavior with a range of Curie temperatures between 677°C for hematite and -218°C for ilmenite (Ishikawa and Akimoto 1957).

Titanomagnetite is a metastable composition and has a strong tendency to be decomposed and/or oxidized to more stable phases such as magnetite, ilmenite, or hematite (Verhoogen 1962). The oxidation processes occurs differently at high and low temperatures. Titanohematites, rhombohedral minerals, can be produced by the cation-deficient oxidation of titanomagnetite which has cubic symmetry (Dunlop and Özdemir 1997). Alternatively, at high temperatures (above 500°C), titanomagnetite may produce magnetite and ilmenite, increasing the Curie temperature of the rock (Akimoto et al. 1957; O'Reilly and Banerjee 1967; Lewis 1968). The resultant magnetite and ilmenite are often observed as a set of exsolved structures (lamellae) with different appearances described by Haggerty (1991): Sandwich type, Trellis type, lamellae, composite type, depending of the stage of oxidation and composition of minerals. At a higher stage of high-temperature oxidation, ilmenite and magnetite produce hematite, increasing the Curie temperature on magnetic minerals (Petersen 1976).

At low temperatures, below 300°C , the oxidation of titanomagnetite produces titanomaghemite ($(\text{Fe}, \text{Ti}, \square)_3\text{O}_4$), where \square represents a vacant place on the structure of the mineral), causing a small increase of the Curie temperature (Schult 1965 and 1968; Readman and O'Reilly 1972; Petersen 1976; Bleil and Petersen 1979). By affecting the magnetic properties of a rock, these oxidations may affect the ability of rock to record, preserve, or reveal the paleointensity information. The high-temperature, deuteric oxidation often occurs during the initial cooling of lava, however, its final oxidation stage depends on the cooling rate among other parameters. Since the cooling rates for lava flows and dykes are different, one can expect a difference in the resultant magnetic mineral assemblages even for the same initial composition, oxygen fugacity, and other

characteristics of magma. The difference in magnetic mineralogy can in turn affect the paleointensity measurements.

A lava flow connected to its feeder dyke represents an ideal object to study this problem because both the lava and dyke should have nearly identical initial composition and be emplaced at the same time and place, hence recording the same paleointensity value. However, until now, no study comparing the magnetic and mineralogical properties of a lava flow connected to its feeder dyke has been conducted. As a first step towards resolving the systematic discrepancy between mafic dykes and basaltic flows in terms of paleointensity, the magnetic properties and mineralogy of two dyke-flow systems, from Thunder Bay, Canada and La Cienega, New-Mexico, have been studied using a variety of magnetic measurement techniques as well as reflected-light optical and scanning electron microscopy.

2. Background

2.1. Virtual Dipole Moment

Under the assumption of geocentric axial dipole, the geomagnetic inclination I is related to the latitude λ , the magnetic co-latitude θ_m , and the north and vertical down component of the field intensity B by the equation:

$$\tan I = \frac{B_v}{B_n} = 2 \cos \theta_m = 2 \tan \lambda$$

In order to account for the latitudinal dependence of field strength, the paleointensity is usually presented in terms of virtual dipole moment (VDM) using the following relationship:

$$VDM = \frac{\frac{4\pi}{\mu_0} r^3 B}{\sqrt{1 + 3 \cos^2 \theta_m}}$$

where B is measured paleointensity, r is the Earth radius, and μ_0 is the magnetic permeability of free space.

Figure 2.1 shows all published VDM values measured from basaltic flows and mafic dykes (the data from basaltic glass and single crystals have been excluded). Although the total number of data points representing the dykes is much smaller than those representing the flows, a systematic low-field bias of the “dyke” results is obvious. The bias does not depend on the age of rocks and hence cannot be explained by differential geological alteration of older rocks.

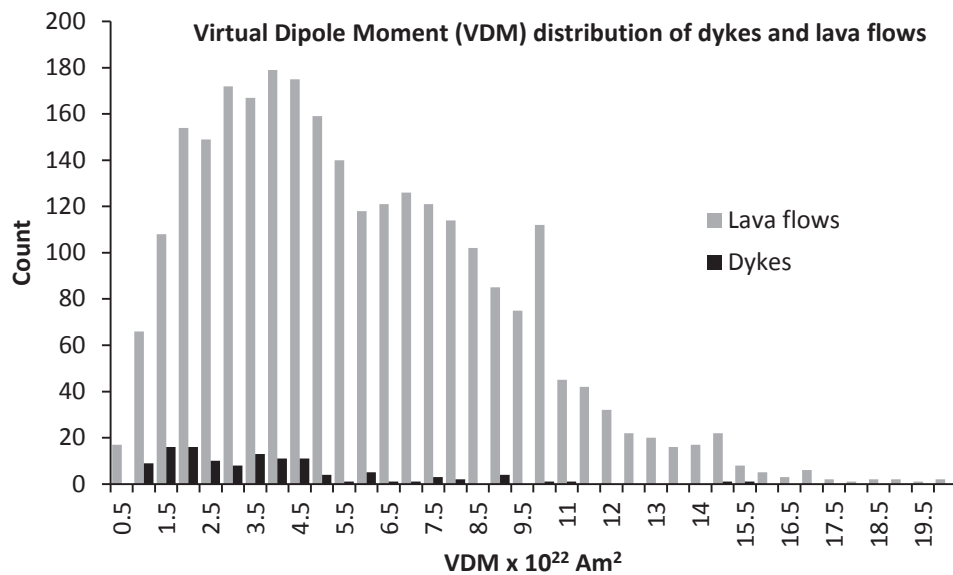


Figure 2.1: Virtual Dipole Moment (VDM) distribution obtained from dykes (black bars) and lava flows (grey bars).

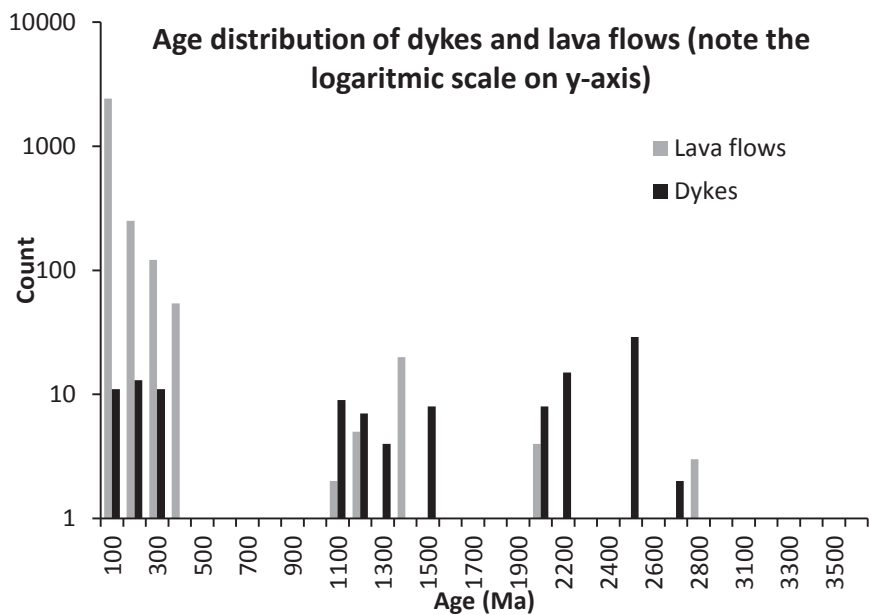


Figure 2.2: Semi logarithmic graph of the age distribution of dykes (black bars) and lava flows (grey bars) shown in Figure 2.1.

Figure 2.2 demonstrates that mafic dykes are increasingly used for paleointensity determination for older times. Notably, most of the paleointensity results for the Precambrian are obtained from mafic dykes. Therefore, it is very important to understand the processes that may affect the paleointensity record in mafic dykes.

2.2. Basics of magnetism

All materials are magnetic due to electron spin (magnetic moment) and electron motion. Magnetism is subdivided into induced and permanent magnetization. Induced magnetization (M) is related to the external field (noted B on this study) by the equation:

$$M = \kappa B$$

where κ is the magnetic susceptibility of the material being studied.

Because M and B have the same unit in SI (A/m), κ is dimensionless. If κ is negative, the material is diamagnetic (Figure 2.3a) and if κ is positive, the material is paramagnetic (Figure 2.3b).

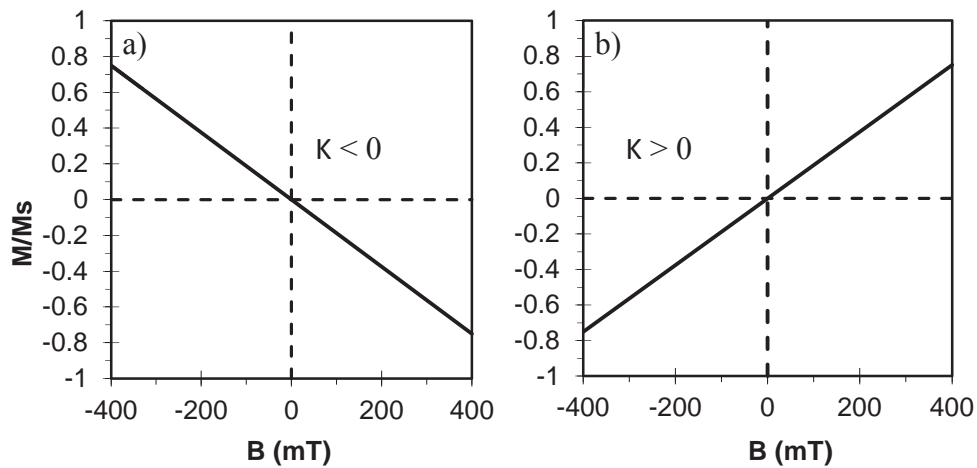


Figure 2.3: Example of (a) diamagnetic and (b) paramagnetic material response to an external magnetizing field B . M is the magnetization. Figures from Tauxe (2009), redrawn from Tauxe (1998).

In addition to the reversible linear negative and positive magnetic responses, a third fundamental type exists: ferromagnetism (Figure 2.4). Unlike paramagnetic materials, the adjacent atomic moments in ferromagnetic material interact strongly. This is because the atoms in ferromagnetic substances are more tightly packed and exhibit a higher density of valence electrons, which cause exchange forces between them. The strong coupling of atomic moments results in alignment into magnetic domains, which stay aligned even in absence of an applied field. The magnetization path in a changing external field is called a hysteresis loop (Figure 2.4) and gives indirectly information about the size of magnetic grains. This loop defines four basic parameters:

- 1) the maximum saturation magnetization: M_s
- 2) the remanent magnetization of the sample in zero field or saturation remanence: M_r
- 3) the field needed to obtain zero magnetization on the sample or coercive field: B_c
- 4) the counter field needed to remove the saturation remanence (M_r) or coercivity of remanence: B_{cr}

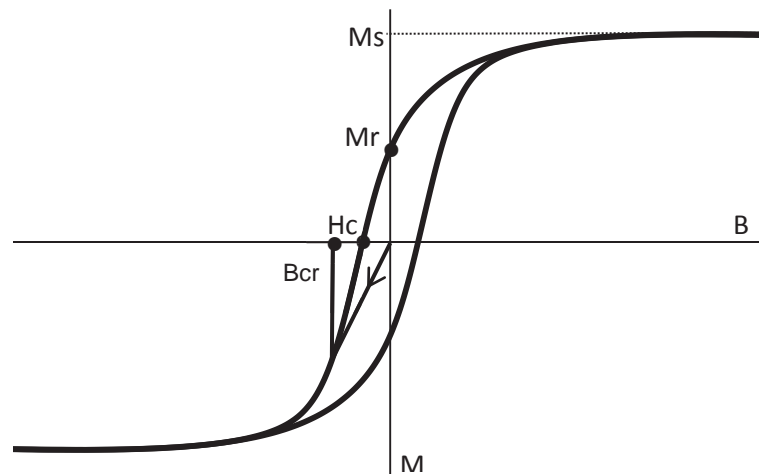


Figure 2.4: An example of a hysteresis loop for a ferromagnetic sample (M = magnetization, B = the applied field, B_c = the coercive force, M_r = the saturation remanent magnetization, M_s = the saturation magnetization, and B_{cr} = coercivity of remanence).

As said previously, the hysteresis loop gives information about the size of the grain. In reality, it gives information about the number of domain within magnetic crystals. Because the atomic magnetic moments align with the field materials, a small permanent magnetization are strongly magnetized when exposed to a weak magnetic field. Ferrimagnetism is a particular case of ferromagnetism presenting two oppositely directed spin moments with unequal magnitudes.

Figure 2.5 shows three general magnetic domain states in ferromagnetic materials: a) single domain, b) pseudo-single domain, c) and the multi domain. A single domain (SD) state is when the entire particle is uniformly magnetized (Figure 2.5a). The SD grains carry the most stable magnetization record. When there is more than one unique direction, it is multi domain (MD) (Figure 2.5c) with a domain wall separating each part. This configuration is magnetically less stable. With a few domains, such as in pseudo-single domain (PSD) grains (Figure 2.5b), the magnetization is almost as stable as in SD particles. According to Day et al. (1977), the proposed limit for the SD is $M_{rs}/M_s = 0.5$ and $B_{cr}/B_c = 1.5$. These values hold truth for titanomagnetites. The limit between the PSD and the MD is more complicated to determine. Day et al. (1977) assumed that the MD limits are defined by the values $M_{rs}/M_s = 0.05$ and $B_{cr}/B_c = 4$.

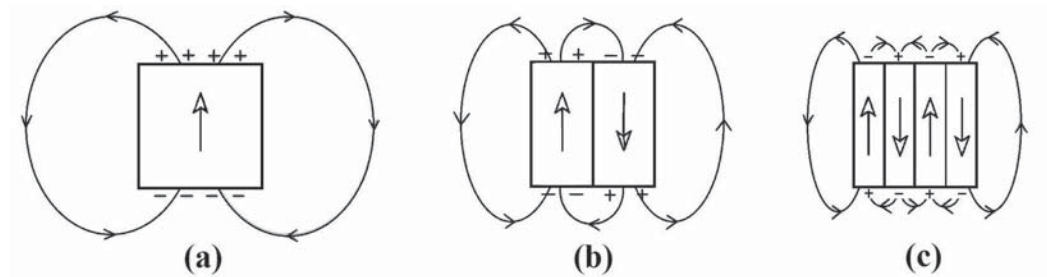


Figure 2.5: Possible domain states in ferromagnetic grains: a) Single domain, b) Pseudo-single domain (just few domains), and c) Multi domain.

Depending of the nature of the magnetism, susceptibility can be a function of temperature. Diamagnetism is independent of the temperature while paramagnetism is proportional to temperature. Ferromagnetism decreases with increasing temperature until becoming zero at its Curie temperature (Tauxe 2009). Beyond the Curie temperature, ferromagnetic materials become paramagnetic. The Curie temperature is a unique characteristic of every ferromagnetic material.

The most common ferromagnetic minerals are Fe-Ti oxides with a variable composition in Fe^{2+} , Fe^{3+} , and Ti^{4+} . These compositions are often drawn on a ternary diagram (Figure 2.6) with normalization to one cation (Butler 2004). The end-members on the diagram are hematite (Fe_2O_3), wustonite (FeO), and rutile (TiO_2). Thereby, the increase of the ferric (Fe^{3+}) to ferrous (Fe^{2+}) iron ratio as the decrease of oxygen is indicated by the horizontal position from left to right (Tauxe 2009). The amount of titanium increases from the bottom to the top of the triangle.

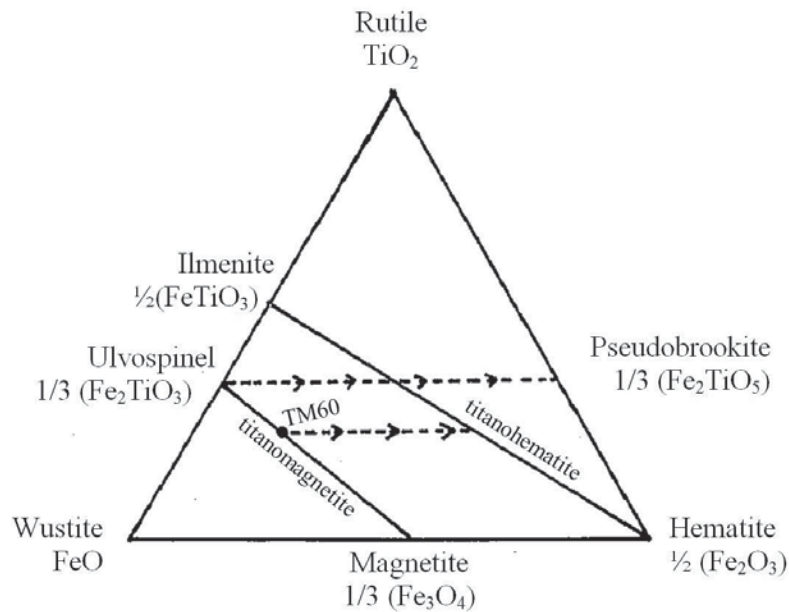


Figure 2.6: TiO_2 – FeO – Fe_2O_3 ternary diagram. Solid lines are solid solution series of titanomagnetite and titanohematite and dotted lines indicate an increase in oxidation (Redrawn after Butler (2004); Tauxe (2009)).

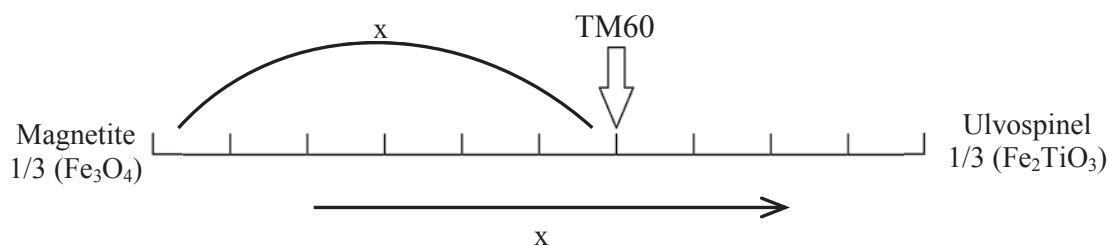


Figure 2.7: Composition of titanomagnetite between magnetite and ulvospinel composition.

Because the ternary diagram is normalized to one cation, a change from the left to the right corresponds to an oxidation of minerals, represented in Figure 2.6 by dotted lines. The composition of titanomagnetite ($\text{Fe}_{3-x}\text{Ti}_x\text{O}_4$) vary from magnetite to ulvospinel, with x indicating the amount of titanium on the mineral (Figure 2.7). For example, when x is equal to 0.6, the mineral has a composition $\text{Fe}_{2.4}\text{Ti}_{0.6}\text{O}_4$ and is called TM60 (Petersen 1976).

2.3. Basics of SEM

Scanning Electron Microscope (SEM) was used in order to identify Fe-Ti oxide grains and their composition. In SEM, a focused beam of electrons bombard the sample. The trajectory of bombarding electrons changes by interaction between the electrons and atoms.

Secondary electrons (SE) are a result of collision between the primary beam electrons and atoms. The emitted electrons are ionized with a low energy. Because of this low energy, the interaction is concentrated on the surface of the sample and depends mostly on the topography. The back-scattered electrons (BSE) are a result of an influence on the trajectory of the electron by the core of an atom. There is a small loss of energy permitting a depth intrusion of the beam electron. Because of this interaction with the nucleus, BSE imaging is sensitive to the atomic number of the element. Heavier atoms reflected more BSE. A detector collects emitted electrons in order to translate the signal into an image. The more electrons the detector receives, the stronger the signal is. This phenomenon is observed on a SEM image through a range of gray depending on the

composition. A dark gray represents a weak signal corresponding to lighter elements, and lighter grey correspond to heavier elements such as Fe or Ti.

The Energy Dispersive X-ray Spectrometer (EDS) is an attachment to SEM which measure X-ray produced by a primary or back-scattered electron which collides with an electron bound to the atom. If the energy of the primary electron is sufficient, the bound electron is emitted, releasing an atom in an excited state. An electron in a higher energy level takes the place of the emitted electron, giving off a photon in the X-ray spectrum. These X-rays are dependent of the chemical composition of the target atom permitting a quantitative elemental analysis of the sample at a known location.

During secondary electron (SE) analysis, the primary electrons interact within the surface of a sample. In contrast, when doing BSE or EDS, the primary electrons interact within a deeper volume of the sample (Figure 2.8). These techniques permit qualitative and quantitative approximations of the composition based on the hypothesis that the average composition does not change with the depth. In order to eliminate the effect of silicate matrix on the composition measurement, care was taken that the grain was thick enough for analysis. Because of difficulties in verifying the depth of a mineral, EDS interpretations are not precise but give, nevertheless, an idea about the composition of different phases.

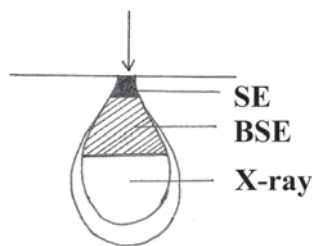


Figure 2.8: Depth of the interaction of primary electron with sample atoms. SE = secondary electron, BSE = back-scattered electron (after Goldstein and Yakowitz 1975; Loyd 1987).

3. Geological setting

3.1. Thunder Bay, Canada

The Thunder Bay site is located on the north shore of Lake Superior, within the North America's Midcontinental Rift System (MRS). This rift is represented by a series of extrusive and intrusive rocks emplaced in the late Mesoproterozoic from ~1150 Ma to ~1080 Ma (Klewin and Shirey 1992).

The Thunder Bay samples for this study were obtained from Elisa Piispa (Michigan Technological University) who had collected the samples during summer 2010 for a paleomagnetic study. A six to seven meter wide dyke appears to be a feeder to small lava flow two meter wide. The lava and the dyke carry stable paleomagnetic directions similar to these of the Logan sills (Piispa et al. 2011). The Logan sills are abundant in Thunder Bay area and have been dated $114.7 \text{ Ma} \pm 1.1 \text{ Ma}$ (Heaman et al. 2007).

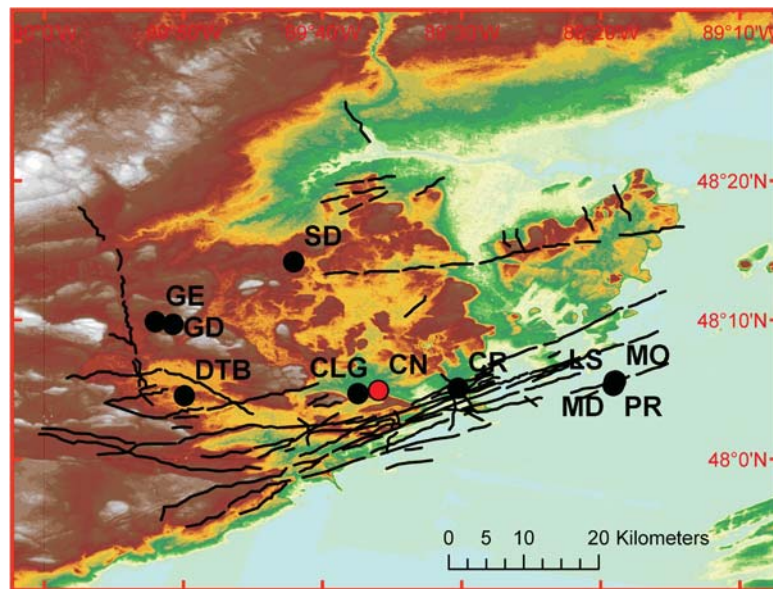


Figure 3.1: Digital Elevation Model (DEM) of the study area shows that some dykes can be traced based on the elevation in Thunder Bay area. The red circle shows the location of the dyke and lava flow. (By Piispa et al. (2011), Copyright permission seen in Appendix 8.12)

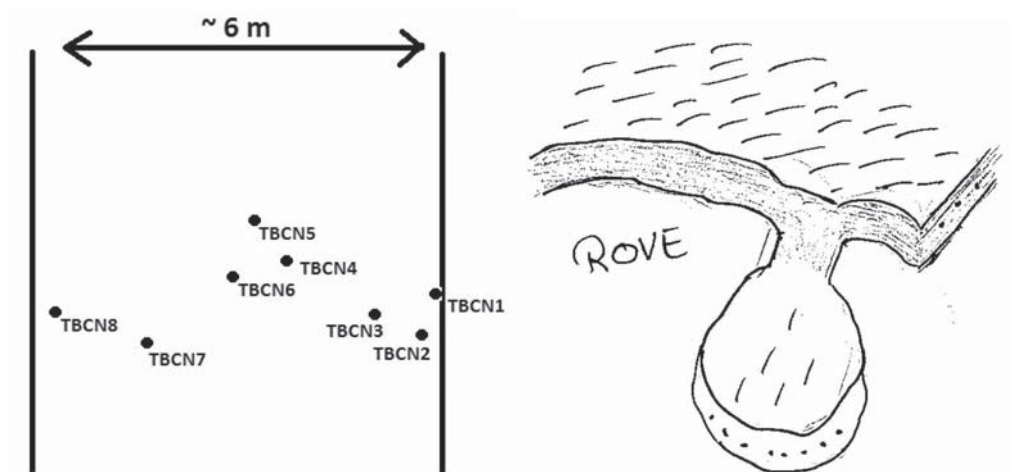


Figure 3.2: Relative positions of the sampling locations in the dyke and lava flow from the Thunder Bay area.

The location of the site is N 48.08214°, W 89.5996° (Figure 3.1). Eight samples (TB-CN1/TB-CN8) were drilled across the width of the dyke (Figure 3.2). Sample TB-CN1 is the closest to the western margin of the dyke and TB-CN8 is in the eastern margin of the dyke. The lava samples are TB-CM1/TB-CN3. Lava samples were taken at around the same distance to the dyke (15m). Macroscopically, dyke and lava samples are black basaltic rocks. The samples from the dyke center are finer grained than the lava flow samples and the samples from the dyke margin do not have visible minerals.

3.2. La Cienega, New Mexico

The junction of the Gulf of California and the western Mexican Volcanic Belt (MVB) on the Mexican coast causes two tectonic regimes, a subduction zone and Rio Grande rift (Kelley 1952). The subduction of the Rivera plate caused an uplift of the western Mexico during late Cenozoic and formation of volcanoes (Richter 1997). La Cienega is a shield volcano from the lower Pleistocene ~2.2 Ma located within the MVB (Bachman and Mehnert 1978; Richter et al. 1997 and 2012). Because of its subducting slab origin, erupted rocks are enriched in subduction-related magmas by the chemical

change of the convecting asthenosphere by entrained pelagic sediments (Baldrige 1978; Arculus and Powell 1986; Duncker et al. 1991) Three main type of rocks are present in this area which are hawaiiite, andesite and basaltic andesite according to Irvine and Baragar (1971) classification (Aubele 1979).

Five samples were collected from La Cienega by Marine Foucher (New Mexico Highlands University) during fall 2011(Figure 3.3). NM-CM3A is the feeder dyke and NM-CMvS is a sample from the vent of this dyke. Three samples were collected from the lava flow. NM-CMB1 is the closest to the dyke (~60m), NM-CMB2 further (~67m) and NM-CMB3 furthest (~81). The exact locations for each sample are shown in Table 3.1.

Table 3.1:
Locations of La Cienega samples

Sample	latitude	longitude	Distance from the dyke (m)
NM-CM3A	35.6174771	-106.1395635	/
NM-CMvS	35.6170736	-106.1397709	~50
NM-CMB1	35.6169497	-106.1395541	~60
NM-CMB2	35.6168912	-106.1395239	~67
NM-CMB3	35.6167582	-106.1395589	~81



Figure 3.3: Field photograph of the south of La Cienega volcano. The arrow shows the samples location. (By Foucher (2012), Copyright permission seen in Appendix 8.12)

Rocks from this site contain numerous vesicles and some macroscopic minerals. Sample NM-CM3A has noticeable alteration visible by brown rims around the minerals. The matrix is light gray. Sample NM-CMvS is not a homogeneous rock. Some parts have more vesicles and the minerals have a big range of sizes. Minerals within this sample also have a large color range suggesting that the rock underwent complicated mixing and solidification. Samples NM-CMB1, NM-CMB2, and NM-CMB3 are from the same lava flow but sample NM-CMB1 is visually different. This sample closest to the dyke is of a lighter color than samples NM-CMB2 and NM-CMB3. The rock has vesicles and large altered minerals. Samples NM-CMB2 and NM-CMB3 are very dark compared to sample NM-CMB1 and contain some rusty lineation, likely caused by alteration of the rock rich in iron.

4. Methods

4.1. Hysteresis properties

In this study, the hysteresis properties were measured by the MicroMag™ Model 2900 Alternating Gradient Magnetometer (AGM) housed in Michigan Tech's Earth Magnetism Laboratory (EML) (Figure 4.1). The AGM determines the magnetic properties through combined use of alternating and direct fields. Two gradient field coils create a magnetic field in the measurement area where the sample is placed. The horizontal motion of the sample is detected by a symmetrical piezoelectric bimorph (Graham 2000). The AGM measures the hysteresis properties with an extremely high sensitivity (10 nanoemu standard deviation with a speed at 1 second per point). A parallel silica fine probe is used as a support for samples.

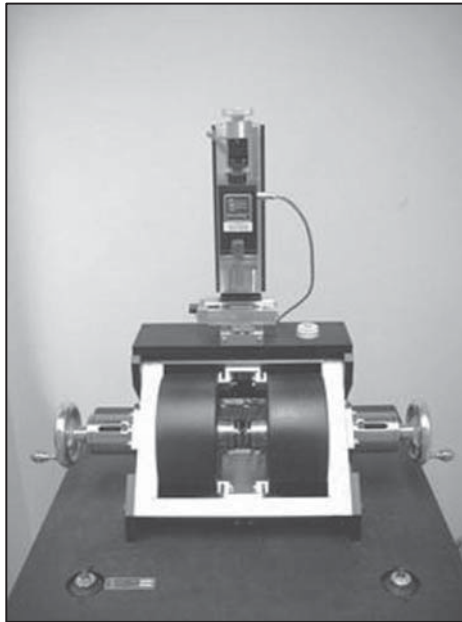


Figure 4.1: Photo of the Alternating Gradient Magnetometer at Michigan Tech.

Before each measurement, the probe was cleaned with alcohol. To calibrate the instrument, an yttrium iron garnet sphere standard, with a known magnetic moment (77.64 memu) was measured. The empty holder was also measured in order to later subtract the effect of the empty holder.

For each sample, the same procedure was followed. A small part of sample was crushed in order to obtain a small chip with approximate size of 1mm x 1mm x 1mm. To prevent the magnetization effects due to shape, the best sample for this measurement is ideally a sphere. Therefore, we selected samples that were as close to a sphere as possible.

The AGM provides information regarding the magnetic moment M (in emu) versus the applied magnetic field (in mT). Two corrections to raw data are done. The first is to subtract the previously measured empty holder. The second correction adjusts the slope of the hysteresis loop, so that the dia- and paramagnetic contributions are minimized (Figure 4.2). After the corrections, data were imported into Microsoft Excel for plotting purposes.

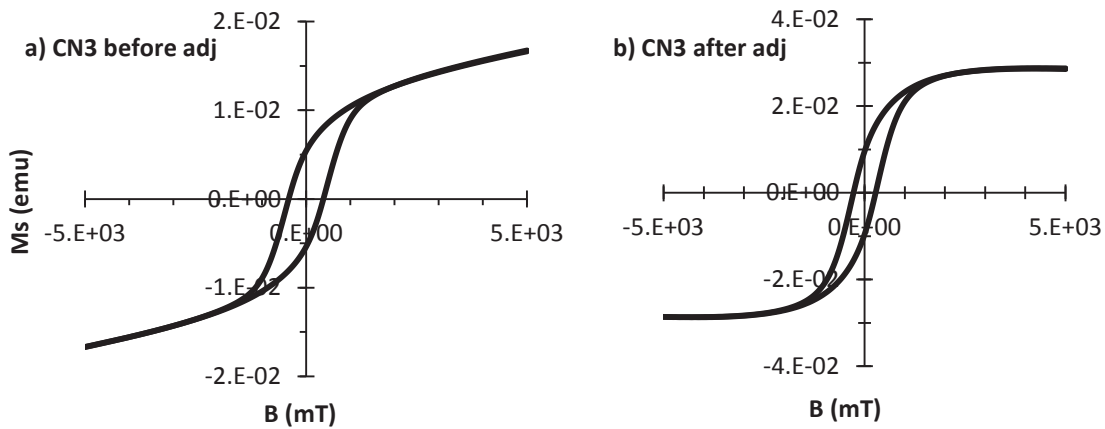


Figure 4.2: Typical hysteresis loop a) before and b) after paramagnetic slope correction.

4.2. Thermomagnetic curves

In this study, an AGICO (Advanced Geosciences Instruments Company) MFK1-FA Kappabridge equipped with a CS-3 Furnace Apparatus and a CS-L Cryostat was used to measure the temperature dependence of low-field magnetic susceptibility (thermomagnetic curves) (Figure 4.3).

Each sample was prepared by crushing with an iron mortar and pestle to a very fine powder. All samples were weighted by a balance with precision of $\pm 0.001\text{g}$ (Table 4.1).



Figure 4.3: Photo of the Kappabridge instrument used during this study.

Table 4.1:
Sample weights for the thermomagnetic analysis

Sample	Location	Weight (g)
<i>Canada</i>		
TB-CN3	dyke	0.479
TB-CN4	dyke	0.406
TB-CM1	lava flow	0.464
TB-CM2	lava flow	0.654
<i>New Mexico</i>		
NM-CM-3A	dyke	0.511
NM-CMvS	vent	0.540
NM-CMB-1	lava flow	0.566
NM-CMB-2	lava flow	0.451
NM-CMB-3	lava flow	0.253

The same analysis for each sample is completed, divided into three parts. Thermomagnetic analyses begin and end by a heating at low temperature from -192°C to 5°C. Between the two low temperature runs, the susceptibility is measured during heating and cooling at high temperatures from room temperature to 700°C. The atmosphere during these high temperature analyses were generally controlled by utilizing Argon gas (exceptions are noted in the study). For all measurements the effect of the holder is subtracted from the results.

4.3. Optical microscope

Before petrographic analysis, a small sample (less than 2.5 cm in diameter) is prepared by slicing samples with a diamond saw. Some of the samples were attached into epoxy in order to have the standard size for the SEM. The epoxy should dry for at least 24 hours. For this study, samples were dried for more than two full days. Unfortunately, for the first run, the epoxy was too soft, resulting in poor quality SEM images. A second

set of samples was prepared and analyzed without epoxy. Avoiding the epoxy permits the heating of the sample between successive analyses. All samples are polished in successive steps of decreasing size of diamond composite grains to increase the quality of the polish (120 μm , 60 μm , 35 μm , 15 μm , 6 μm , and 1 μm).

Observation of samples by reflected light was done with an optical microscope Olympus PMG3 Metallograph equipped with a Leica EC3 digital camera. Leica Application Suite EZ image capture software was used to save and treat images.

4.4. Scanning Electron Microscope

The magnetic mineralogy of samples was studied using a Scanning Electron Microscope (SEM) JEOL 6400 equipped with a tungsten filament (Figure 4.4). The SEM magnification range is between 10x to 300,000x and the accelerating beam voltage is between 0.2 kV and 40 kV. All samples were coated with carbon.

For these analyses the working distance was set to 15 mm and an accelerating voltage of 20 kV was used. Only light colored minerals were described during these analyses, corresponding to titanomagnetites within the rock.

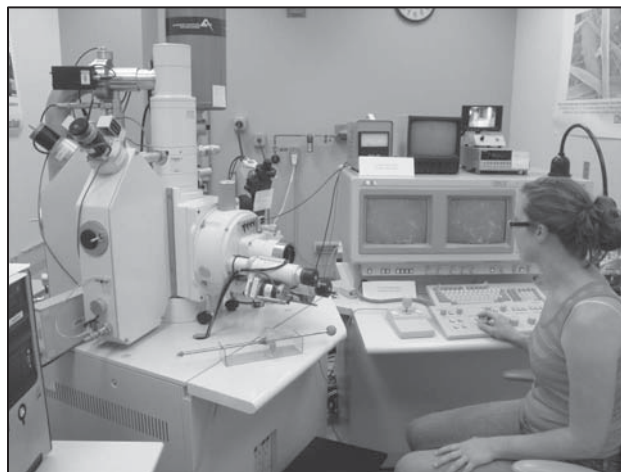


Figure 4.4: SEM JEOL 6400 at Michigan Technological University.

5. Results / Discussion

5.1. Hysteresis properties

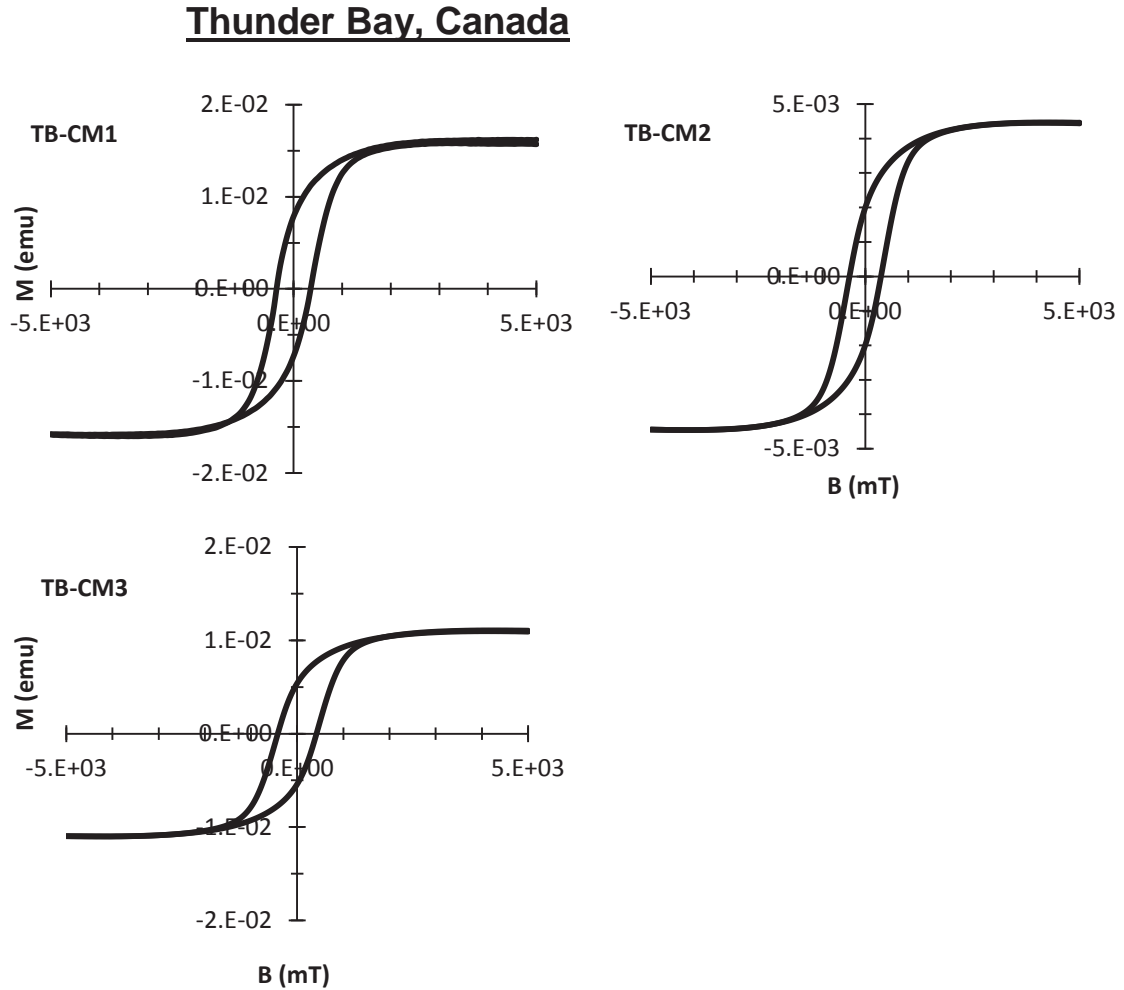


Figure 5.1: Hysteresis loops measured from the lava flow samples TB-CM1, TB-CM2, and TB-CM3 from Thunder Bay (Canada).

Hysteresis loops of the Thunder Bay lava flow (Figure 5.1) are generally wider than the loops measured from the dyke (Figure 5.2) suggesting a larger amount of multi-domains components in the lava flow samples.

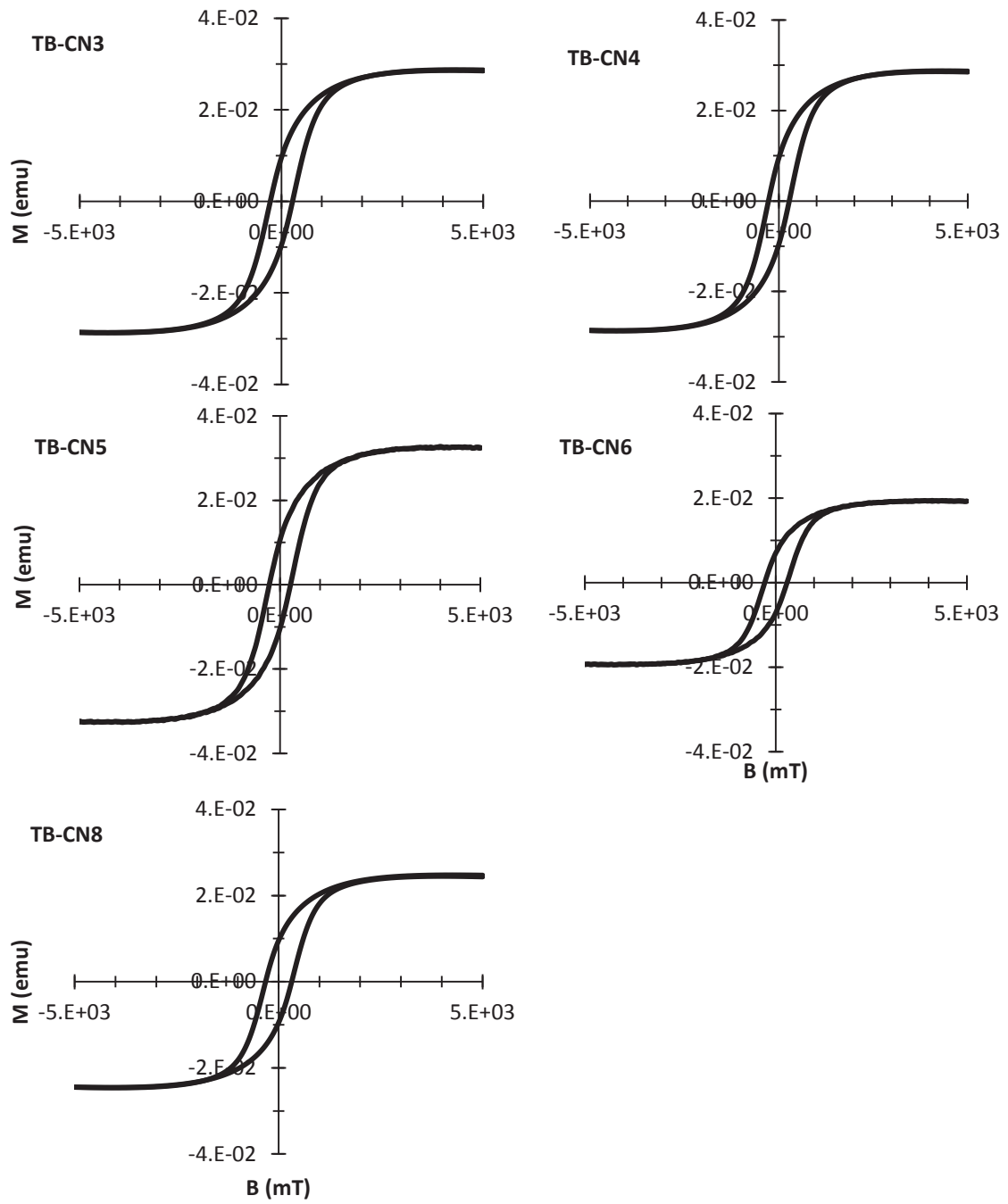


Figure 5.2: Hysteresis loops measured from the dyke samples TB-CN3, TB-CN4, TB-CN5, TB-CN6 and TB-CN8 from Thunder Bay (Canada).

La Cienega, New-Mexico

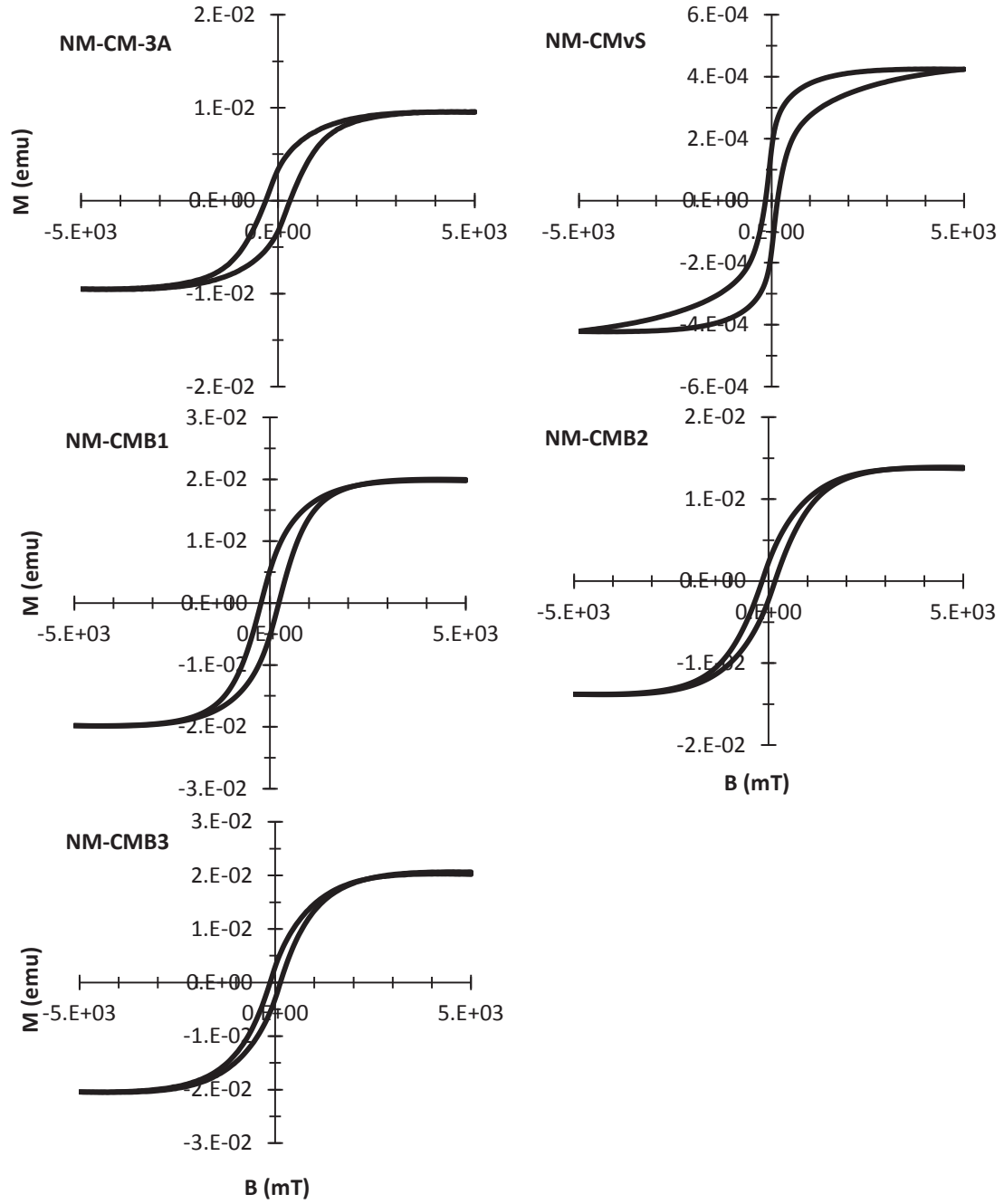


Figure 5.3: Hysteresis loops measured from the samples NM-CM-3A, NM-CMvS, NM-CMB1, NM-CMB2, and NM-CMB3 from La Cienega (New Mexico).

For the New Mexico samples, the hysteresis loops become less wide with the distance from the dyke. In this set of samples, there is a gradual decrease in MD

components with respect to the distance from the dyke. The hysteresis loop from the vent sample has a “wasp-waisted” shape suggesting a mix between single domain and superparamagnetic domain magnetic carriers (Figure 5.3).

Day-plot

Some results from the Thunder Bay samples were provided by Elisa Piispa (Michigan Technological University) in 2011 and are integrated to this study (Table 5.1).

Table 5.1:
Magnetic properties^a of rock samples

Site	Bc (Oe)	Mr (memu)	Ms (memu)	Bcr (Oe)	Bcr/Bc	Mr/Ms
<i>Canada</i>						
<i>Dyke</i>						
TB-CN2	377.9	1.465	3.523	568.6	1.50	0.416
TB-CN3	275.3	9.558	28.580	419.4	1.52	0.334
TB-CN4	266.1	8.906	27.940	421.0	1.58	0.318
TB-CN5	264.8	10.470	32.460	407.4	1.54	0.322
TB-CN6	292.1	7.079	19.290	439.7	1.51	0.366
TB-CN7	298.2	13.270	38.360	442.5	1.48	0.346
TB-CN8	320.3	9.533	24.590	465.5	1.45	0.387
<i>Lava</i>						
TB-CM1	502.3	5.597	10.740	688.0	1.37	0.521
TB-CM1c	351.2	7.588	15.980	498.9	1.42	0.475
TB-CM2	322.3	0.106	0.314	575.7	1.79	0.339
TB-CM2b	367.3	1.994	4.453	555.7	1.51	0.447
TB-CM3e	419.1	5.399	10.950	594.5	1.42	0.492
<i>New Mexico</i>						
<i>Dyke</i>						
NM-CM3A	307.2	3.329	9.510	650.7	2.12	0.350
<i>Vent</i>						
NM-CMvS	156.2	0.165	0.423	753.2	4.82	0.389
<i>Lava</i>						
NM-CMB1	226.9	5.244	19.790	434.3	1.91	0.265
NM-CMB2	165.8	2.288	13.770	599.5	3.62	0.166
NM-CMB3	131.0	2.981	20.330	413.2	3.15	0.146

^aColumn heading indicate: Bc = the coercive force, Mr = the saturation remanent magnetization, Ms = the saturation magnetization, and Bcr = coercivity of remanance.

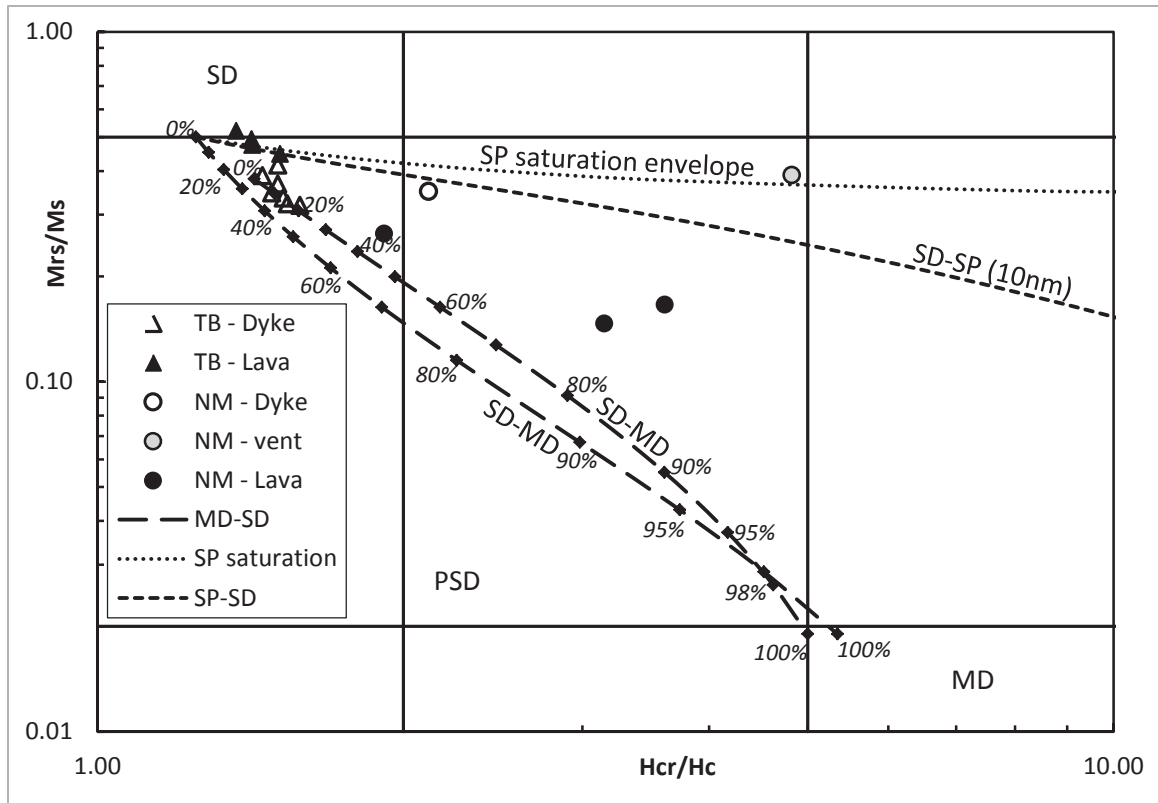


Figure 5.4: Day-plot (Day et al. 1977) for Thunder Bay (triangle) and La Cienega (circle). In solid forms are dyke samples, in open forms lava samples, and in striped form the vent sample. Graph shows the ratio of M_{rs}/M_s (M_{rs} = the saturation remanent magnetization and M_s the saturation magnetization) as a function of the ratio B_{cr}/B_c (B_{cr} = the coercivity of remanence and B_c the coercive force). Three main domain states are characterized: the single domain SD, the pseudo-single domain PSD, and the multi domain MD. The superparamagnetic SP saturation envelope and the mixture models (SD-SP and SD-MD) are also plotted (Dunlop 2002).

The Day-plot in Figure 5.4 shows the relation of the ratio of saturation remanent magnetization to the saturation magnetization (M_{rs}/M_s) and the ratio of the coercive remanence to the coercive force (B_{cr}/B_c) (Figure 5.4) (Day et al. 1977). The mixture models (Dunlop 2002) for a SD and MD grain sizes are added to this graph. The results of Thunder Bay samples plot close to this SD-MD mixture curve. The Thunder Bay samples show values less than 2 for the ratio B_{cr}/B_c . This is described in Dunlop's study

(2002) as a mix between SD and MD with less than 50% of MD. Samples from La Cienega in New Mexico plot further from the SD-MD mixture curves. If results from these samples are compared to the theoretical model, the fraction of MD is greater than SD remanance carriers. The samples from the dyke and the vent of La Cienega do not fit on to this mixture curve. According to Dunlop (2002), the composition of these samples would correspond to a SD-SP mixture with a larger amount of SD component and a sample with saturation in SP grains.

Although the values for Thunder Bay samples are very well grouped on the graph and mainly composed of SD grains, the dyke has slightly more MD particles. The values on the graph do not show any correlation with the location of samples within the dyke or lava flow. The same observation can be made for samples for La Cienega. Values on the diagram are closer to the dyke for sample NM-CMB1, then sample NM-CMB3, and the furthest sample NM-CMB2. That does not correspond to the relative location in the dyke. Also, samples NM-CMB2 and NM-CMB3 show similar values.

5.2. Thermomagnetic curves

The temperature dependence of the susceptibility for Thunder Bay and La Cienega samples is measured in a weak magnetic field (200 A/m).

Thunder Bay, Canada

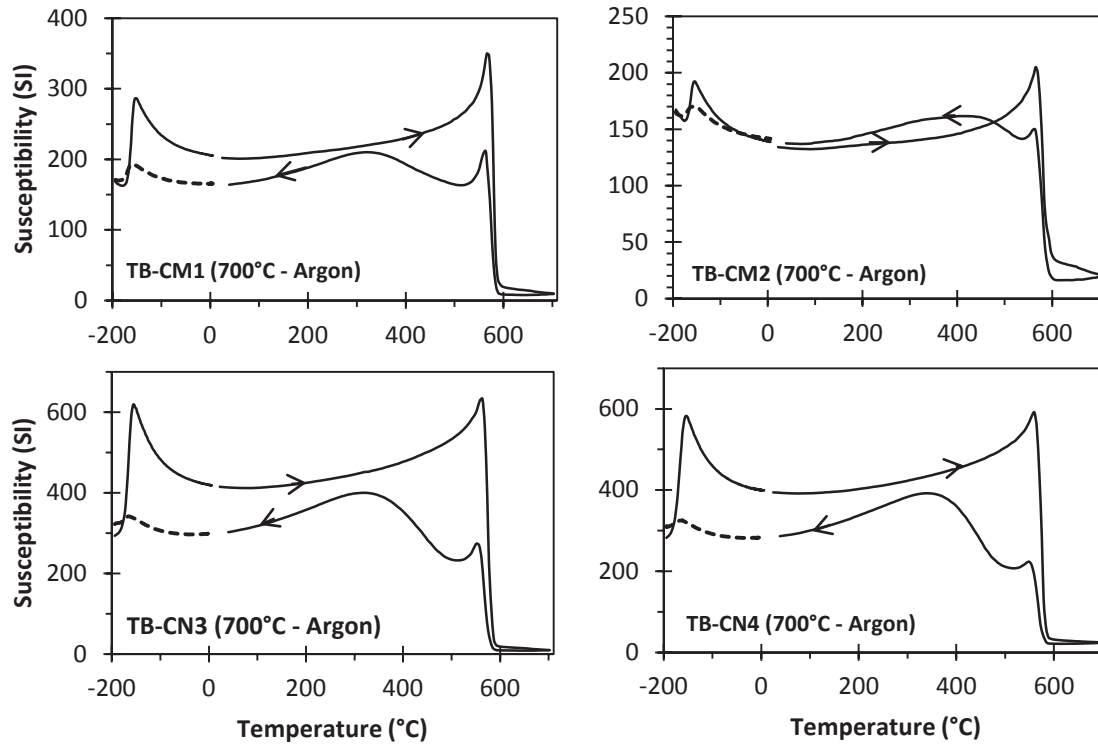


Figure 5.5: Representative thermomagnetic curves for samples from Thunder Bay, Canada in low and high temperature. The magnetic susceptibility analysis started and ended by heating in low temperature. The solid line is the first heating and the dotted line is the second heating. TB-CM1 and TB-CM2 are the lava flow samples and TB-CN3 and TB-CN4 are the dyke samples.

During high temperature thermomagnetic analysis, there is a high peak before 600°C (Figure 5.5). The susceptibility drops off rapidly after the peak for all the samples. This corresponds to the Curie temperature of magnetite at around 580°C (Hrouda et al. 1997). This confirms that a significant contribution of the titanomagnetite is almost pure

magnetite. Also, at low temperatures, curves show a peak at $\sim 150^{\circ}\text{C}$ corresponding to the Verwey transition of the magnetite. At this temperature, the magnetite passes from monoclinic to cubic structure (Verwey 1939).

The high temperature curves are not reversible. There is a difference in the magnetic susceptibility between heating and cooling of the sample. This irreversibility corresponds to a change of the magnetic mineral's composition at high temperatures. The peak corresponding to magnetite becomes smaller after heating, indicating a decrease of the amount of magnetite in the rock. Moreover, there is a new peak during the cooling at around 300°C . The peak is broad and makes difficult the estimation of the exact Curie temperature. The Curie temperature of the titanomagnetite series is large from $\sim 152^{\circ}\text{C}$ for ulvospinel to 577°C for magnetite, depending of the composition (Haggerty 1978; Lattard et al. 2006)). A peak at 300°C as seen on the Figure 5.5 could correspond to an amount of around 40% of ulvospinel.

On one hand, there is a decrease of the amount of magnetite in the rock; on the other hand there is a creation of TM40 after heating. Because the heating is done in argon atmosphere, an oxidation of the rock is impossible. Also there is a supposed amount of Ti-rich oxides such as ilmenite or ulvospinel intergrowth with magnetite. This creation of titanomagnetite 40 results to a mixing of composition between a phase titanium-rich (ulvospinel or ilmenite) and magnetites present within the rock. In order to have a better idea, a petrographic analysis is needed and would permit the composition and organization identification of each phase.

According to results found by E. Piispa in 2011, the temperature dependence of the susceptibility of these samples does not show any composition changes when heating to 600°C (Figure 5.6).

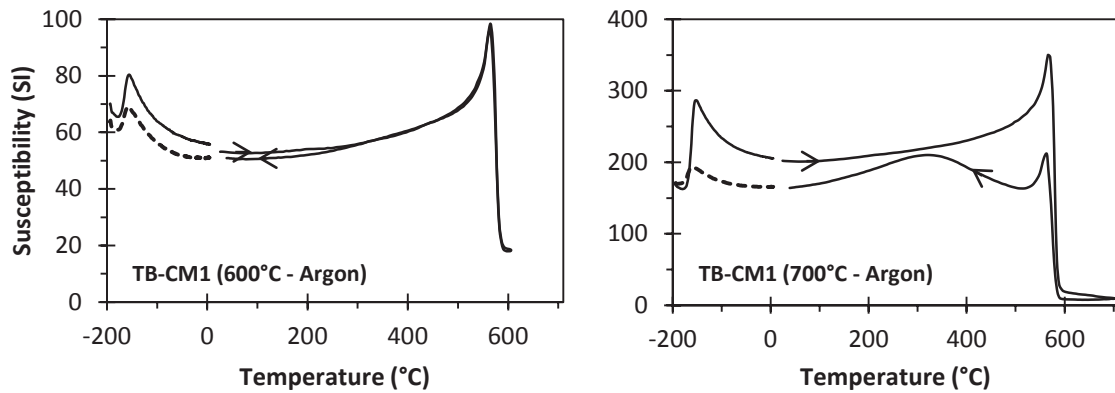


Figure 5.6: Representative thermomagnetic curves for samples from Thunder Bay, Canada in low and high temperature to 600°C and 700°C. The magnetic susceptibility analysis started and ended by heating in low temperature. The solid line is the first heating and the dotted line is the second heating.

Figure 5.6 shows the same result for samples heated to 600°C and 700°C. Unlike the sample heated to 700°C, the sample heated to only 600°C shows a reversible high temperature thermomagnetic curve. This result suggests that the modification within the rock occurs between 600°C and 700°C, probably related to the creation of titanomagnetite by homogenization or mixing of composition.

The thermomagnetic curves suggest the sample is mostly composed of titanium-poor titanomagnetite or magnetite. At high temperatures, between 600°C and 700°C, the magnetic carrier undergoes changes. Analysis shows a reorganization of elements from magnetite and ilmenite to a TM phase. This separation creates two phases, one containing more ilmenite and another phase more magnetite. The Curie temperature of 300°C corresponds to a composition of TM40 (titanomagnetite with 40% of titanium) (Lattard 2006) or to a composition of titanohematite also with 40% of titanium (Ishikawa and Akimoto 1957).

La Cienega, New-Mexico

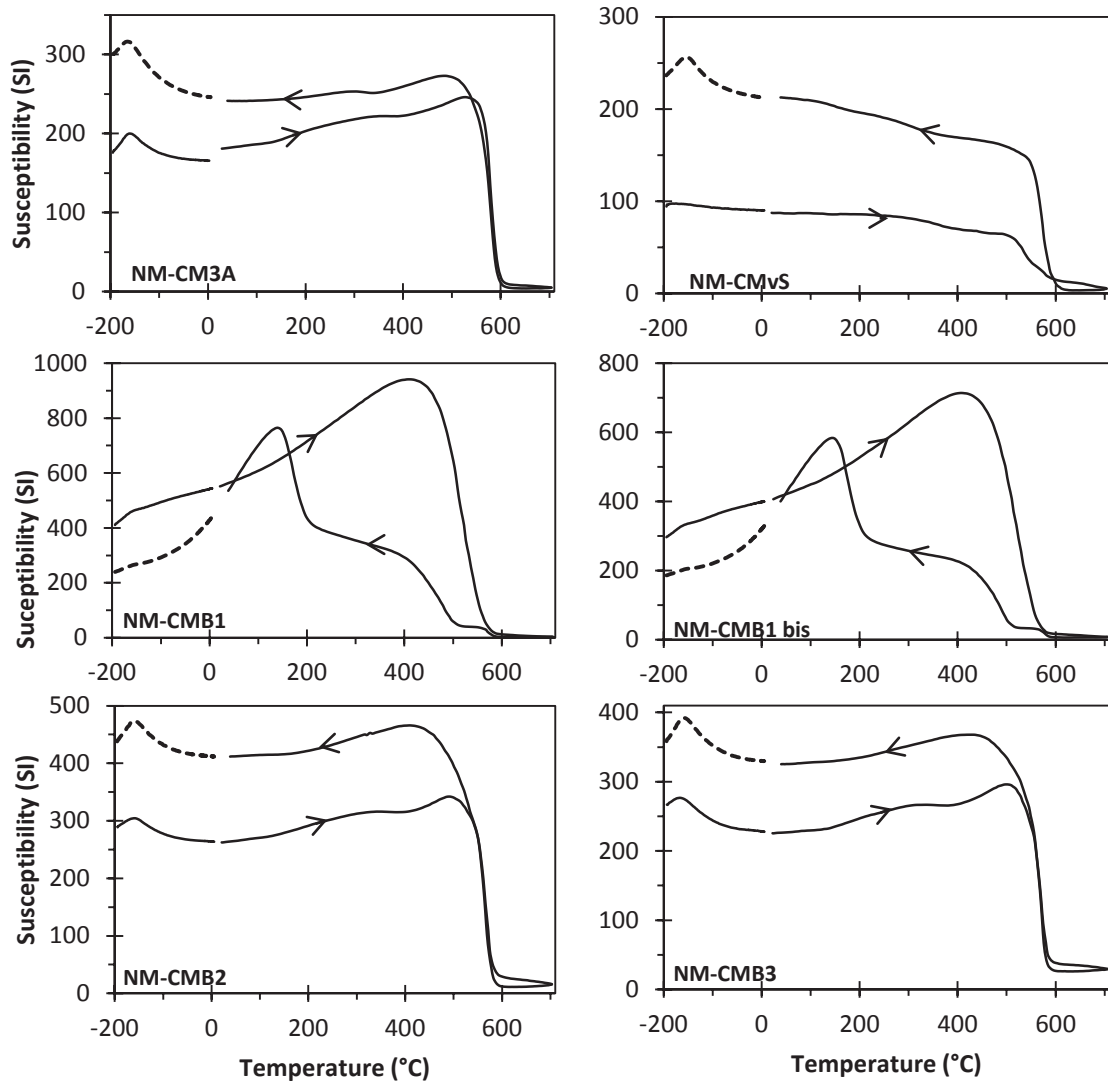


Figure 5.7: Representative thermomagnetic curves for samples from La Cienega, New Mexico in low and high temperature. The magnetic susceptibility analysis started and ended by heating in low temperature. The solid line is the first heating and the dotted line is the second heating. NM-CM3A is the dyke sample, NM-CMvS is the vent sample and NM-CMB1, NM-CMB2, and NM-CMB3 are the lava samples.

The sample NM-CMB1 shows very different behavior from other La Cienega rocks. To be sure of the reliability of the analysis and to exclude any problems with the argon gas or other factors, the measurement was repeated twice with the same result (Figure 5.8). This sample reacted to the treatment differently than NM-CMB2 and NM-CMB3, although it is from the same lava flow. This case is discussed later.

The thermomagnetic curves of New Mexico samples (Figure 5.7) show small peaks during the first and second low temperature analyses corresponding to the Verwey transition (Verwey 1939). This indicates the presence of almost pure magnetite on the rock.

Unlike the Canadian samples, for New-Mexico samples the temperature of the peak is less than the Curie temperature of the magnetite estimated to $\sim 580^{\circ}\text{C}$. The peak begins before 500°C and the drop off after the peak continues until 580°C . It is noted that the Curie temperature of the titanomagnetite decreases with increasing amounts of titanium (Readman and O'Reilly 1971; Stacey and Banerjee 1974). This suggests the presence of titanomagnetite with a small amount of titanium (Ishikawa and Akimoto 1957).

After a high temperature analysis, samples show a higher susceptibility and a larger amount of magnetite within the rock. Also, there is the small bump at around 300°C present during heating that is not observable during cooling. This temperature corresponds to a TM40. Different quantities of magnetites and the disappearance of TM40 are interpreted as a result of an unmixing of composition. The initial TM40 undergoes a second deuteritic oxidation resulting into a phase more magnetite and a phase closer to ilmenite or ulvospinel. These samples react in an opposite manner than Thunder Bay samples.

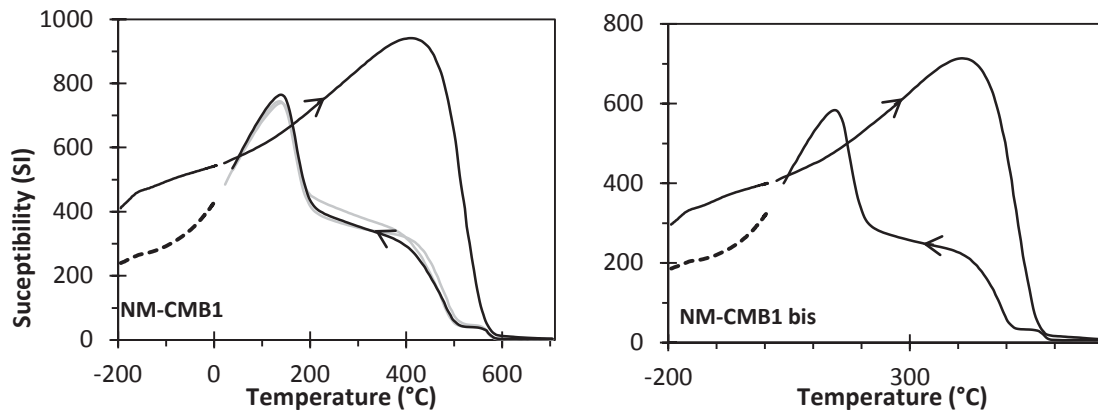


Figure 5.8: Representative thermomagnetic curves for the sample NM-CMB1 from La Cienega, New Mexico at low and high temperature. The magnetic susceptibility analysis started and ended by heating in low temperature. The full line is the first heating and the dotted line is the second heating. Gray lines are a second high temperature analysis.

For NM-CMB1 sample, the thermomagnetic curves for the two low temperature analysis show very small amount magnetite in the rock by the absence of a Verwey peak (Verwey 1939). The peak during the high temperature run is similar to the peak previously seen just before 600°C in other samples. This corresponds to a creation of titanomagnetites close to pure magnetite. The extension of the peak shows that the titanomagnetite is more Ti-rich than in Thunder Bay samples.

On the cooling leg, three different peaks are observed. The first peak occurs at around 580°C. This peak corresponds to almost pure magnetite. The second peak appears at the same temperature as during heating. This lower Curie temperature corresponds to the presence of more Ti-rich titanomagnetites with more titanium (Readman and O'Reilly 1971). During heating, these titanomagnetites unmix in two compositions: a small amount of Ti-poor and a large amount of Ti-rich. The third peak corresponds to a Curie temperature close to 100°C. The magnetite-ulvospinel series presents Curie temperatures between ~-153°C and ~577°C. There is a linear relation between the composition and the Curie temperature, low for ulvospinel and high for magnetite. The peak found at 100°C corresponds to a large amount of titanomagnetite around TM70 created during the heating to 700°C (Lattard 2006).

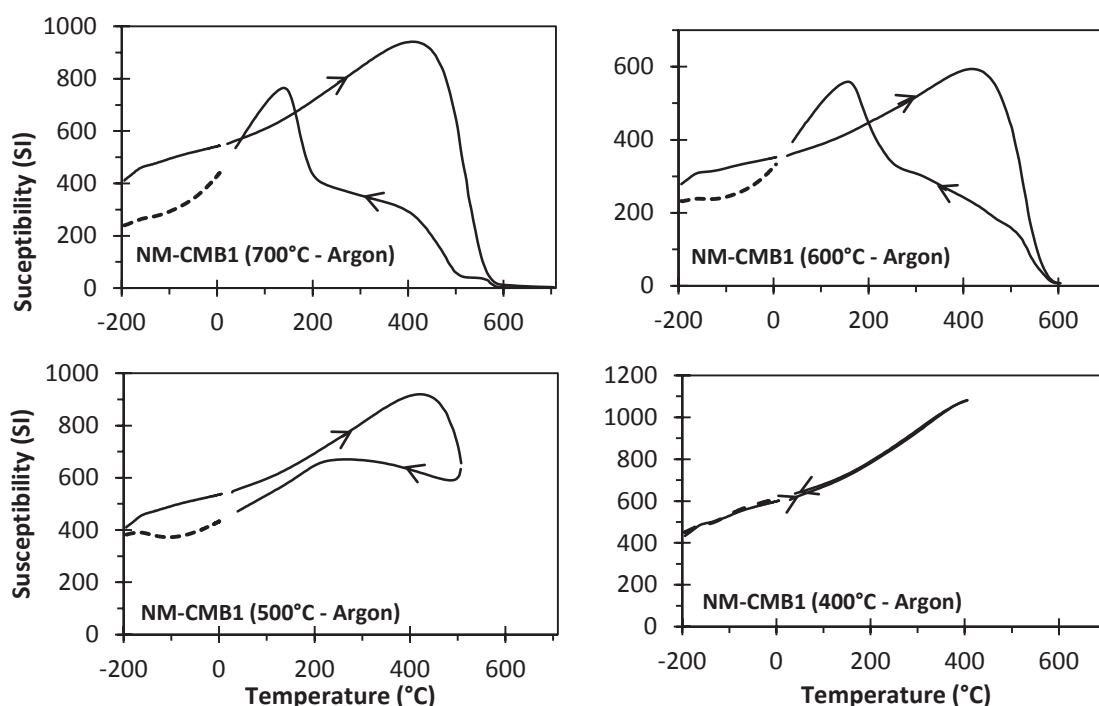


Figure 5.9: Representative thermomagnetic curves for the sample NM-CMB1 from La Cienega, New Mexico at low and high temperatures. The magnetic susceptibility analysis started and ended by heating in low temperature. The peak temperature varies from 700°C to 400°. The solid line is the first heating and the dotted line is the second heating.

As seen previously, after heating to 700°C, sample NM-CMB1 forms different phases not present before. The same analysis to 600°C shows a similar type of transformation, but with only two distinguishable peaks (Figure 5.9). Almost pure magnetite with a Curie temperature at 580°C is created when heating to 700°C. The increase in susceptibility at around 150°C is comparable to heating results, but at 600°C the slope of the peak is smaller. Moreover, at room temperature the susceptibility is around the same before and after the heating for both analyses. Additionally, after heating to 500°C the susceptibility of the rock at room temperature is lower. The peak shows a Curie temperature at around 200°C. The average composition of magnetic minerals is around 50% ilmenite (Ishikawa and Akimoto 1957). During heating, there is a change of

the composition from titanomagnetite a “closer-to-magnetite” with around 15% of titanium to a phase richer in titanium with the composition TM60. This confirms the idea of the homogenization of composition to a TM60 more stable and common.

The thermomagnetic analyses show a high concentration of titanomagnetite in the rock with a small amount of titanium before heating to 700°C. After heating, the quantity of Ti-poor magnetite increased. Only in the dyke sample contains titanohematite after the heating. For lava samples the titanomagnetite TM40 disappear during cooling. The exception is NM-CMB1, the sample closest to the dyke showing very different results. The composition of minerals on this rock goes from a uni-modal phase of titanomagnetites to a bi-modal phase. The titanomagnetite undergoes a separation of the composition between a phase closer to magnetite and a phase closer to TM60.

5.3. Optical microscope

Thunder Bay, Canada

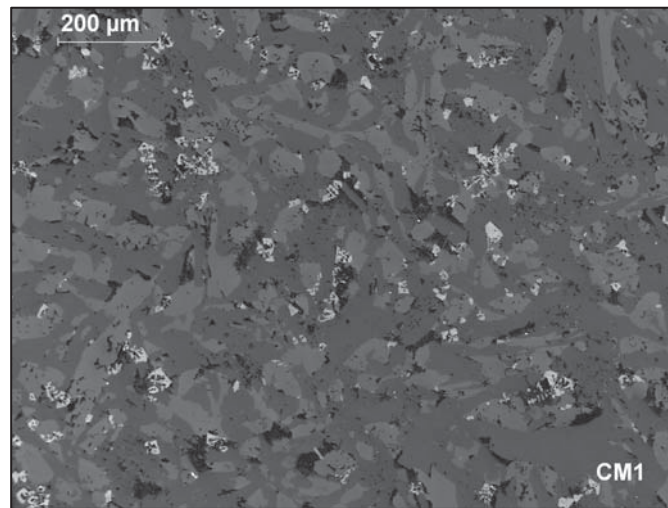


Figure 5.10: Sample TB-CM1 observed with an optical microscope in reflected light, objective x10. Scale bar is 200 μm.

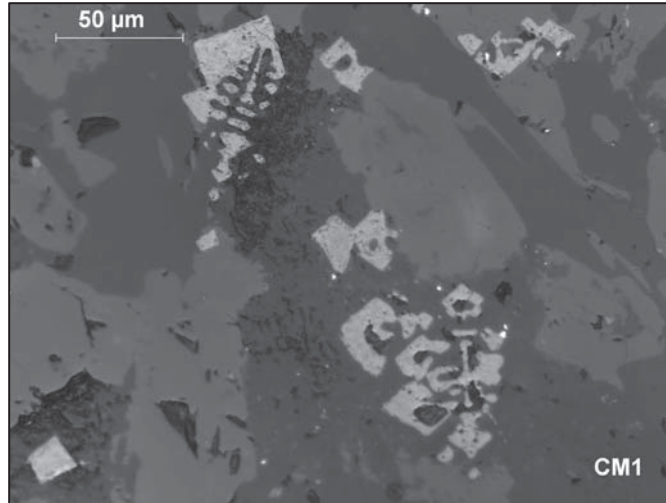


Figure 5.11: Sample TB-CM1 observed with an optical microscope in reflected light, objective x50. Scale bar is 50 μm .

Figure 5.10 is a photo of the sample TB-CM1 in reflected-light with an optical microscope. Titanomagnetites can be observed in lighter colors. Their sizes are fairly small ($\sim 50\mu\text{m}$). They are present everywhere in the rock with the same quantity and the same size. The black zones in pictures are cavities and can be disregarded. In Figure 5.11, the typical titanomagnetite minerals can be seen in finer detail. All these minerals present a dendritic form typical of a fast solidification. The sizes of the dendrites are about 50 μm (Figure 5.11). The composition of titanomagnetites seems homogeneous in this rock.

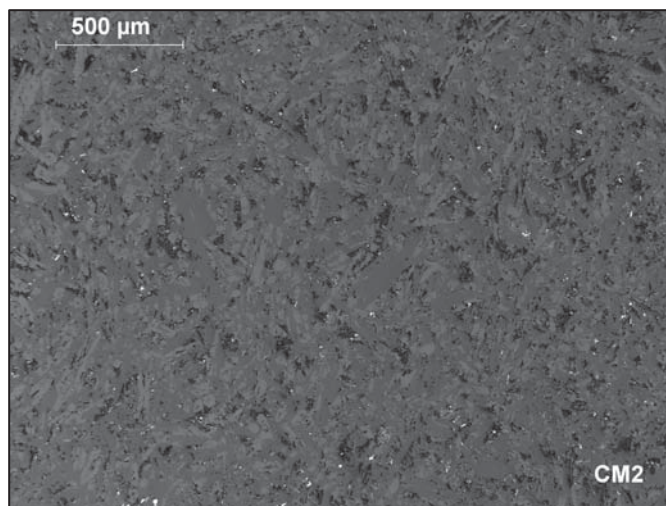


Figure 5.12: Sample TB-CM2 observed with an optical microscope in reflected light, objective x5. Scale bar is 500 μm .

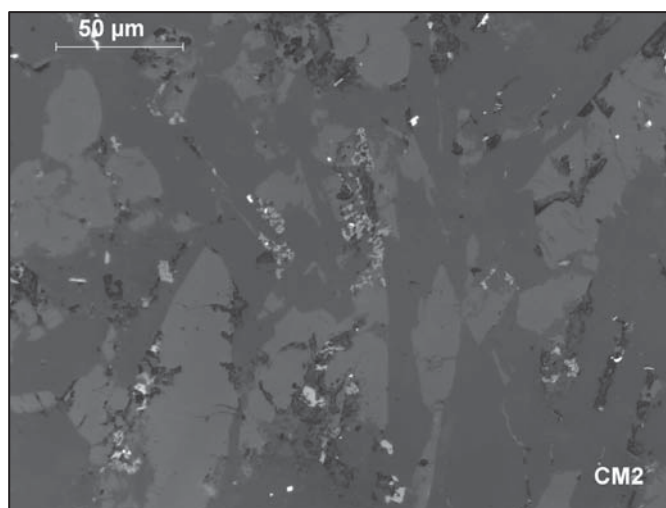


Figure 5.13: Sample TB-CM2 observed with an optical microscope in reflected light, objective x50. Scale bar is 50 μm .

In sample TB-CM2 (Figure 5.12), titanomagnetites are smaller and fewer than in sample TB-CM1 (Figure 5.10). In Figure 5.13, the size of the larger titanomagnetite can be approximated at 10 μm . Magnetic minerals seem to be of single and homogeneous composition. The two different shades of gray in photos can be explained by the leftover of polish particles.

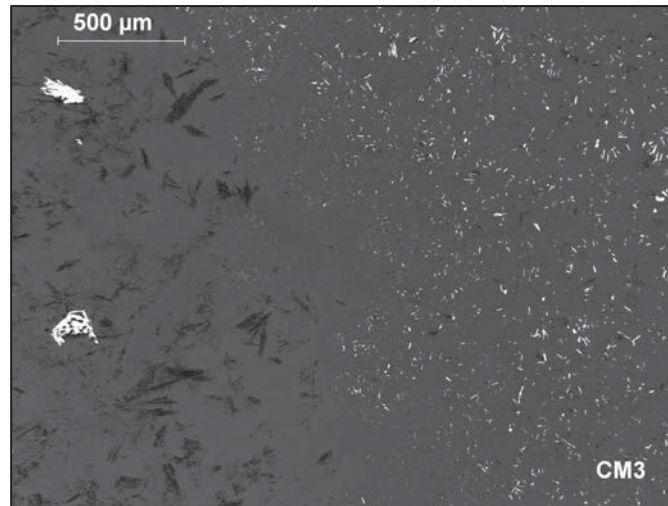


Figure 5.14: Sample TB-CM3 observed with an optical microscope in reflected light, objective x5. Scale bar is 500 μm.

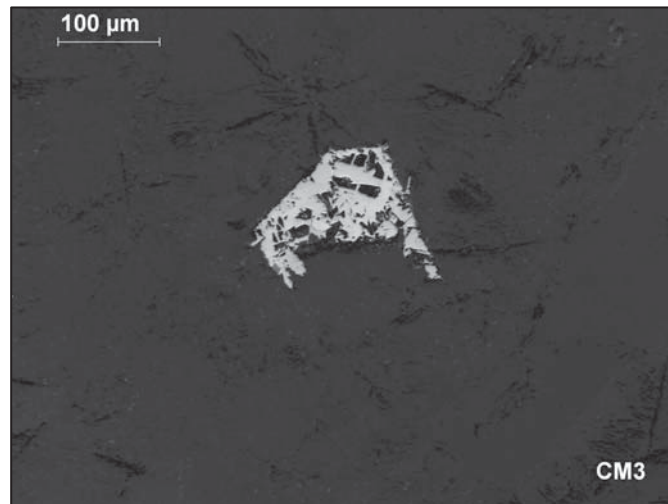


Figure 5.15: Sample TB-CM3 observed with an optical microscope in reflected light at high contrast, objective x20. Scale bar is 100 μm.

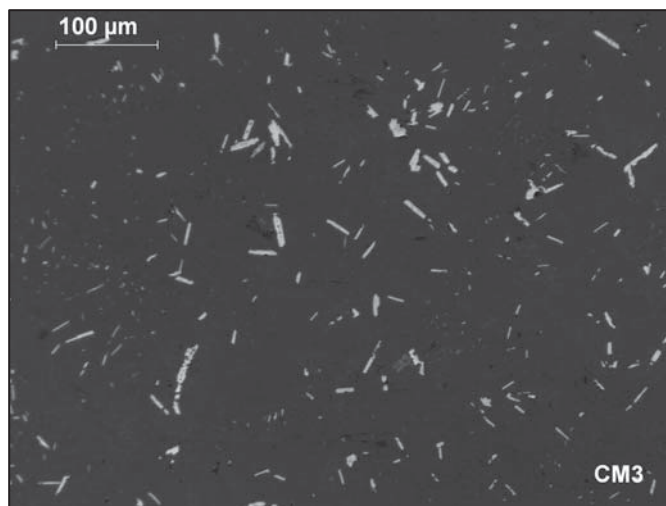


Figure 5.16: Sample TB-CM3 observed with an optical microscope in reflected light at high contrast, objective x20. Scale bar is 100 μm .

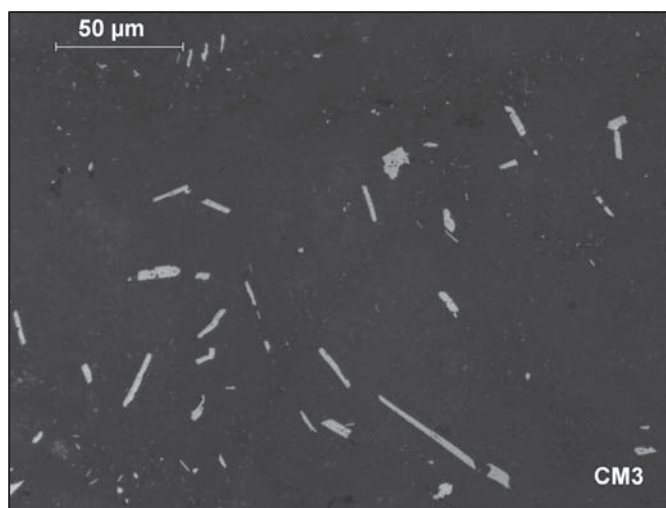


Figure 5.17: Sample TB-CM3 observed with an optical microscope in reflected light at high contrast, objective x50. Scale bar is 50 μm .

Sample TB-CM3 shows different shape of titanomagnetites than previous samples from the same lava flow. In Figure 5.14, there are two different zones. On the left there are very few but large titanomagnetite grains. The size of the crystal is $\sim 120\ \mu\text{m}$ and has a dendritic form (Figure 5.15). The mineral seems to be homogeneous. On the right part of Figure 5.14, the titanomagnetites are smaller and greater in quantity. This part of the

rock is closer to the organization and composition of samples NM-CM1 and NM-CM2. Figure 5.16 and Figure 5.17 display estimated sizes of approximated 30 μm to 50 μm for the largest minerals. The form is very thin and long, lath-like in shape with homogeneous composition.

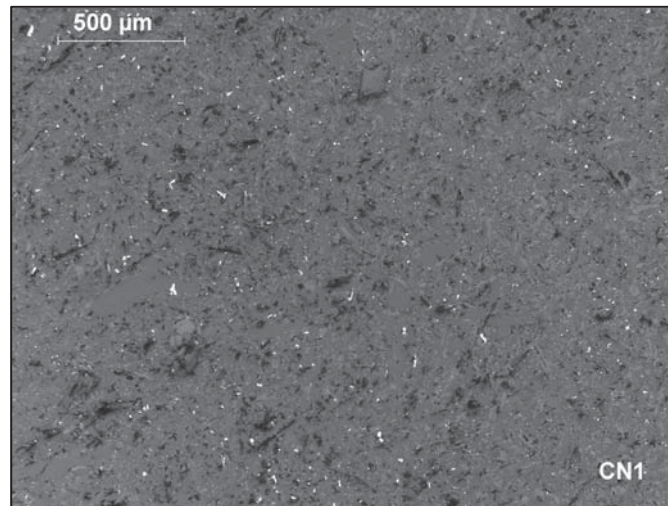


Figure 5.18: Sample TB-CN1 observed with an optical microscope in reflected light, objective x5. Scale bar is 500 μm .

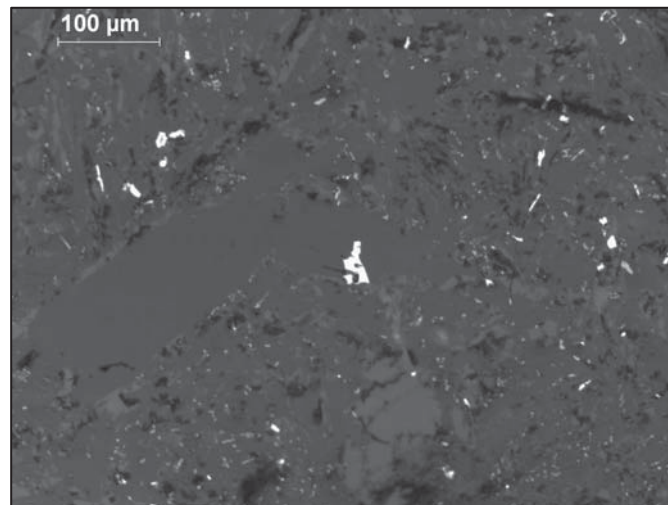


Figure 5.19: Sample TB-CN1 observed with an optical microscope in reflected light at high contrast, objective x20. Scale bar is 100 μm .

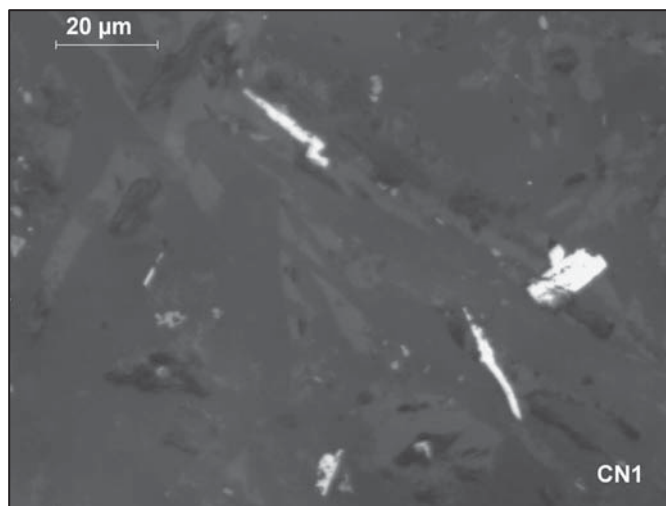


Figure 5.20: Sample TB-CN1 observed with an optical microscope in reflected light, objective x100. Scale bar is 20 μm .

TB-CN1 presents small titanomagnetite minerals (Figure 5.18). The quantity of this mineral is the same throughout the sample. In Figure 5.19, we can see different sizes for titanomagnetite, most with a lath form. The largest minerals are around 20 μm . Although the resolution of Figure 5.20 does not permit seeing any differences in composition or organization inside the mineral, it seems compositionally homogeneous.

Sample TB-CN3 does not have any photos as the polish did not permit any usable photos with the optical microscope. Observation showed minerals a bit larger than TB-CN1 ($\sim 25\mu\text{m}$) with a dendritic form and a homogeneous composition.

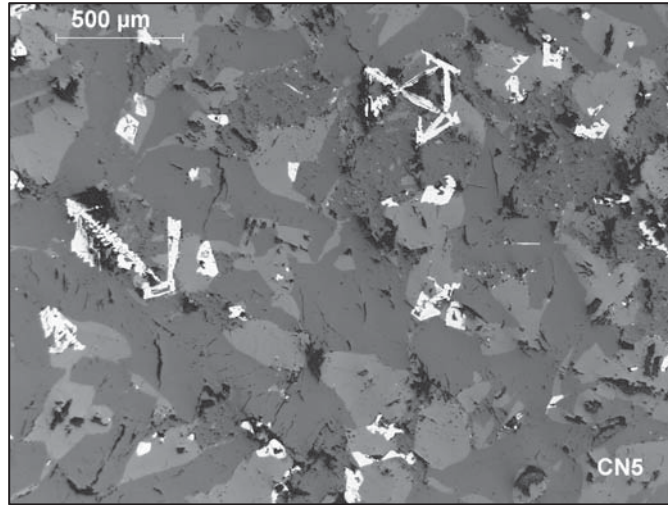


Figure 5.21: Sample TB-CN5 observed with an optical microscope in reflected light, objective x5. Scale bar is 500 μm.

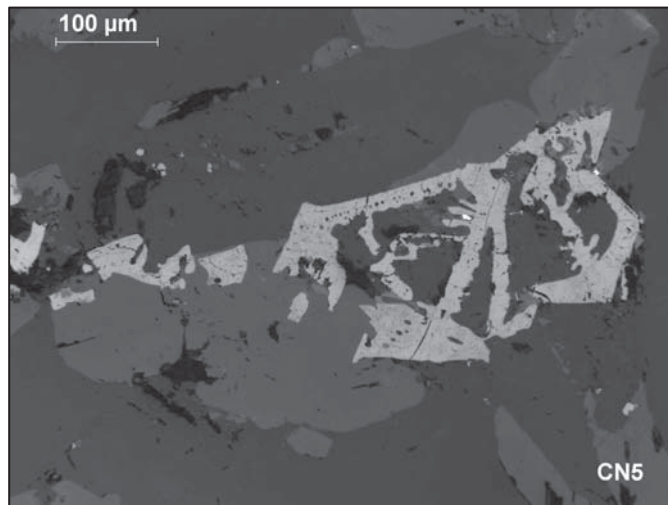


Figure 5.22: Sample TB-CN5 observed with an optical microscope in reflected light, objective x20. Scale bar is 100 μm.

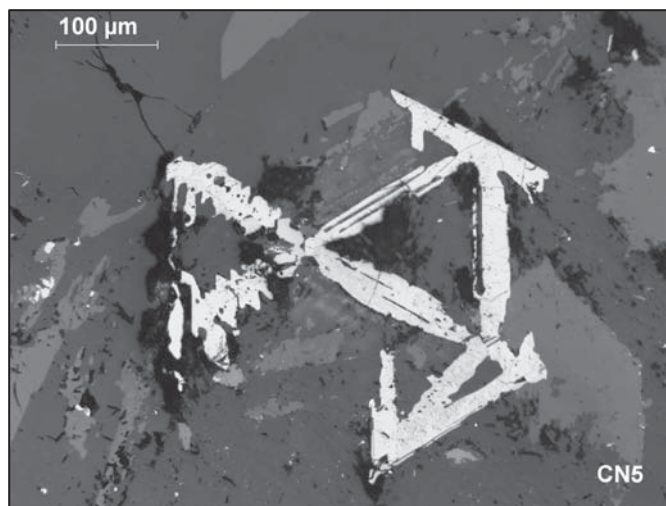


Figure 5.23: Sample TB-CN5 observed with an optical microscope in reflected light, objective x20. Scale bar is 100 μm.

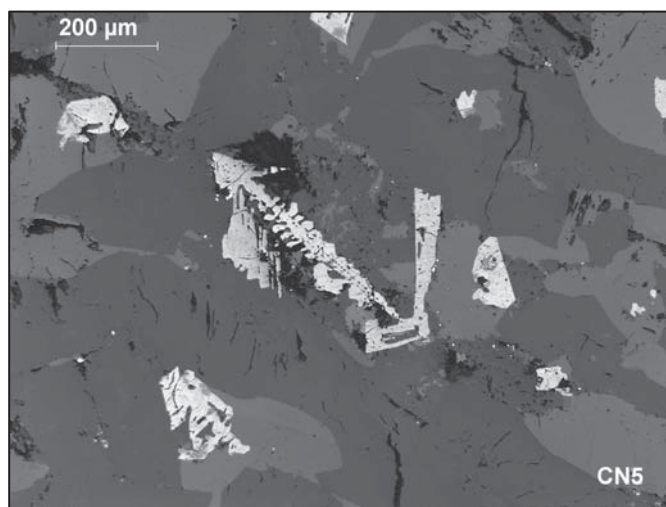


Figure 5.24: Sample TB-CN5 observed with an optical microscope in reflected light, objective x10. Scale bar is 200 μm.

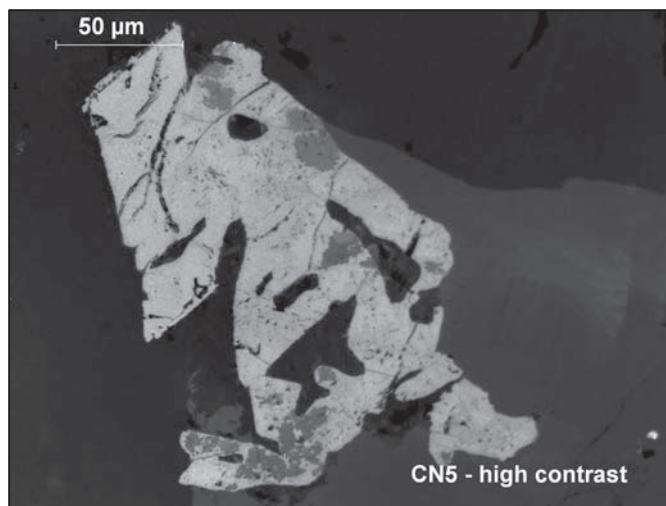


Figure 5.25: Sample TB-CN5 observed with an optical microscope in reflected light at high contrast, objective x50. Scale bar is 50 μm .

The titanomagnetite grains in this sample TB-CN5 are much larger than in other samples (Figure 5.21). These dendrites are well formed and very big. The largest grains are between 400 μm and 500 μm . In the Figure 5.22 and Figure 5.23, the dendrites look homogeneous. In the Figure 5.24, there are different shades of grays inside the titanomagnetite crystals which are more visible in Figure 5.25. Three different shades of gray can be distinguished, explained by three different compositions of the mineral. They are organized on the mineral by small zones and can be the result of alteration of the rock. If we observe the whole rock, titanomagnetites are mainly homogeneous. Only few grains contain different compositions.

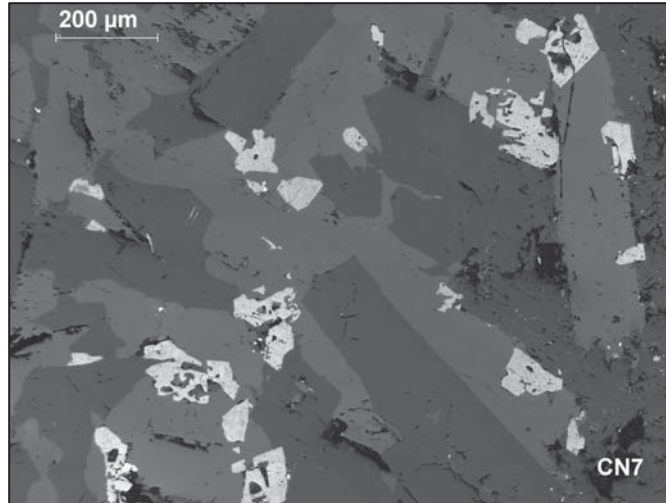


Figure 5.26: Sample TB-CN7 observed with an optical microscope in reflected light, objective x10. Scale bar is 200 μm .

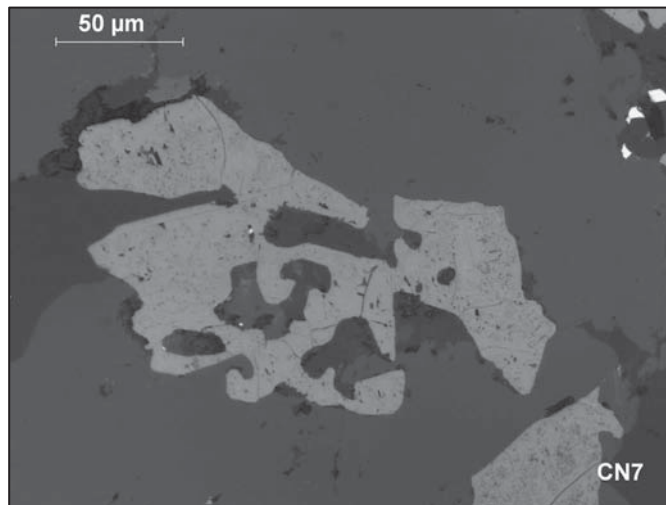


Figure 5.27: Sample TB-CN7 observed with an optical microscope in reflected light at high contrast, objective x50. Scale bar is 50 μm .

Minerals of titanomagnetite on sample TB-CN7 are smaller than TB-CN5 sample, but noticeably larger than in other Canadian samples (Figure 5.26). These dendritic forms are around 100 to 200 μm in size and the mineralogy appears to be homogeneous (Figure 5.27).

La Cienega, New-Mexico

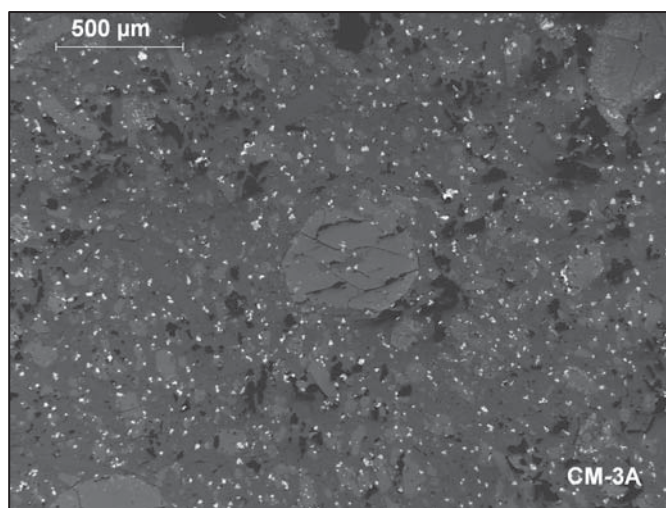


Figure 5.28: Sample NM-CM3A observed with an optical microscope in reflected light at high contrast, objective x5. Scale bar is 500 μm.

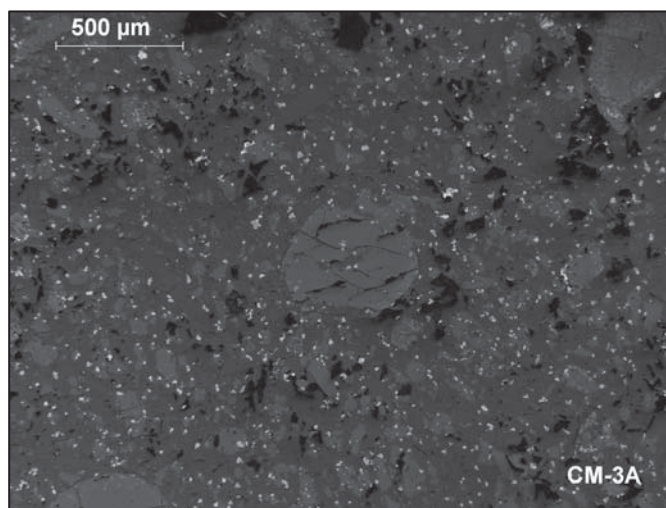


Figure 5.29: Sample NM-CM3A observed with an optical microscope in reflected light at high contrast, objective x10. Scale bar is 200 μm.

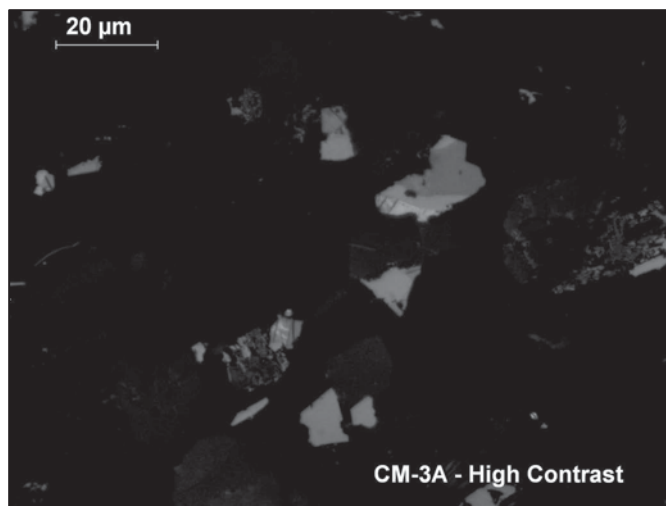


Figure 5.30: Sample NM-CM3A observed with an optical microscope in reflected light at high contrast, objective x100. Scale bar is 20 μm .

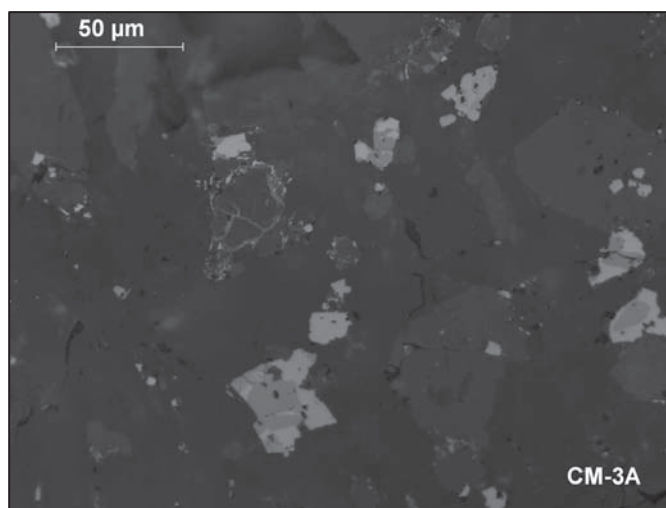


Figure 5.31: Sample NM-CM3A observed with an optical microscope in reflected light at high contrast, objective x50. Scale bar is 50 μm .

In the New-Mexico dyke sample, there are large olivine olivines, shown as gray in Figure 5.28 and Figure 5.29. These crystals have titanomagnetite (light minerals) on their border, indicating that titanomagnetites began to crystallize at the end of the crystallization of olivine minerals. Titanomagnetites are small ($\sim 20\ \mu\text{m}$) with a narrow size range. Figure 5.30 and Figure 5.31 show a magnified view of titanomagnetites. In

Figure 5.30, there are three different shades of gray inside the crystal. They are distributed in zones with clear borders in the grain. The same behavior is observed in Figure 5.31.

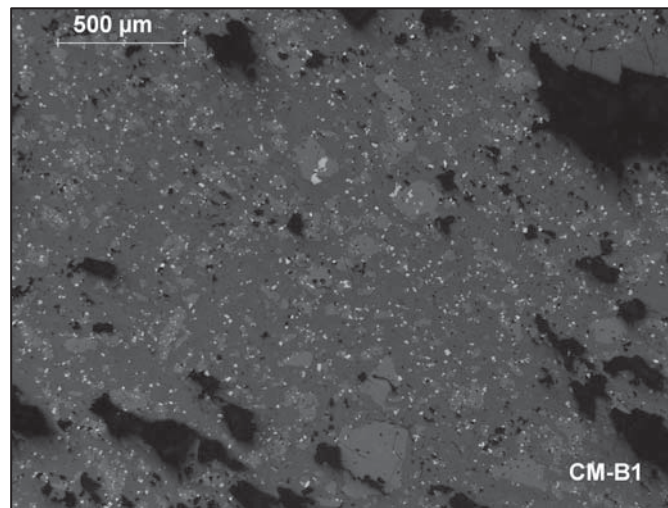


Figure 5.32: Sample NM-CMB1 observed with an optical microscope in reflected light, objective x5. Scale bar is 500 μm.

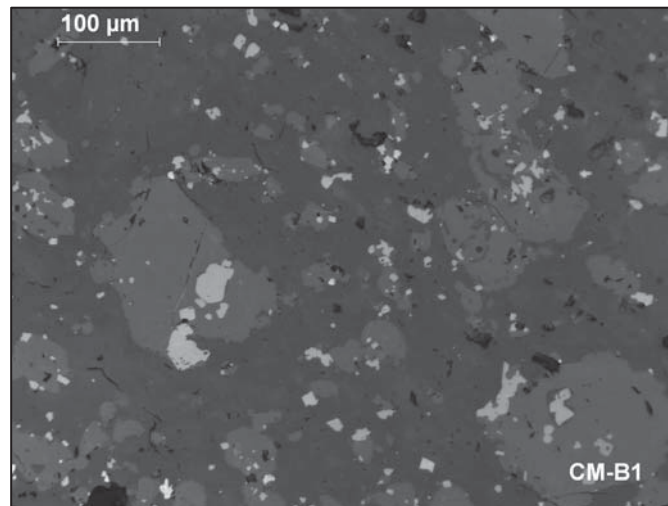


Figure 5.33: Sample NM-CMB1 observed with an optical microscope in reflected light, objective x20. Scale bar is 100 μm.

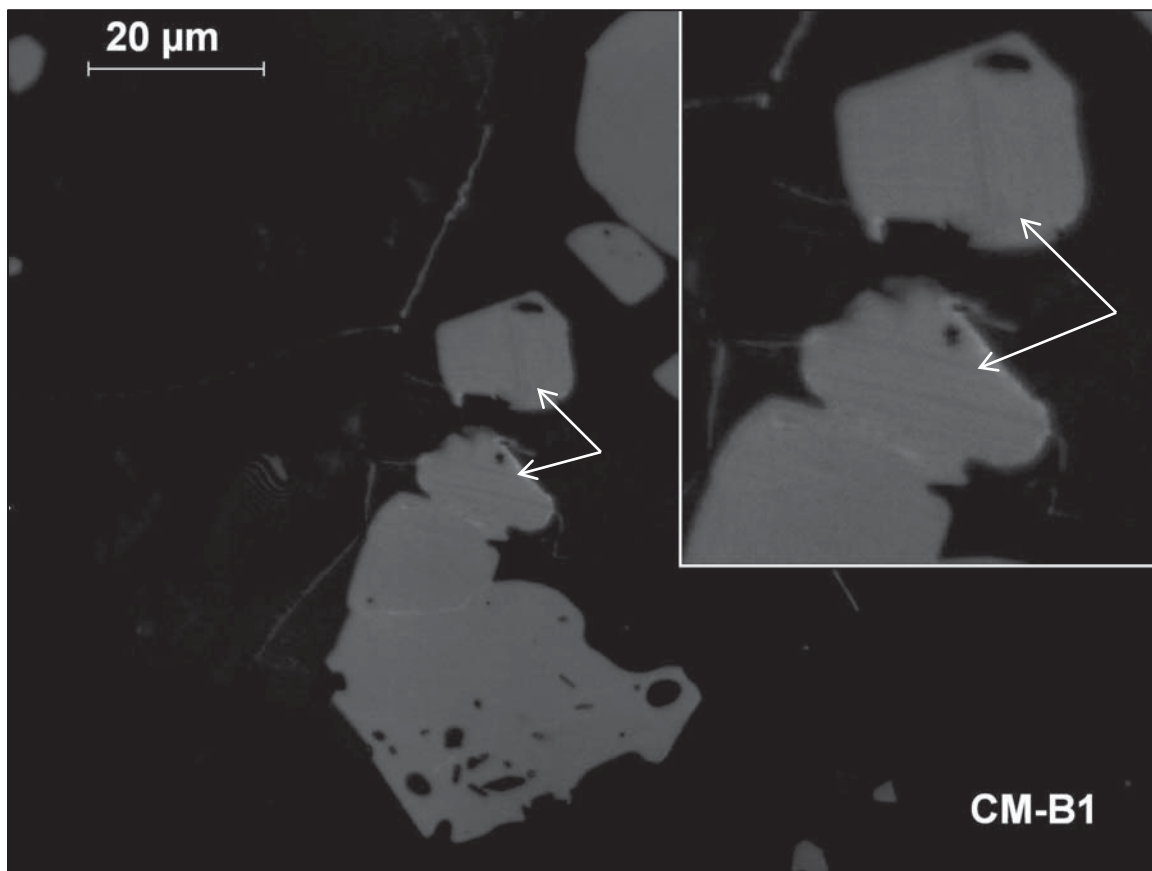


Figure 5.34: Sample NM-CMB1 observed with an optical microscope in reflected light at high contrast, objective x100. Scale bar is 20 μm. A magnification of very thin exsolutions in the titanomagnetite is on the white box both denoted by arrows.

Sample NM-CMB1 contains smaller grains of titanomagnetite (Figure 5.32). These are located inside other minerals and crystallized before and/or at the same time as other minerals (Figure 5.33). They are generally smaller than 10 μm in size, with a few exceptions being close to 50 μm. A more detailed image of one titanomagnetite grain (Figure 5.34) shows two different shades of gray. There are very thin lighter stripes denoted by white arrows. These exsolutions have different orientations and are thinner than 1 μm.

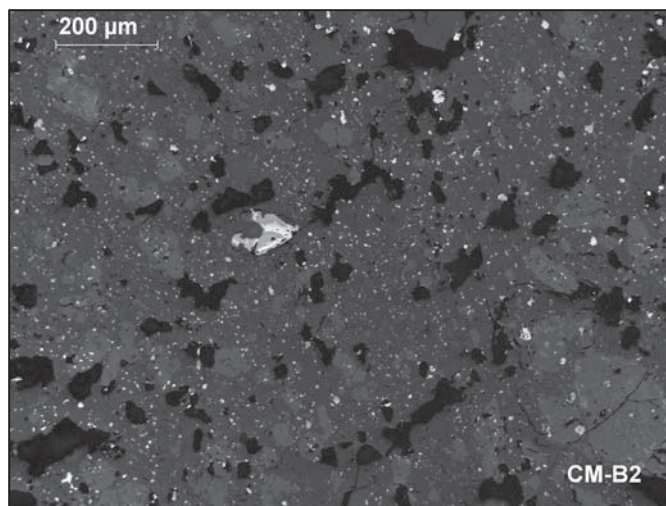


Figure 5.35: Sample NM-CMB2 observed with an optical microscope in reflected light, objective x10. Scale bar is 200 μm.

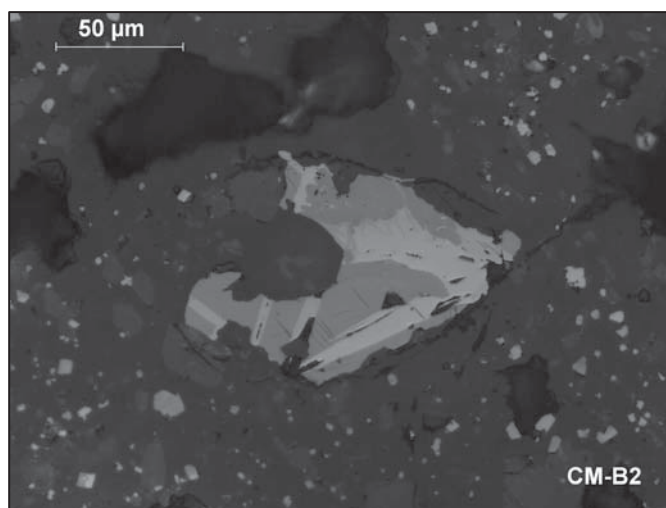


Figure 5.36: Sample NM-CMB2 observed with an optical microscope in reflected light at high contrast, objective x50. Scale bar is 50 μm.

In sample NM-CMB2, titanomagnetites are basically the same size as in NM-CMB1 but more abundant (Figure 5.35). Titanomagnetites show different shades of gray. Figure 5.36 shows four distinct grays on the image with regular exsolution pattern on the bottom of this mineral, and irregular margins between different compositions on the top part of the mineral.

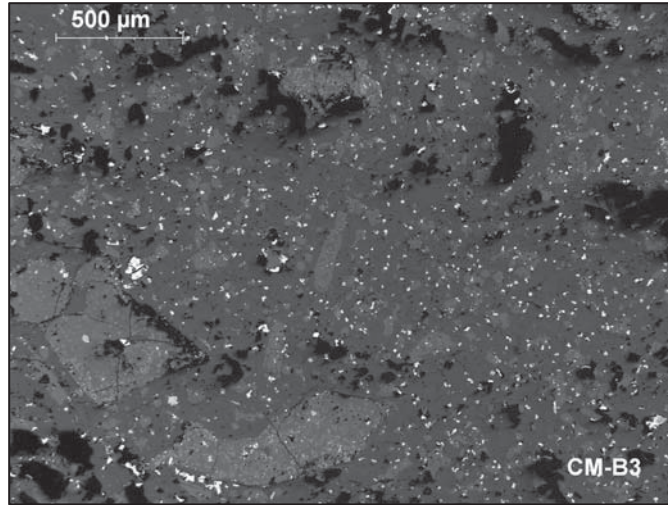


Figure 5.37: Sample NM-CMB3 observed with an optical microscope in reflected light, objective x5. Scale bar is 500 μm.

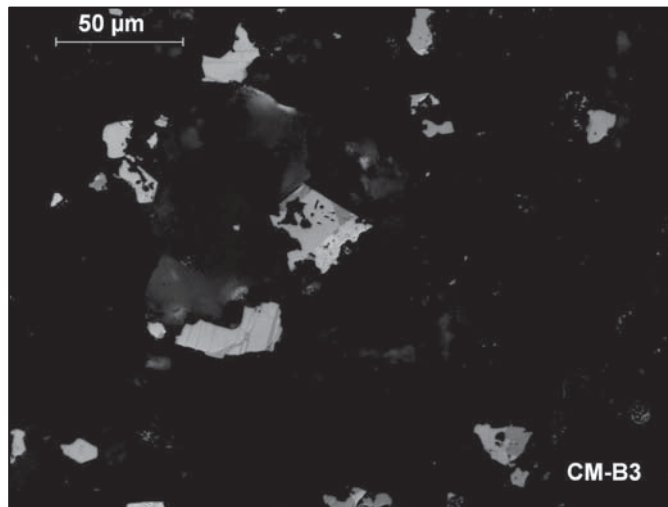


Figure 5.38: Sample NM-CMB3 observed with an optical microscope in reflected light at high contrast, objective x50. Scale bar is 50 μm.

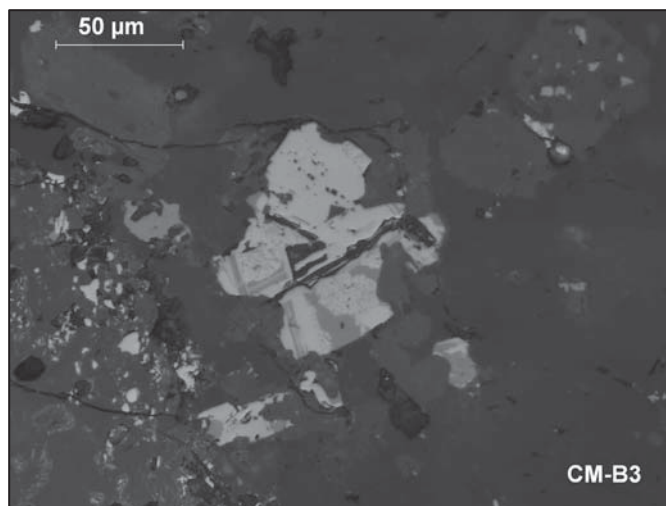


Figure 5.39: Sample NM-CMB3 observed with an optical microscope in reflected light at high contrast, objective x50. Scale bar is 50 μm.

Titanomagnetites are slightly bigger in this sample (Figure 5.37). Different shades of gray are visible inside some grains. Figure 5.38 shows titanomagnetites around 40 μm in size. The crystal in the middle presents three different compositions distributed in zones. Just under this grain there is a titanomagnetite grain which presents two different grays, indicating two compositions with striped organization. Figure 5.39 shows titanomagnetite with three different compositions. These striped exsolutions are particularly noticeable on the bottom of the grain.

The optical microscope analysis indicates that every sample from La Cienega presents multiphase titanomagnetites. These minerals present exsolution lamellae-like (samples NM-CMB1 and NM-CMB2) and zoned exsolutions (samples NM-CM3A and NM-CMB3).

5.4. Scanning Electron Microscope

Thunder Bay, Canada

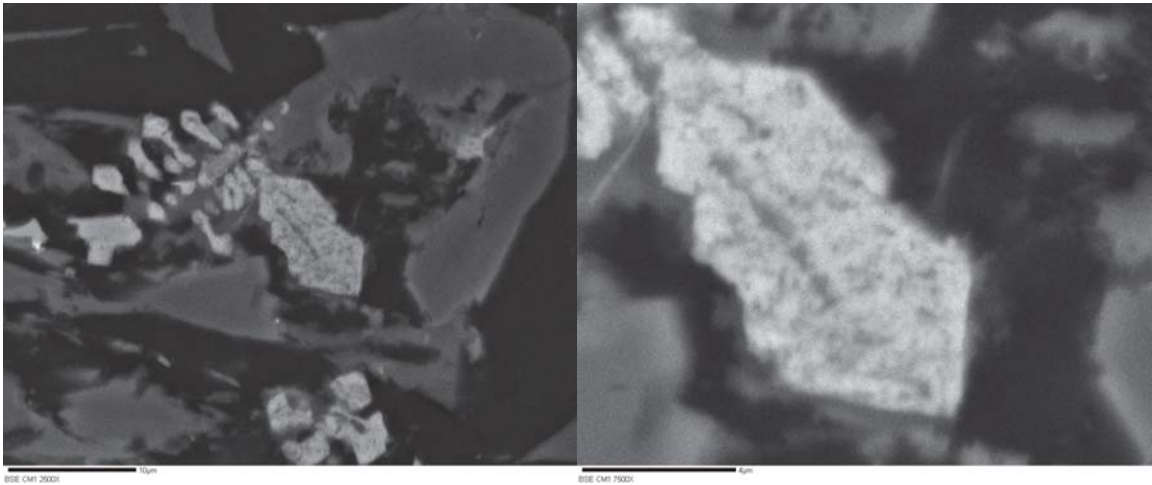


Figure 5.40: Back Scattered Electron Image (BEI) of the multiphase titanomagnetite in TB-CM1 sample. Scale bars are 10 μm on the left and 4 μm on the right.

TB-CM1 presents dendritic forms of titanomagnetite (light minerals on BSE images) (Figure 5.40). On the Figure 5.40, there is a big dendrite at around 20 μm and a small one (bottom of the left image) presenting a cruciform type. Although the resolution of the image is poor, variations in color gray can be seen inside the titanomagnetite mineral, suggesting different compositions. During the analysis the BSE image was compared to the SE image in order to check if topographic effect influences the BSE image. Additional analyses of this sample are presented in Figure 5.41.

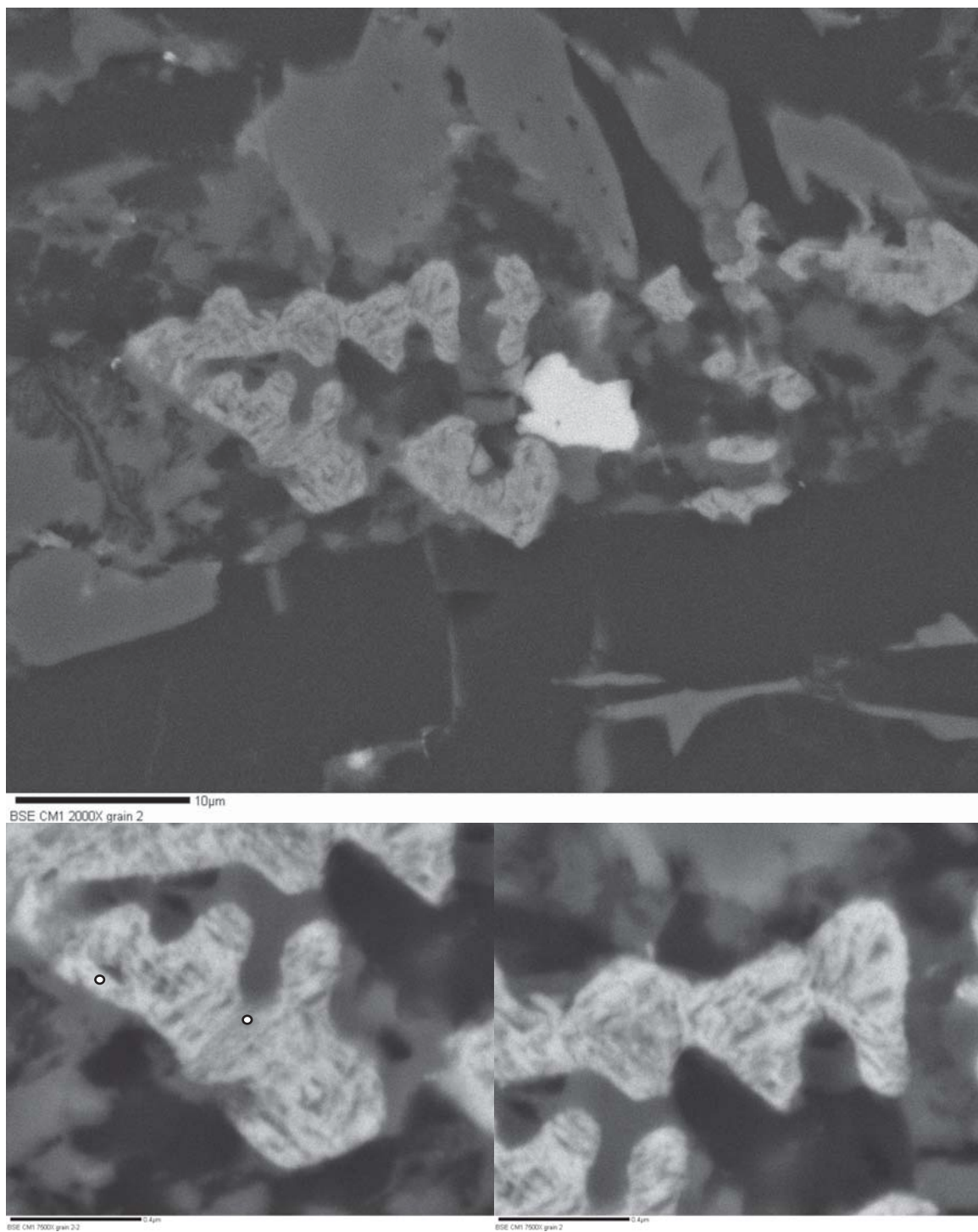


Figure 5.41: BEI of the multiphase titanomagnetite in TB-CM1 sample. Points on the image indicate the locations of EDS spectra analysis of the different phases (see Appendix 8.1). Scale bars are 10 μm on the top and 4 μm on both images on the bottom.

This dendrite at also around 20 μm shows different phases on the mineral. The lightest colored mineral in the middle of the top image (Figure 5.41) shows a high concentration of sulfur on the EDS spectrum. On the titanomagnetite, different phases show two main directions, oriented $\sim 55^\circ$ and $\sim 140^\circ$ on these images. Lamellae in this mineral are not regular and show an advanced oxidation of titanomagnetites (Haggerty 1991; Ramdohr 1980). EDS analysis suggests a very close composition between the darkest and lightest phases. The iron represents around 65 weight % of the mineral and titanium 25 weight % corresponding to a TM60. Also different phases are very small in size making the precise analysis of composition difficult. Moreover, not only the surface of the mineral is analyzed during the EDS analysis (Chapter 2.2). The measurement of the composition is mostly an average between the lightest and darkest part, giving the composition of the total titanomagnetite.

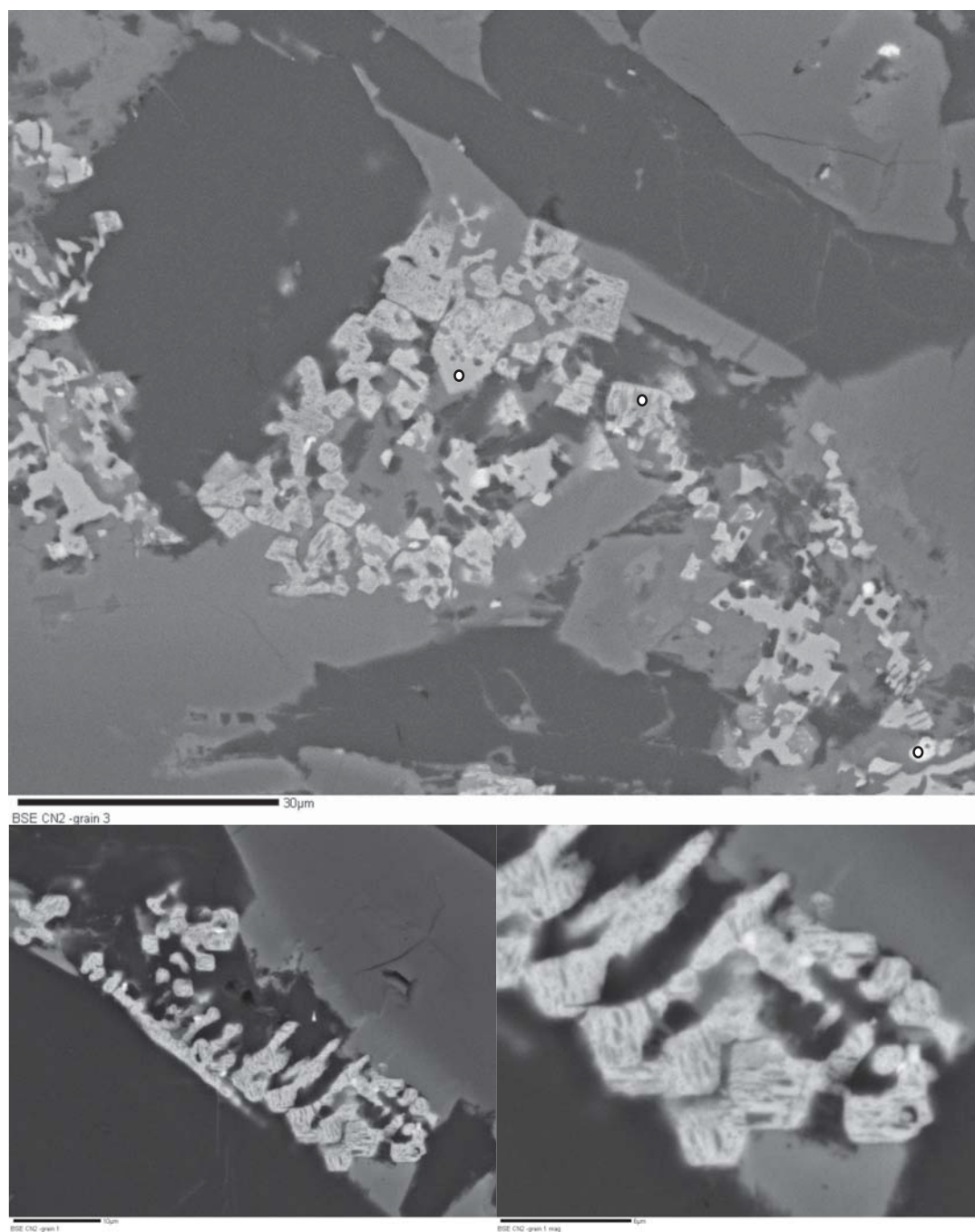


Figure 5.42: BEI of the multiphase titanomagnetite in TB-CN2 sample. Points on the image indicate the locations of EDS spectra analysis of the different phases (see Appendix 8.2). Scale bars are 30 μm on the top and 10 μm and 6 μm on both bottoms left and right.

Dendrites on the sample TB-CN2 are around 20 μm in size sometimes regrouped to form a heap (top of Figure 5.42). Titanomagnetite minerals on this sample show two different oxidation stages. On the top, there is sandwich type exsolutions (Haggerty 1991) presenting a range of gray from TM12 for the dark part (81 weight % of iron and 9 weight % of titanium from EDS analysis, Appendix 8.2) to approximately TM65 for the lightest part (38 weight % of iron and 15 weight % of titanium with a small amount of copper and sulfur). Some of these minerals show a non-homogeneous composition inside of the crystal with irregular exsolutions presenting a higher stage of oxidation. Dark exsolutions present around 38 weight % of iron and 15 weight % of titanium corresponding to a TM20.

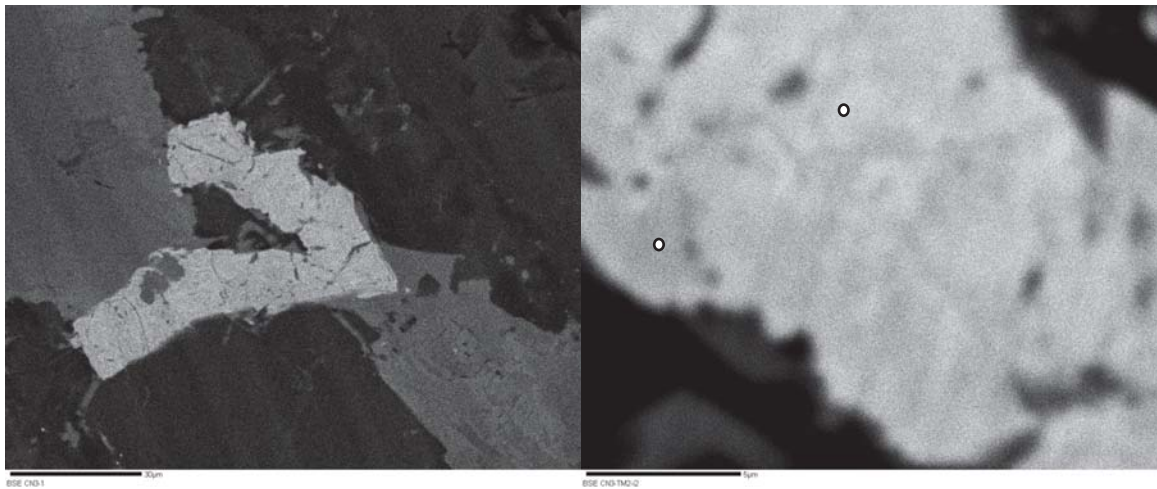


Figure 5.43: BEI of the multiphase titanomagnetite in TB-CN3 sample. Points on the images indicate the locations of EDS spectra analysis of the different phases (see Appendix 8.3). Scale bars are 30 μm on the left and 5 μm on the right.

Minerals on TB-CN3 do not have a dendritic form. Apparently, the cooling of the rock and the crystallization of minerals took longer time. The Figure 5.43 on the left shows a titanomagnetite with a size around 40 μm containing a visible microstructure with a $\sim 20^\circ$ angle on the right BSE image. The range of grays is narrow in this mineral. As for some other samples, the microstructures are very small and do not permit a differentiation

on the EDS analysis. The total composition of the titanomagnetite is around 74 weight % of iron and 17 weight % of titanium which is close to TM30. In this rock, other titanomagnetites show a gradual change of their composition on the mineral without a sharp border (Figure 5.44). The titanomagnetite shows a range of gray lighter on the left than on the right caused by a composition richer in iron on the left. EDS analysis confirmed this result and shows a composition 52 weight % of iron and 40 weight % of titanium on the dark part. The amount of iron increases gradually toward the left border with a composition close to TM20 (80 weight % of iron and 14 weight % of titanium present on this part). In the middle, the composition shows 74 weight % of iron and 17 weight % of titanium, corresponding to TM30.

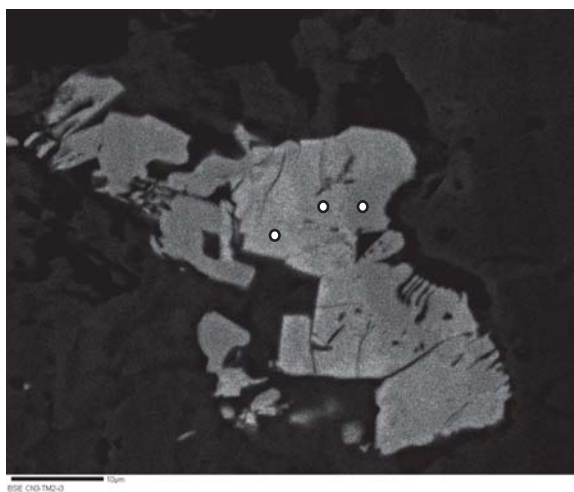


Figure 5.44: BEI of the multiphase titanomagnetite in TB-CN3 sample. Points on the images indicate the locations of EDS spectra analysis of the different phases (see Appendix 8.4). Scale bars are 10 μm .

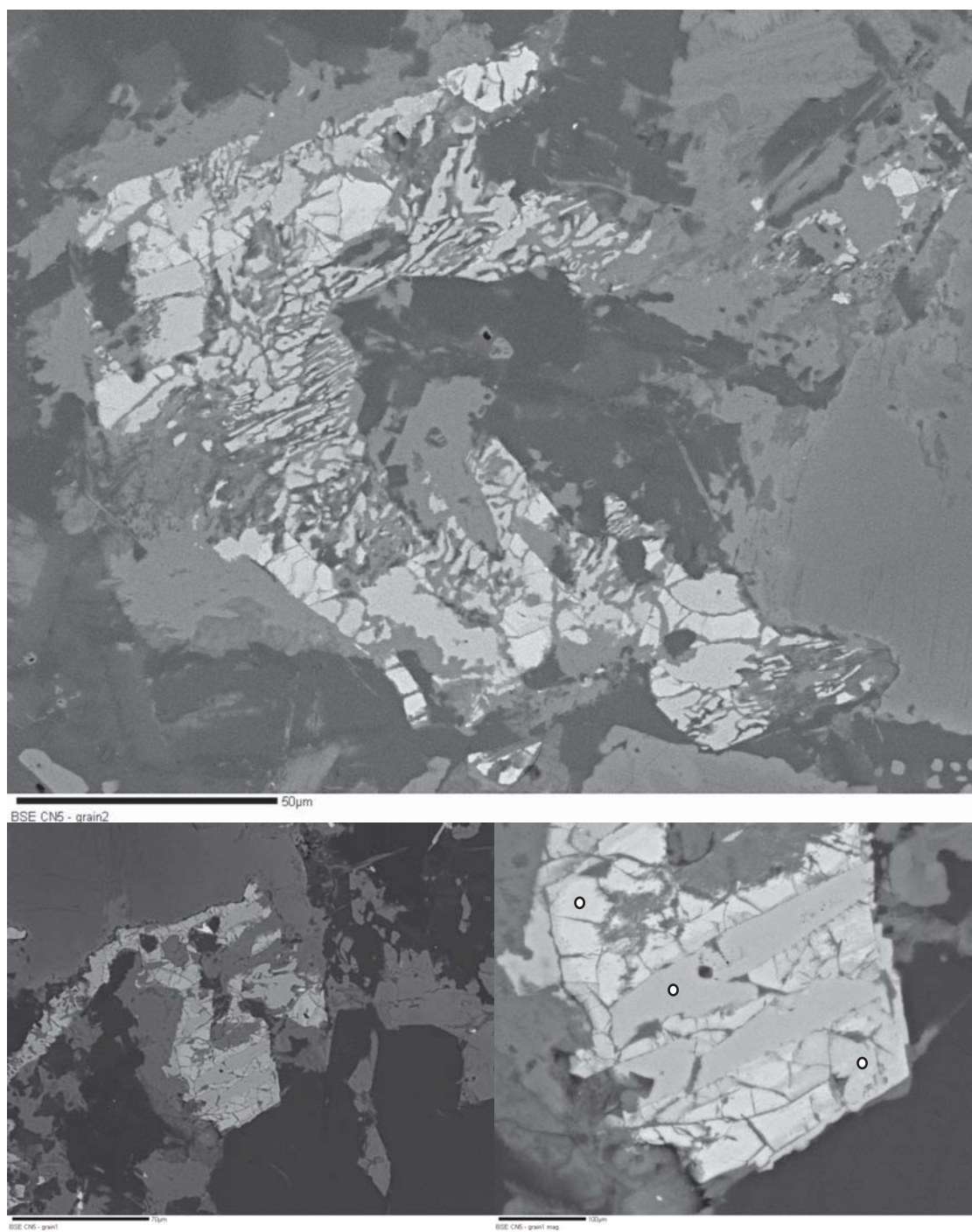


Figure 5.45: BEI of the multiphase titanomagnetite in TB-CN5 sample. Points on the image indicate the locations of EDS spectra analysis of the different phases (see Appendix 8.5). Scale bars are 30 μm on the top and 70 μm and 10 μm on both bottoms left and right.

The sample TB-CN5 contains larger grains than other samples with the grain sizes at around 80-100µm, consistent with the location of the sample on the middle of the dyke. There are two distinct phases: The first has numerous fractures and the second is in lath-shape inside of the grain (Figure 5.45). The fractured portion presents a gradual change in the range of gray from a light part close to TM5 (87 weight % of iron and 5 weight % of titanium) to a dark part close to TM25 (71 weight % of iron and 14 weight % of titanium). The lath-shape shows an organization as sandwich-type of exsolutions without fractures and a composition around TM15 (84 weight % of iron and 10 weight % of titanium).

Because of these systematic different compositions with a phase Ti-poor titanomagnetite and a phase magnetite, the supposition of a mix of compositions is possible. The relative small amount of titanium within dark color phases on SEM image leads to the possibility of ilmenite within Thunder Bay sample. So there is a mix of composition with a transfer of cation between a phase close to ulvospinel and magnetite to create an intermediate phase TM40.

La Cienega, New-Mexico

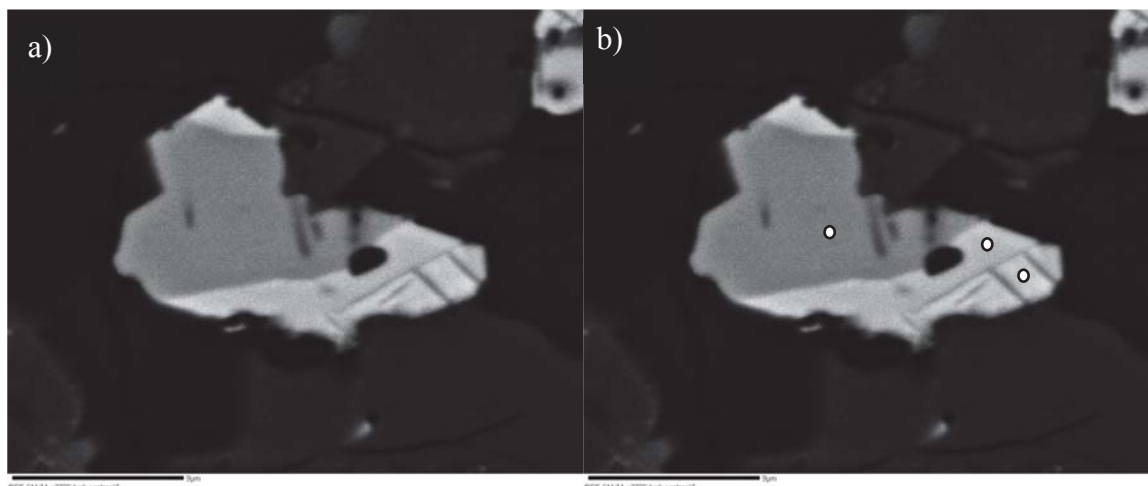


Figure 5.46: BEI of the multiphase titanomagnetite in NM-CM3A sample. Points on the image b indicate the locations of EDS spectra analysis of the different phases (see Appendix 8.6). Scale bars are 9 μm .

During the SEM analysis, exactly the same grain in NM-CM3A (Figure 5.46) was found as during the optical microscope analysis (Figure 5.30). There is three different phases in the titanomagnetite grain presenting sandwich-type exsolution (Haggerty 1991). A quantitative analysis of the composition was done by EDS analysis on each different phase of the grain (white points on Figure 5.46b). The EDS data are shown in Appendix 8.6. The darkest part shows an almost equal amount of iron and titanium (45 weight % and 44 weight % respectively). Carbon and magnesium are present in very small amounts. The medium gray shows a higher concentration of iron and a smaller concentration of titanium (57 weight % and 18 weight % respectively) corresponding to TM45. There is a considerable amount of silicon in this part of the mineral representing around 8 weight %. The lightest part is mainly composed of iron with around 90 weight %. The titanium presents a very small amount and its quantity is too small in comparison to the error of this analysis to be considered.

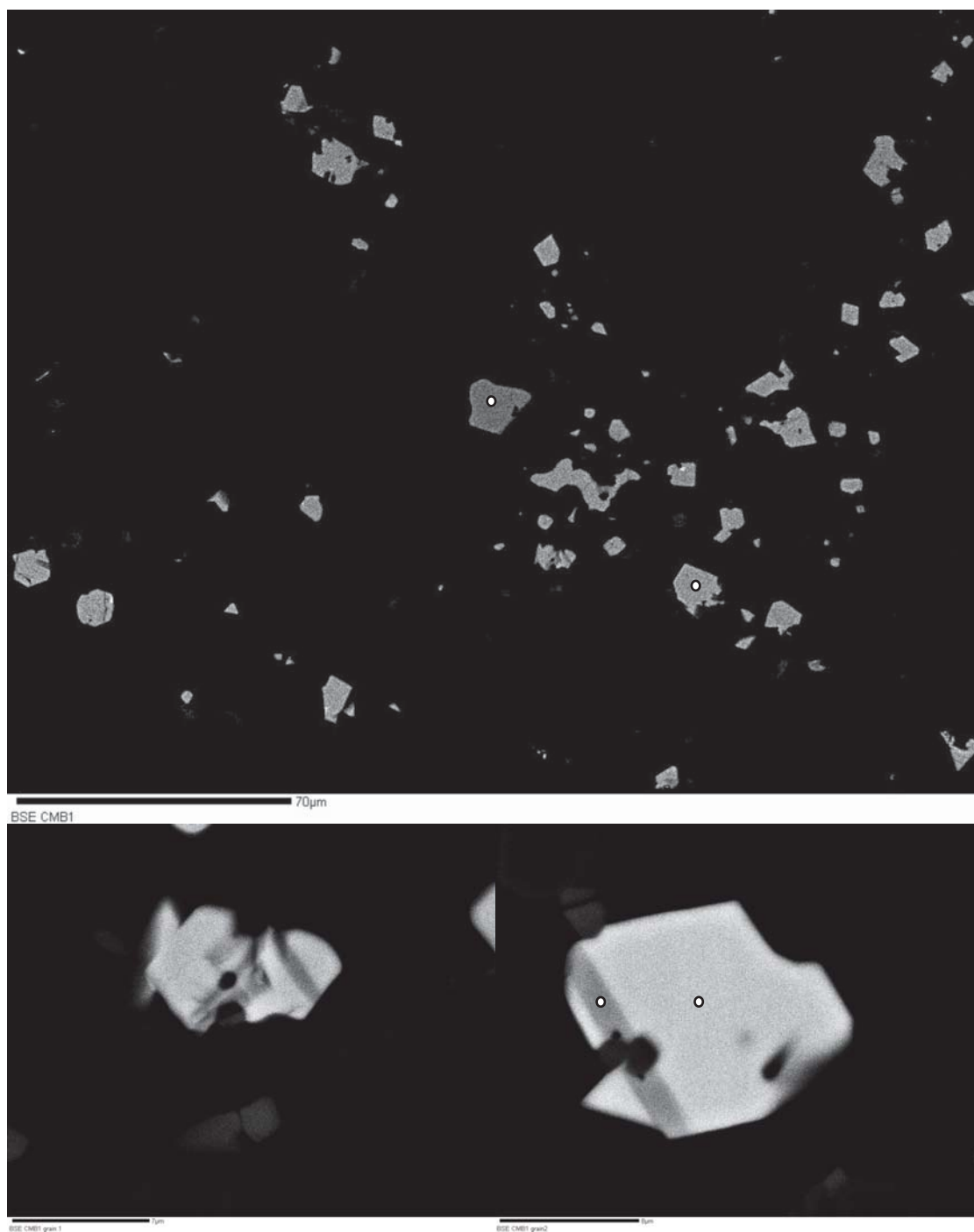


Figure 5.47: BEI of the titanomagnetites in NM-CMB1 sample. Points on the image indicate the locations of EDS spectra analysis of the different phases (see Appendix 8.7 and 8.8). Scale bars are 70 μm on the top and 7 and 8 μm on bottom left and right respectively.

In the sample NM-CMB1, the titanomagnetite grains show a homogeneous composition and/or exsolution pattern. On the top image of the Figure 5.47, we can see homogeneous minerals of titanomagnetite of around 20 μm in size showing different shade of gray. Two of them are analyzed by EDS (Appendix 8.7) showing a larger amount of iron in the lightest mineral. The composition is gradual from close to TM20 for lightest mineral (75 weight % of iron and 14 weight % of titanium) to a composition close to TM50 for darkest minerals.

On the same Figure 5.47, smaller titanomagnetites present different compositions inside the grain. Figure 5.47 shows sandwich-type exsolutions in some grains. The different composition between the light part close to TM15 (78 weight % of iron and 11 weight % of titanium) and the dark part close to ilmenite (47 weight % of iron and 26 eight % of titanium) shows an oxidation of titanomagnetites.

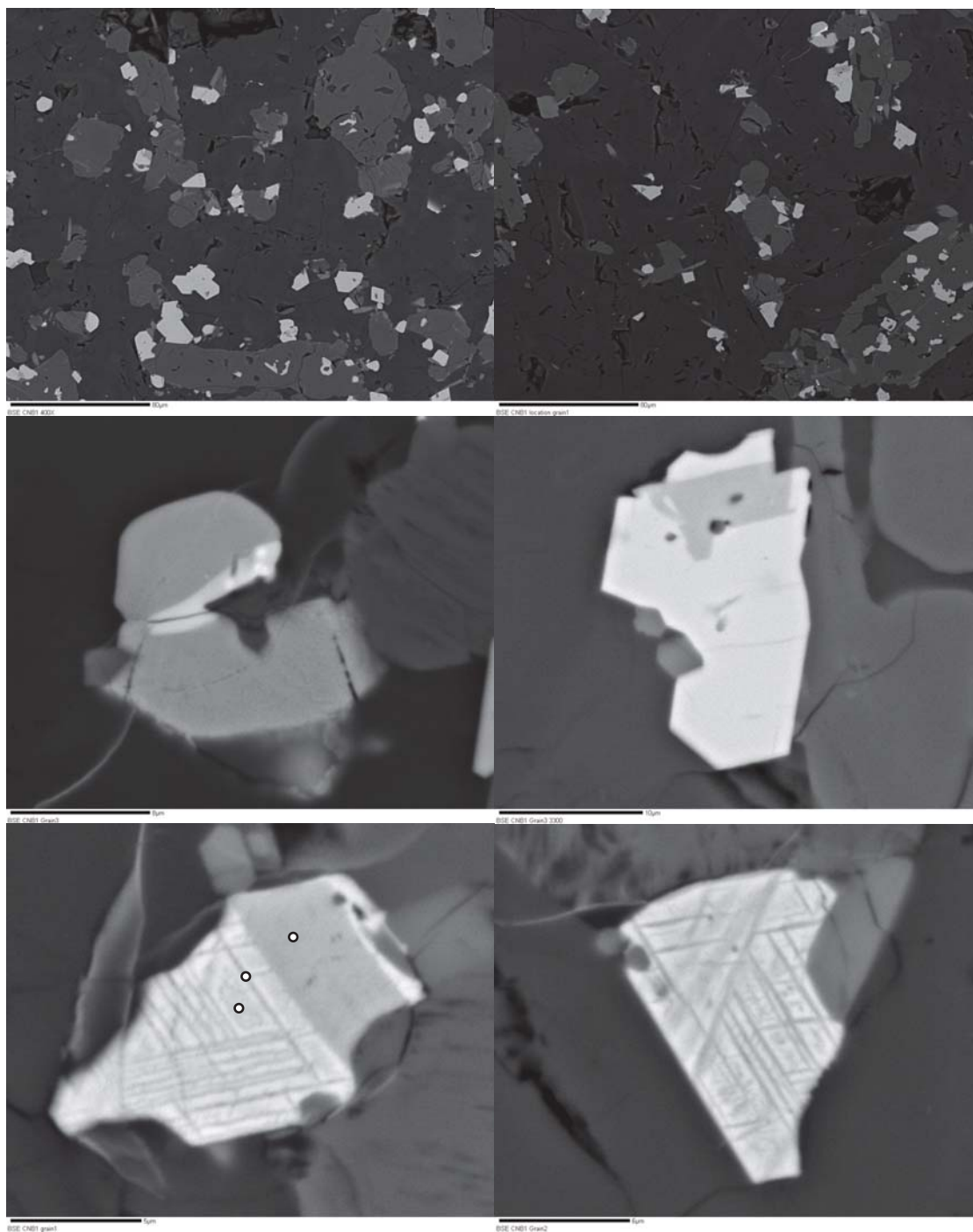


Figure 5.48: BEI of the multiphase in titanomagnetites in NM-CMB1 sample. Points on the image indicate the locations of EDS spectra analysis of the different phases (see Appendix 8.9). Scale bars are 80 μm on the top and 8 and 10 μm on middle, 5 μm and 6 μm on the bottom left and right respectively.

As seen previously, NM-CMB1 presents titanomagnetites with a homogeneous composition or with sandwich type exsolutions (Figure 5.48 top and middle row). Some smaller grains present more complex microstructure (Figure 5.48 bottom row). There is the trace of oxidation by the sandwich-type exsolutions. Thinner lamellae on these minerals present two main directions concordant with larger exsolution stripe. This lamellae-type exsolution shows another and higher stage on the oxidation of the rock than sandwich-type exsolutions. EDS analysis presents the same composition on the large and thinner exsolutions with 47 weight % iron and 41 weight % titanium. The light colorpart has a composition with more iron (78 weight %) than titanium (13 weight %) corresponding to TM20. In some titanomagnetites, a very small scale structure can be seen and makes their analysis difficult. It could be called parquet-texture created at the beginning of equilibration of element between ulvospinel and magnetite (Haggerty 1991). Because of the size and the relatively small resolution of images compared to these microstructures, EDS analysis are impossible.

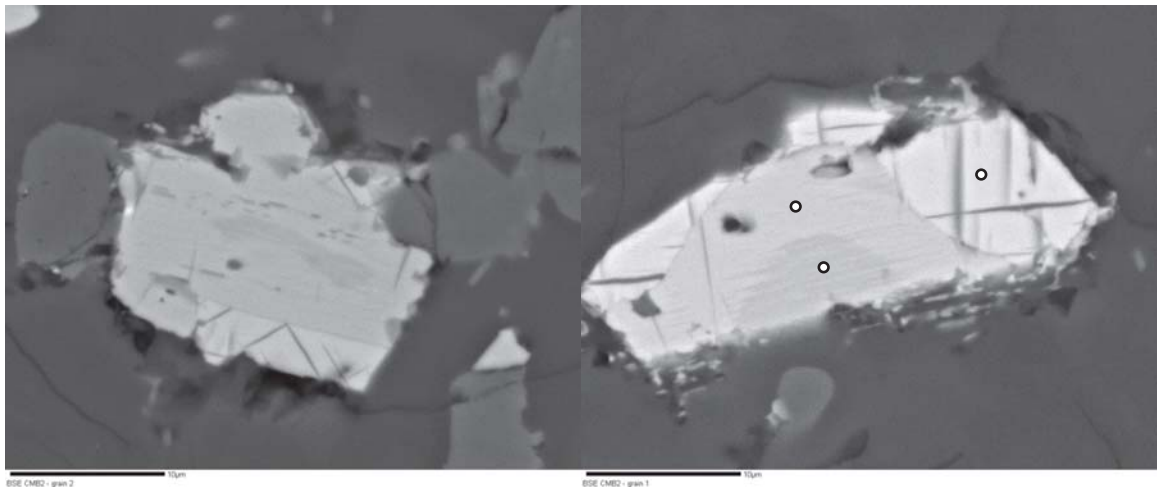


Figure 5.49: BEI of a multiphase titanomagnetite in NM-CMB2 sample. Points on the image b indicate the locations of EDS spectra analysis of the different phases (see Appendix 8.10). Scale bars are 10 μm .

In the Figure 5.49, there are two grains of NM-CMB2 showing the same structure in two phases with numerous fractures in the lightest phase. It presents a composition of pure iron with only a very little amount of titanium which can be negligible (91 weight % of iron and 0.8 weight % of titanium by EDS analysis). The second part of these minerals shows a range of color with mainly two colors corresponding to a composition TM5 with a very small amount of titanium (89 weight % of iron and 4 weight % of titanium) and a composition TM60 (66 weight % of iron and 25 weight % of titanium). This part divided in two phase shows smaller exsolutions.

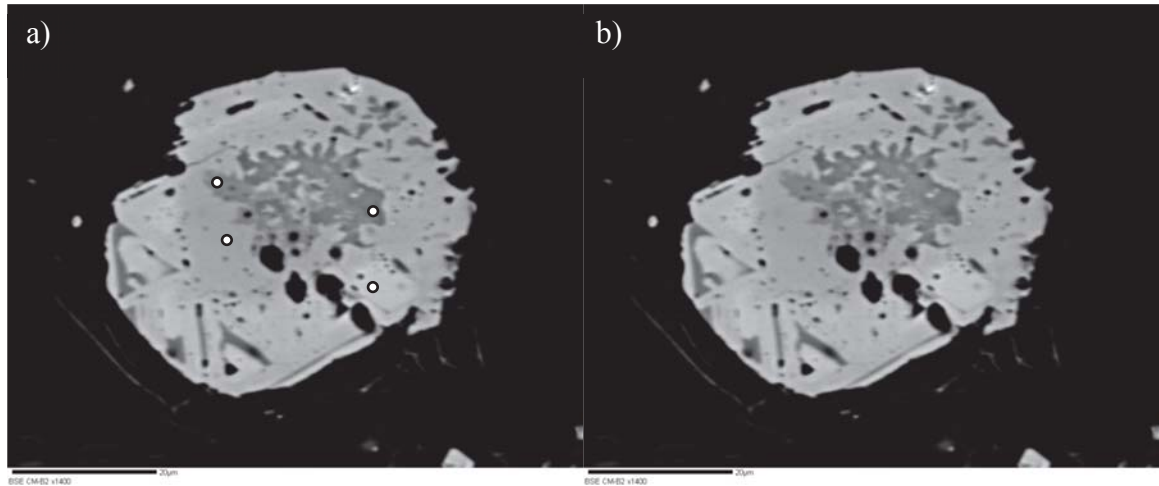


Figure 5.50: Back Scattered Electron Image (BEI) of a multiphase titanomagnetite grain in NM-CMB2 sample. Points on the image (a) indicate the locations of EDS spectra analysis of the different phases (see Appendix 8.11). Scale bars are 20 μm .

The grain from NM-CMB2 shows two stages of oxidation (Figure 5.50). There are sandwich type exsolutions with sharp border on the bottom left of the mineral. The other part of the mineral shows exsolutions with irregular borders which can indicate a higher degree of oxidation in the rock. Very small bright points correspond to polish particles. Four different shades of gray on this titanomagnetite mineral were analyzed by EDS available in the Appendix 8.11. The darkest phase of this grain has a composition rich in iron with 82 weight % and contains titanium at 9 weight % corresponding to

TM12. The second darkest phase correspond to TM25 with a smaller amount of iron (76 weight %) and more titanium (16 weight %). This corresponds to titanomagnetite at 18% Ti. For the second lightest gray phase, iron is still the dominating element with 86 weight % of the composition. The titanium is present at 7 weight %. This corresponds to titanomagnetite poor in titanium, TM8. The amounts of other elements are negligible. The lightest phase of the grain contains mainly iron at 96 weight % of the composition. The titanium is present in very small quantity (1 weight %) negligible. This phase of this mineral is almost pure magnetite.

The average titanomagnetite composition is more Ti-poor for La Cienega sample. Sample NM-CM3A shows three different compositions of exsolutions. Samples NM-CMB1 and NM-CMB2 show different compositions in the same grain and different organization between grains. They are mainly composed of iron but show a bigger amount of titanium on exsolutions. Sample NM-CMB2 shows a more evolved stage of oxidation than sample NM-CMB1. Except sample NM-CMB1, both samples show a relative same composition and separation of phases. There a phase Ti-rich close to ilmenite composition and a phase pure iron close to pure magnetite. An intermediate phase can correspond to TM40 seen on thermomagnetic analysis. The supposition did by interpretation of thermomagnetic curves of unmixing of compositions of a phase TM40 is possible but need further investigation to be identified. Also the sample NM-CMB1 presented a different thermomagnetic curve suggesting a mix of composition. SEM analysis shows different exsolution with a Ti-rich composition, close to ilmenite, and a Ti-poor composition suggesting a possible a possible mix.

6. Conclusions

The magnetic and microscopy analyses performed in this study showed significant differences in magnetic properties and oxidation of Fe-Ti oxides between the two studied dyke-lava flow systems. The differences between the dyke and flow within each system are less dramatic except for one sample (NM-CMB1) from New Mexico.

The dyke and lava flow from Thunder Bay exhibit the smallest but still noticeable difference in magnetic mineralogy and behavior. Although both dyke and lava flow samples manifest single-domain magnetic behavior, the former contains slightly larger magnetic grains (as seen by their shift towards the PSD region on the Day plot; Figure 5.4). This behavior is consistent with slightly slower cooling rate for the six meter wide dyke than for the two meter wide lava flow. Nevertheless, for both dyke and flow, the cooling rate is similar (both are estimated to cool to room temperature within several days). The relatively fast cooling rate is also consistent with primarily dendritic shape of Fe-Ti oxide grains observed in all samples from Thunder Bay. Many Fe-Ti oxide grains from both dyke and flow contain intergrowths of magnetite and nearly ilmenite phases produced as a result of deuteric oxidation (oxyexsolution) during the initial cooling of magma. Our thermomagnetic analyses suggest that these two phases start to mix back to a more homogeneous titanomagnetite composition upon heating to 700°C. However, heating to 600°C does not result in significant changes in magnetic mineralogy of the samples. Because the maximum temperature during paleointensity experiments does not exceed 580°C, it is concluded that the Thunder Bay rocks are suitable for paleointensity investigation.

Despite the younger age, the dyke and lava flow from La Cienega are more different in their magnetic mineralogy and behavior. Unfortunately, due to the lack of field information, it was impossible to estimate the cooling rates for these rocks. However, typically these rates should not be dramatically different from those estimated for the Thunder Bay rocks. The magnetic hysteresis data show that the samples contain a wider range of magnetic domain states and, in the case of the vent sample, a bimodal

mixture of superparamagnetic and single-domain grains. The SEM analyses show the presence of different oxidation states of Fe-Ti oxides even within a single specimen which is consistent with the magnetic hysteresis data. The thermomagnetic analyses that, in contrast to the Thunder Bay samples, the Fe-Ti oxide grains from La Cienega undergo further unmixing of relatively homogeneous titanomagnetite into at least two, Ti-rich and Ti-poor phases. The irreversible character of thermomagnetic curves indicates that the rocks for la Cienega are not suitable for paleointensity analyses.

Overall, this study has shown that the relationships between the magnetic and mineralogical properties of dyke-flow systems are complex and cannot be generalized. Accordingly, every paleointensity investigation should be accompanied by mineralogical and petrological analyses to estimate the possible effect on paleointensity determinations such as the presence of thermochemical magnetization due to oxyexsolution (Smirnov and Tarduno 2005). Although no dramatic differences in magnetic mineralogies between the dyke and flow within each system have been identified by this study, the effect of different cooling histories and magnetic mineral assemblages between basaltic flows and mafic dykes cannot be ruled out as an explanation for the systematic differences in paleointensity values. For example, thermal cycling up to the Curie temperature used during paleointensity experiments may lead to laboratory alteration of magnetic minerals and, hence, to a paleointensity bias. Our results hint that such a laboratory alteration is more expressed in lava flows, perhaps due to the difference in magnetic grain sizes.

This study represents a first step towards understanding the systematic paleointensity bias between mafic dykes and lava flows. However, based on the obtained results, some strategies for future research can be formulated. Most importantly, additional dyke-flow systems should be investigated with more samples per site analyzed in order to produce representative datasets. The mineralogical and magnetic analyses should be accompanied by paleointensity determinations so that the paleofield discrepancies, if any, can be directly compared to the observed magnetic mineralogy. Finally, useful insights can be obtained from direct observations of the heating-induced mineralogical changes using SEM.

7. References

- Akimoto S, Katsura T, Yoshida M. 1957. Magnetic properties of $\text{TiFe}_2\text{O}_4\text{-Fe}_3\text{O}_4$ system and their change with oxidation. *Journal of Geomagnetism and Geoelectricity*. 9:165-178
- Arculus RJ, Powell RP. 1986. Source component mixing in the regions of arc magma generation. *Journal of Geophysical Research*. 91:5913-5926
- Aubele JC. 1979. Cerros del rio volcanic field. *New Mexico Geological Society*. 243-252
- Bachman GO, Mehnert HH. 1978. New K-AR dates and the late Pliocene to Holocene geomorphic history of the central Rio Grande region, New Mexico. *Geological Society of America Bulletin*. 89:283-292
- Baldrige WS. 1978. Petrology of Plio-Pleistocene basaltic rocks from the central Rio Grande rift (New Mexico, USA) and their relation to rift structure. In Neuman ER, Ramberg IB, eds. *Petrology and geochemistry of continental rifts* 71-78
- Bleil U, Petersen N. 1979. Variations in magnetization intensity and low-temperature titanomagnetite oxidation of ocean floor basalts. *Nature*. 301:384-388
- Buddington AF, Lindsley DH. 1964. Iron-Titanium oxide minerals and synthetic equivalents. *Journal of Petrology*. 5:310-357
- Butler RF. 2004. *Paleomagnetism: Magnetic domains to geologic terranes*. Electronic edition.
- Carmichael ISE, Nicholls J. 1967. Iron-titanium oxides and oxygen fugacities in volcanic rocks. *Journal of Geophysical Research*. 72:4665-4687
- Carter MW, MacIlwaine WH, Wisbey PA. 1973. Nipigon-Schreiber sheet, Thunder Bay District. *Ontario Geological Survey, Geological Compilation Series*. Map 2232, scale 1 inch = 4 miles.

- Day R, Fuller MD, Schmidt VA. 1977. Hysteresis properties of titanomagnetites: Grain size and composition dependence. *Physics of the Earth and Planetary Interior*. 13:260-267
- Duncker KE, Wolff JA, Harmon RS, Leat PT, Dickin AP, Thompson RN. 1991. Diverse mantle and crustal components in lavas of the NW Cerros del Rio volcanic field, Rio Grande rift, New Mexico. *Contributions to Mineralogy and Petrology*. 108:331-345
- Dunlop DJ. 2002. Theory and application of the Day plot (Mrs/Ms versus Hcr/Hc) 1. Theoretical curves and tests using titanomagnetite data. *Journal of Geophysical Research*. 107(B3)
- Dunlop DJ, Ozdemir O. 1997. *Rock magnetism, Fundamentals and frontiers*. Cambridge Studies in Magnetism
- Foucher M. 2012. The anatomy of a cinder cone: Paleomagnetic, rock magnetic, structural, and petrologic data from the La Cienega volcano, Cerros del Rio volcanic field, northern New Mexico. Master thesis
- Galenko PK, Krivilyov MD. 2000. Modelling of crystal pattern formation in isothermal undercooled alloys. *Modelling and Simulation in Materials Science and Engineering*. 8:81–94
- Galenko PK, Krivilyov MD. 2009. Modeling of a transition to diffusionless dendritic growth in rapid solidification of a binary alloy. *Computational Materials Science*. 45(4): 972–980
- Goldstein JI, Yakowitz H. 1975. *Practical Scanning Electron Microscopy*. Plenum, New York.
- Graham CD. 2000. High-sensitivity magnetization measurements. *Journal of Materials Science and Technology*. 16(2):97-101

- Haggerty SE. 1978. Mineralogical constraints on Curie isotherms in deep crustal magnetic anomalies. *Geophysical research letters*. 5(2):105-108
- Haggerty SE. 1991. Oxide textures – a mini-atlas. *Oxide minerals: petrologic and magnetic significance*. 25:129-219
- Heaman LM, Easton RM, Hart TR, Hollings P, MacDonald CA, Smyk M. 2007. Further refinement to the timing of Mesoproterozoic magmatism, Lake Nipigon Region, Ontario. *Canadian Journal of Earth Sciences*, 44:1055–1086
- Heller R, Merrill RT, McFadden PL. 2002. variation of intensity of earth's magnetic field with time. *Physics of the Earth and Planetary Interiors* 131:237–249
- Hollings P, Smyk M, Heaman L, Halls H. 2010. Geochemistry, geochronology and paleomagnetism of dikes and sills associated with the Mesoproterozoic Midcontinent Rift near Thunder Bay, Ontario, Canada. *Precambrian Research*. 183:553-571
- Hrouda F, Jelinek V, Zapletal K. 1997. Refined technique for susceptibility resolution into ferromagnetic and paramagnetic components based on susceptibility temperature-variation measurement. *Geophysical Journal International*. 129(3):715–719
- Ishikawa Y, Akimoto S. 1957. Magnetic Properties of the $\text{FeTiO}_3\text{-Fe}_2\text{O}_3$ Solid Solution Series. *Journal of the Physical Society of Japan*. 12(10)
- Irvine TN, Baragar WA. 1971. Guide to the chemical classification of the common volcanic rocks. *Canadian Journal of Earth Sciences*. 8:523-545
- Kelley VC. 1952. Tectonics of the Rio Grande depression of central New-Mexico. *New Mexico Geological Society Guidebook*. 3:93-105

- Klewin KW, Shirey SB. 1992. Igneous petrology and magmatic evolution of the Midcontinent rift system. *Tectonophysics*. 213(1-2):33-40
- Lattard D, Engelmann R, Kontny A, Sauerzapf U. 2006. Curie temperatures of synthetic titanomagnetites in the Fe-Ti-O system: Effects of composition, crystal chemistry, and thermomagnetic methods. *Journal of Geophysical Research*. 111
- Lewis M. 1968. Some experiments on synthetic titanomagnetites. *Geophysical Journal International*. 16:295-310
- Lloyd GE. 1987. Atomic number and crystallographic contrast images with the SEM: a review of backscattered electron techniques. *Mineralogical Magazine*. 51:3-19
- O'Reilly W, Banerjee SK. 1967. The mechanism of oxidation in titanomagnetites: a magnetic study. *Mineralogical Magazine*. 36:29-37
- Ozdemir O, Dunlop DJ. 1993. Effect of oxidation on the Verwey transition in magnetite. *Geophysical Research Letters*. 20(16):1671
- Petersen N. 1976. Notes of the variation of magnetization within basalt lava flows and dikes. *Pageoph*. 114:177-193
- Piispa EJ, Smirnov AV, Pesonen LJ, Hollings P, Smyk M, Campbell D, Scott J. 2011. Paleomagnetism of Midcontinent Rift rocks from the northern shore of Lake Superior (Ontario, Canada): Preliminary results. *ILSG Conference*
- Pye EG, Fenwick KG. 1965. Atikokan-Lake headsheets, Kenora, Rainy River and Thunder Bay districts. Ontario Department of Mines. Geological Compilation Series. Map 2065, scale 1 inch = 4 miles.
- Ramdohr P. 1980. Ore minerals and their intergrowths. International series in earth sciences. 35 Press Frankfurt

- Readman PW, O'Reilly W. 1971. The synthesis and inversion of non-stoichiometric titanomagnetites. *Physics of the Earth and Planetary Interiors*. 4(2):121–128
- Righter K. 1997. High bedrock incision rates in the Atenguillo River valley, Jalisco, Western Mexico. *Earth Surface Processes and Landforms*. 22(4):337-343
- Righter K, Carmichael ISE, Becker TA, Renne PR. 2012. Pliocene-Quaternary volcanism and faulting at the intersection of the Gulf of California and the Mexican Volcanic Belt. *GSA Bulletin*. 107(6):612-626
- Stacey FD, Banerjee SK. 1974. *The Physical Principles of Rock Magnetism*. Elsevier, Amsterdam, 195 pp.
- Tarduno J, Smirnov AV. 2004. Paradox of low field values and the long-term history of the geodynamo. *Geophysical Monograph*. 145(135):75-84
- Tauxe L. 1998. *Paleomagnetic Principles and Practice*. Dordrecht: Kluwer Academic Publishers.
- Tauxe L. 2009. *Essentials of Paleomagnetism: Web Edition 1.0*
- Verhoogen J. 1962. Oxydation of iron-titanium oxides in igneous rocks. *Journal of Geology*. 70:168-181
- Verwey EJW. 1939. Electronic Conduction of Magnetite (Fe_3O_4) and its Transition Point at Low Temperatures. *Nature*. 144:327-328

8. Appendices

8.1. Appendix 8.1

EDS spectra of the different phases in TB-CM1 sample observed in the BEI. All the peaks are labeled on the figures and the results of the standardless analyses are shown on the bottom of each spectrum.

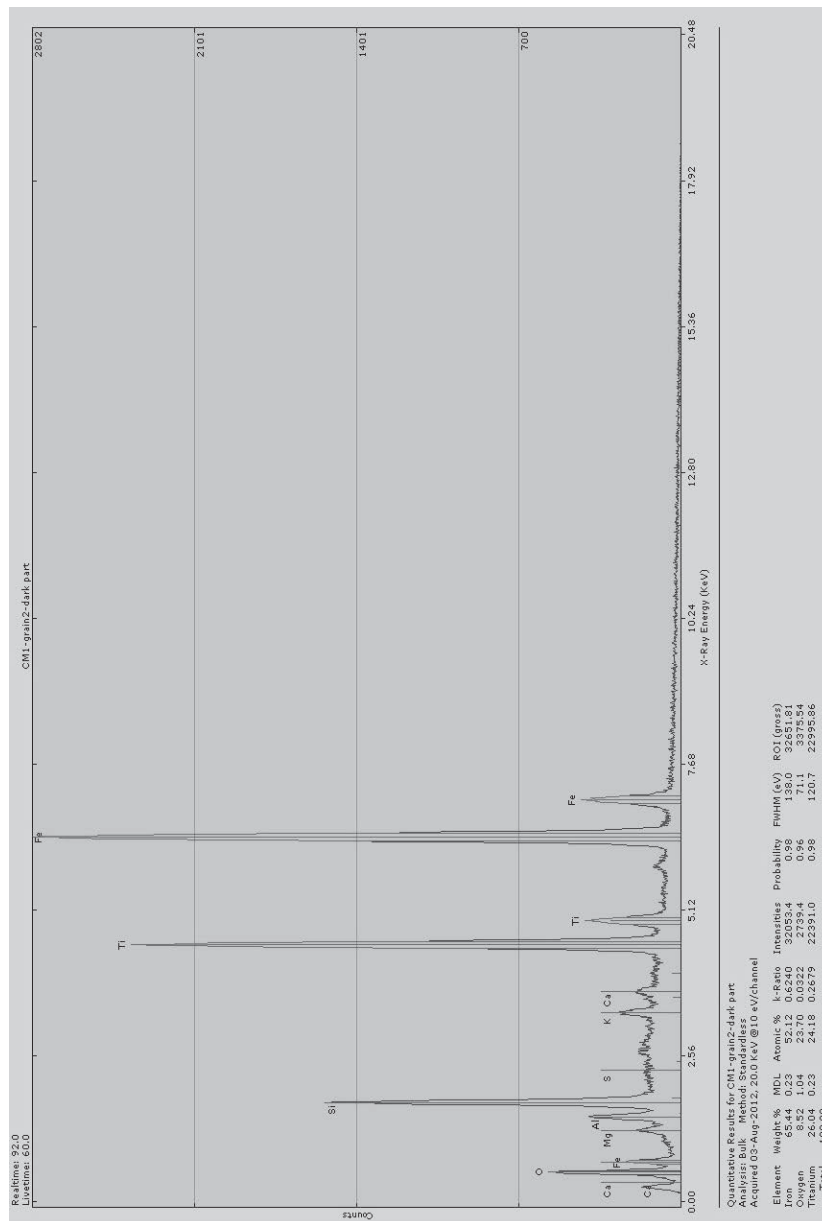


Figure 8.1: Phase #1. EDS spectra of the darkest phase of the mineral on the BEI

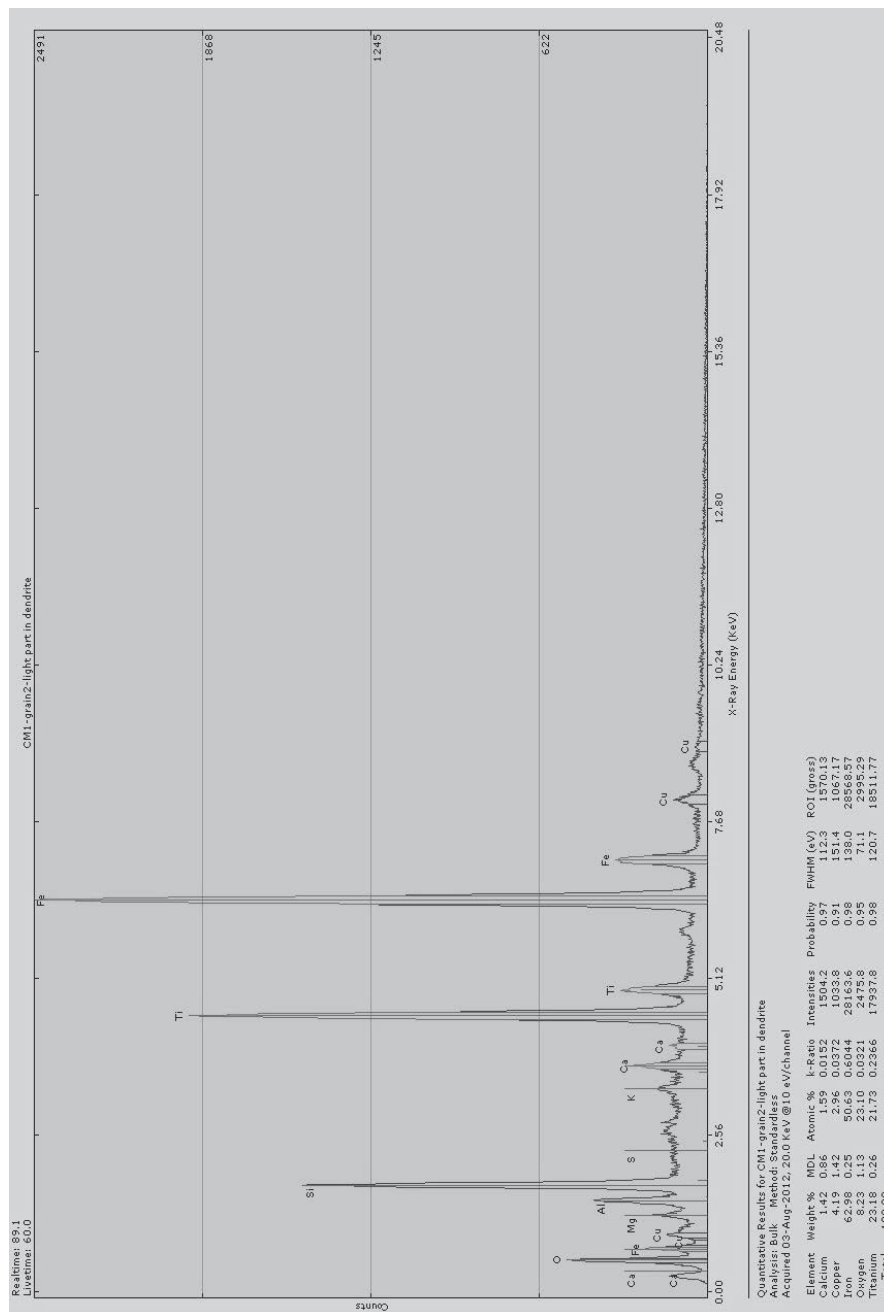


Figure 8.2: Phase #2. EDS spectra of the lightest phase of the mineral on the BEI

8.2. Appendix 8.2

EDS spectra of the different phases in TB-CN2 sample observed in the BEI. All the peaks are labeled on the figures and the results of the standardless analyses are shown on the bottom of each spectrum.

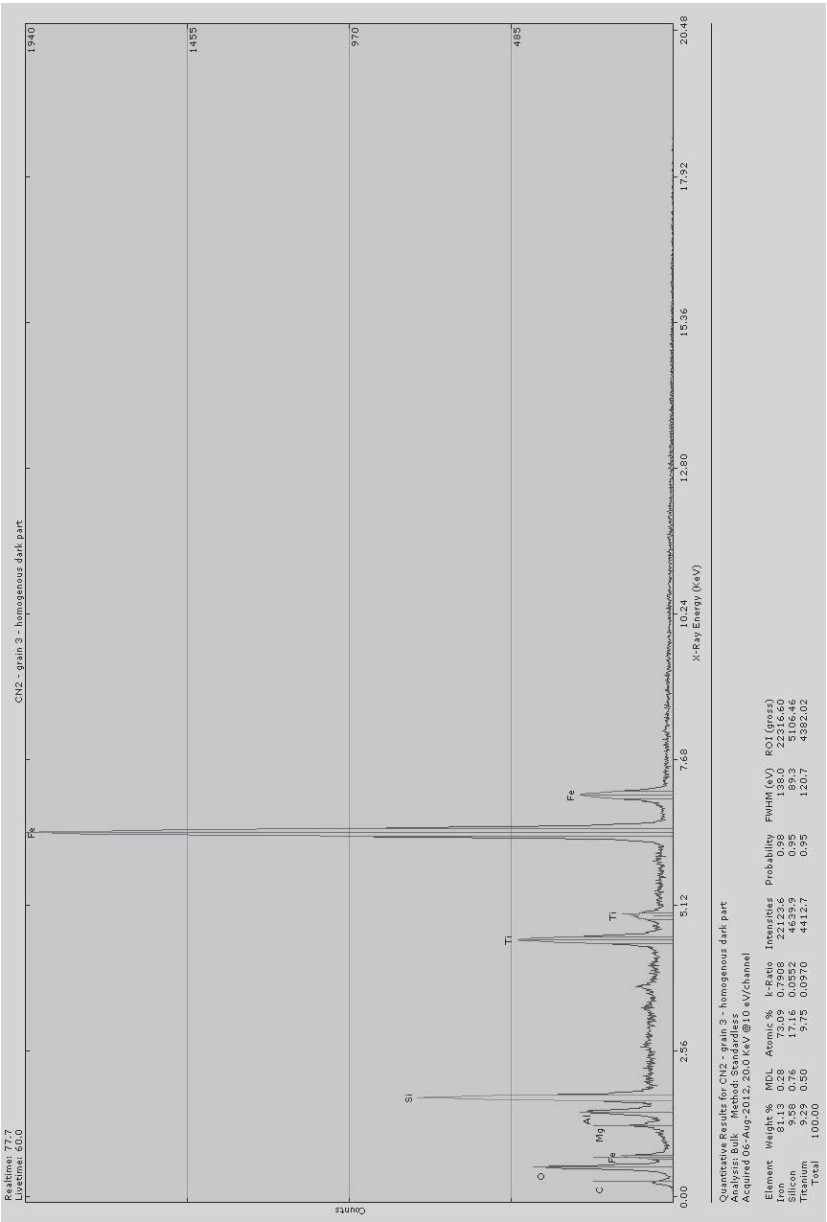


Figure 8.3: Phase #1. EDS spectra of the homogeneous dark phase of the mineral on the BEI

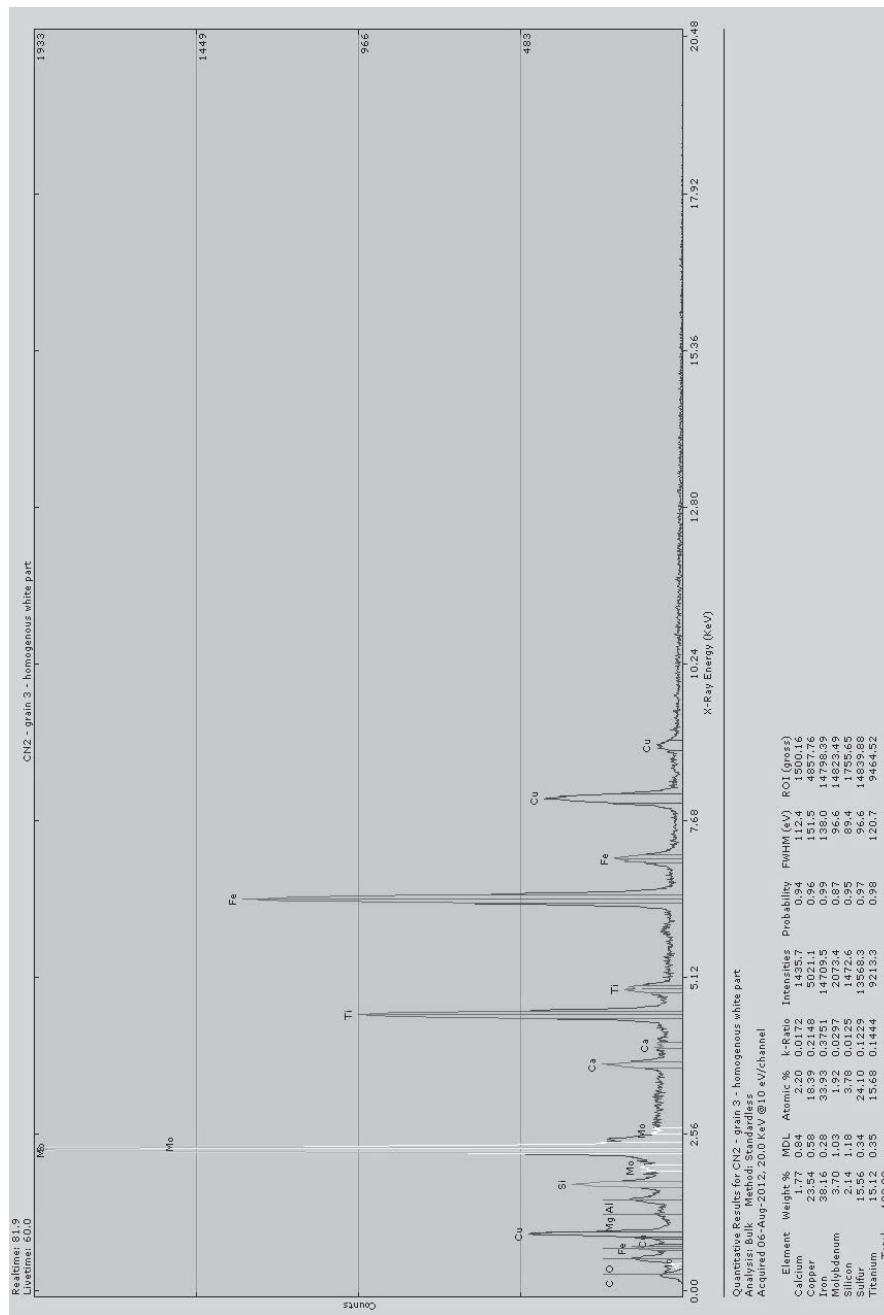


Figure 8.4: Phase #2. EDS spectra of the homogeneous and lightest phase of the mineral on the BEI

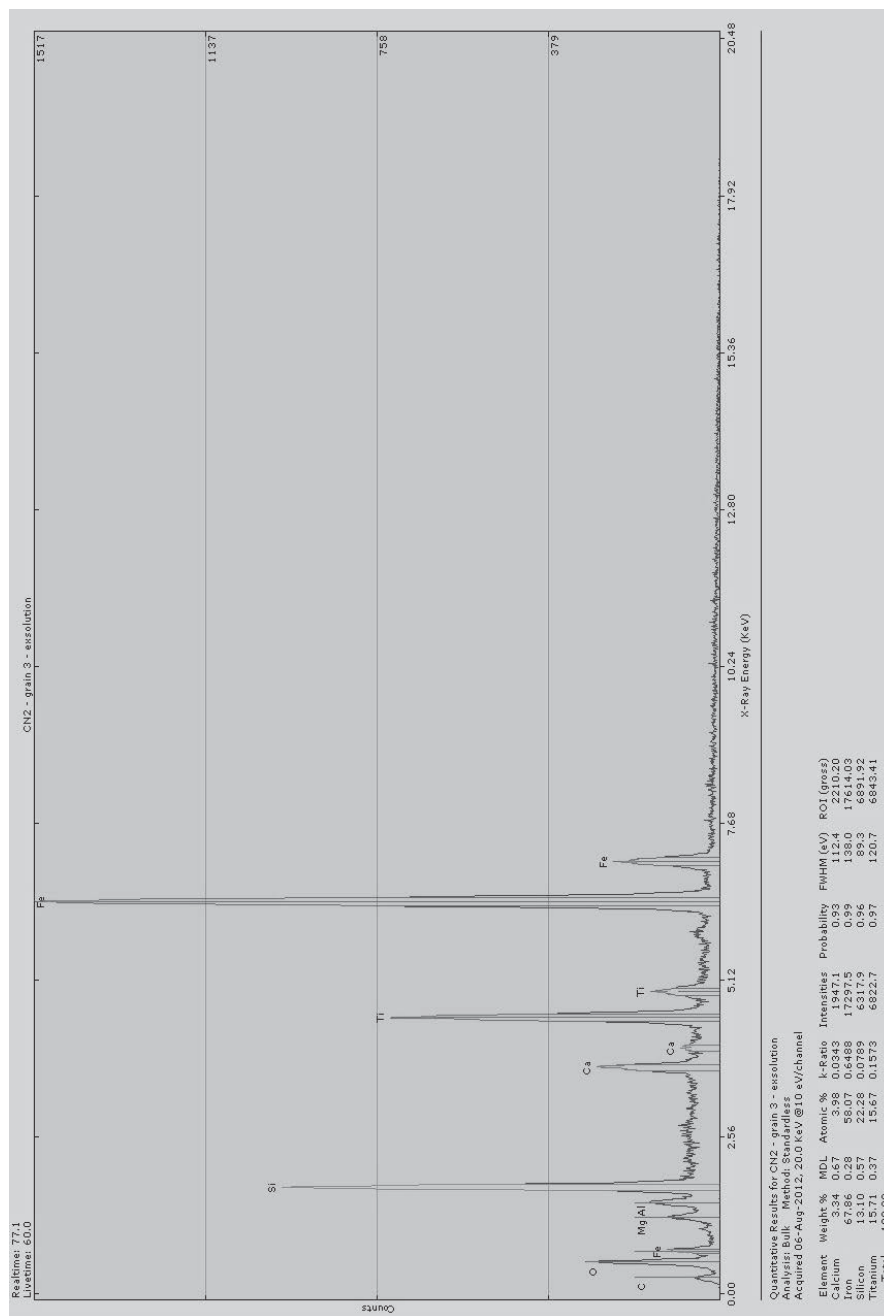


Figure 8.5: Phase #3. EDS spectra of the dark exsolution in the mineral on the BEI

8.3. Appendix 8.3:

EDS spectra of the different phases in TB-CN3 sample observed in the BEI. All the peaks are labeled on the figures and the results of the standardless analyses are shown on the bottom of each spectrum.

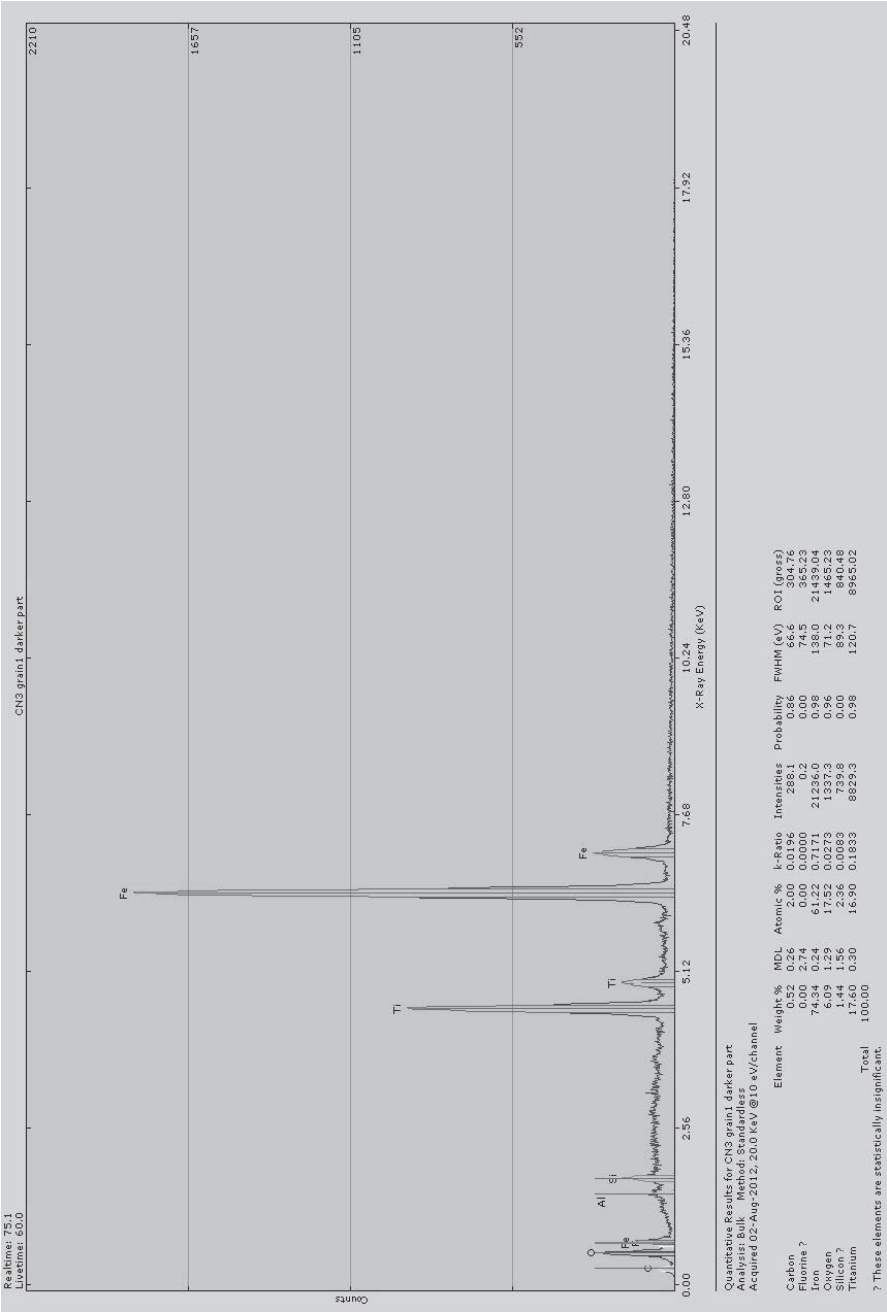


Figure 8.6: Phase #1. EDS spectra of the darkest phase of the mineral on the BEI

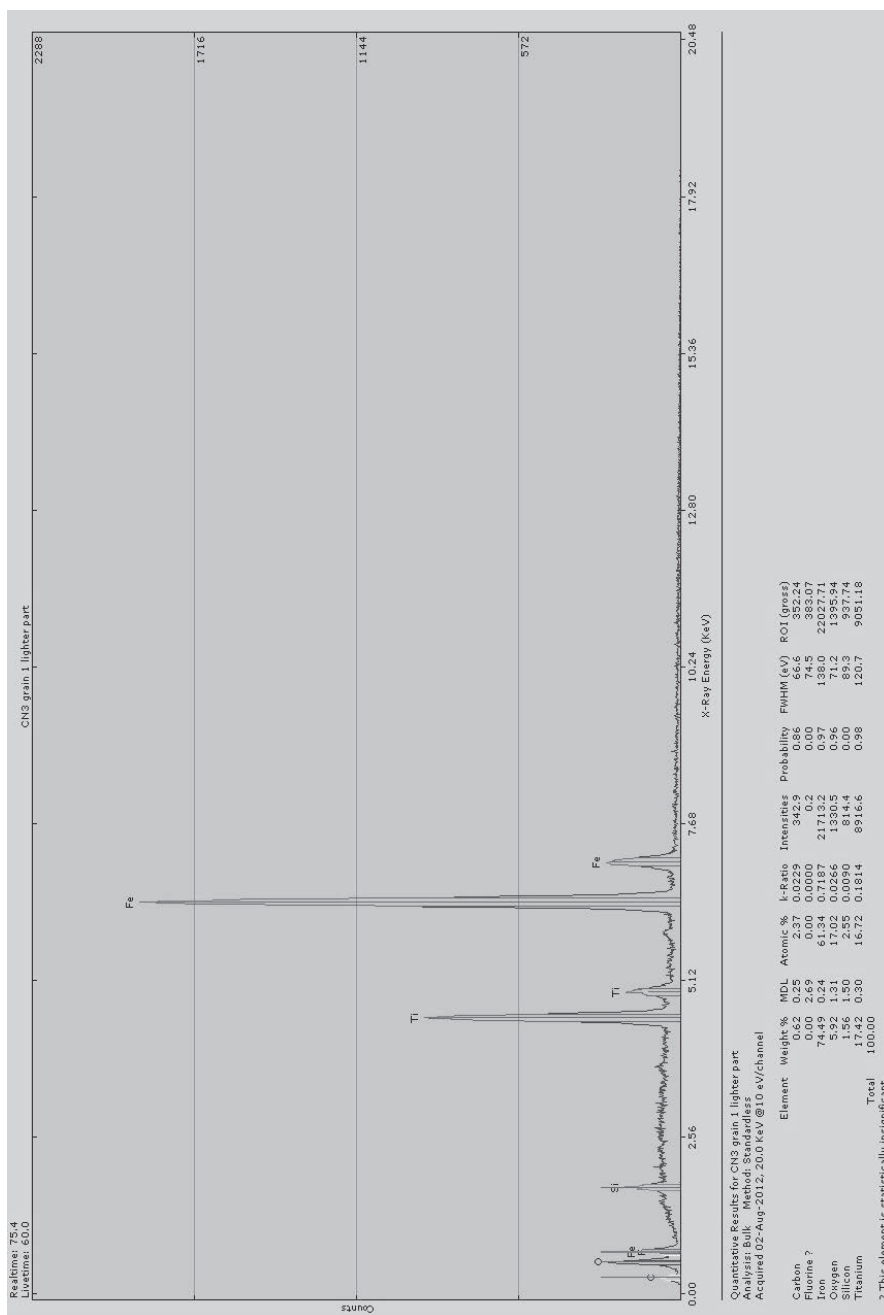


Figure 8.7: Phase #2. EDS spectra of the lightest phase of the mineral on the BEI

8.4. Appendix 8.4:

EDS spectra of the different phases in TB-CN3 sample observed in the BEI. All the peaks are labeled on the figures and the results of the standardless analyses are shown on the bottom of each spectrum.

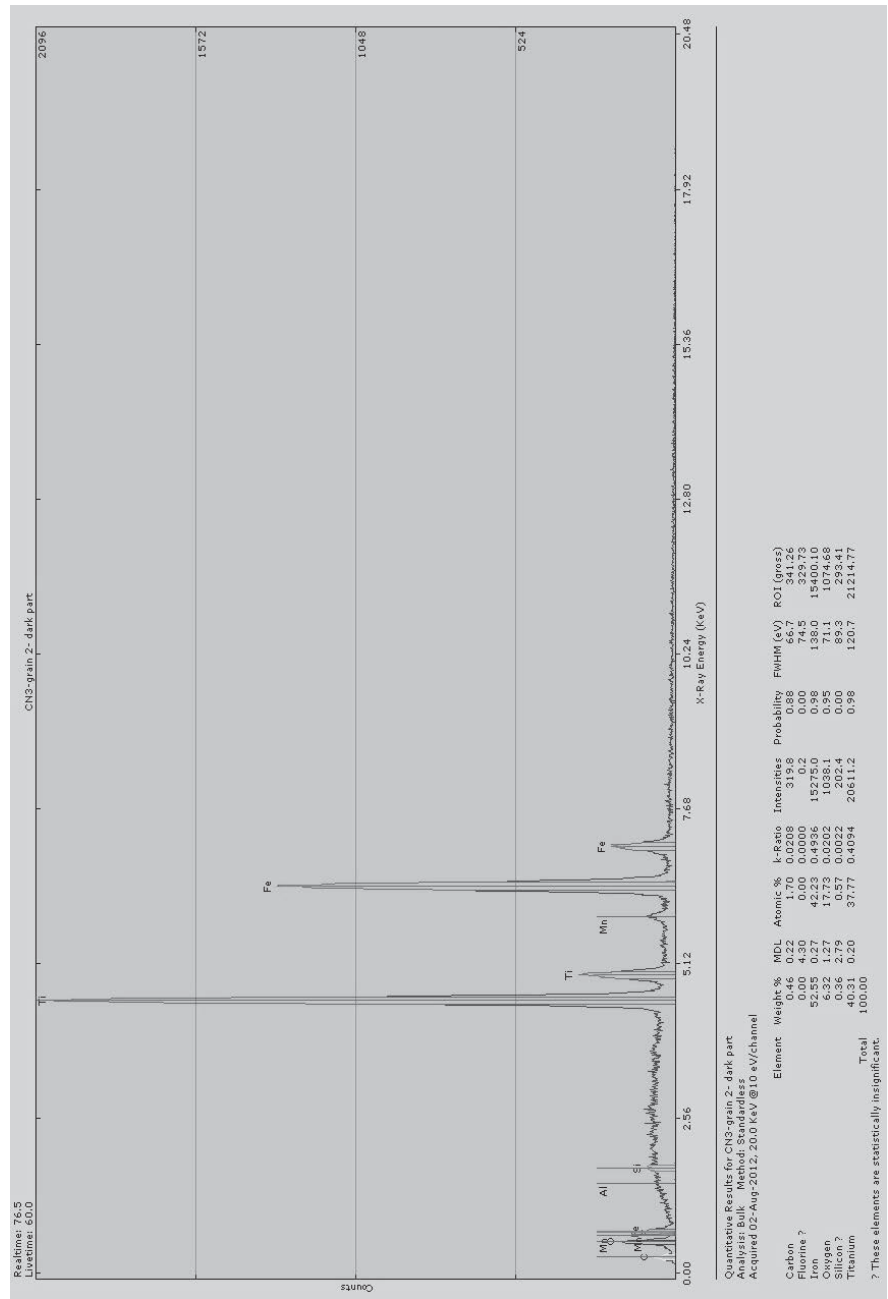


Figure 8.8: Phase #1. EDS spectra of the darkest phase of the mineral on the BEI

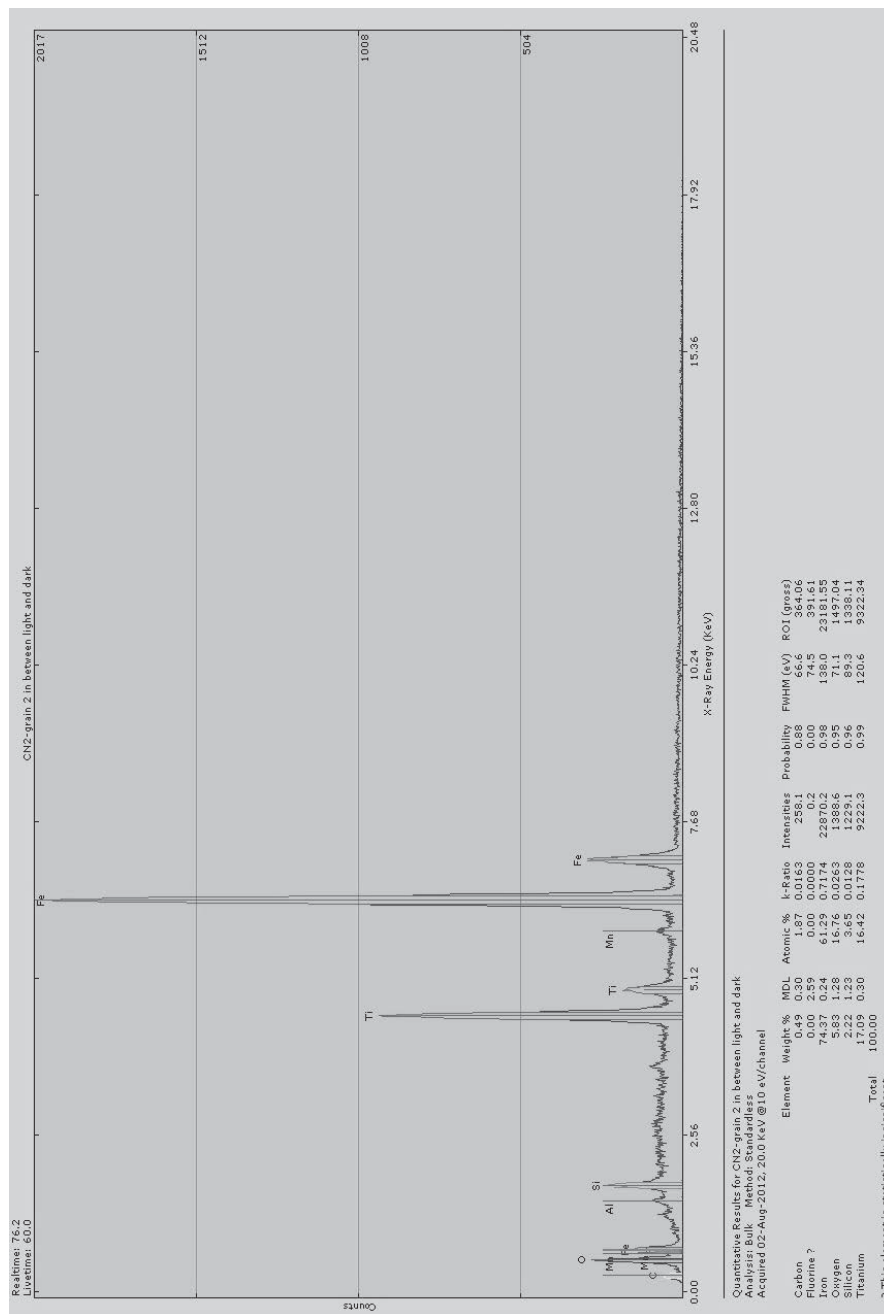


Figure 8.9: Phase #2. EDS spectra of the medium phase of the mineral on the BEI

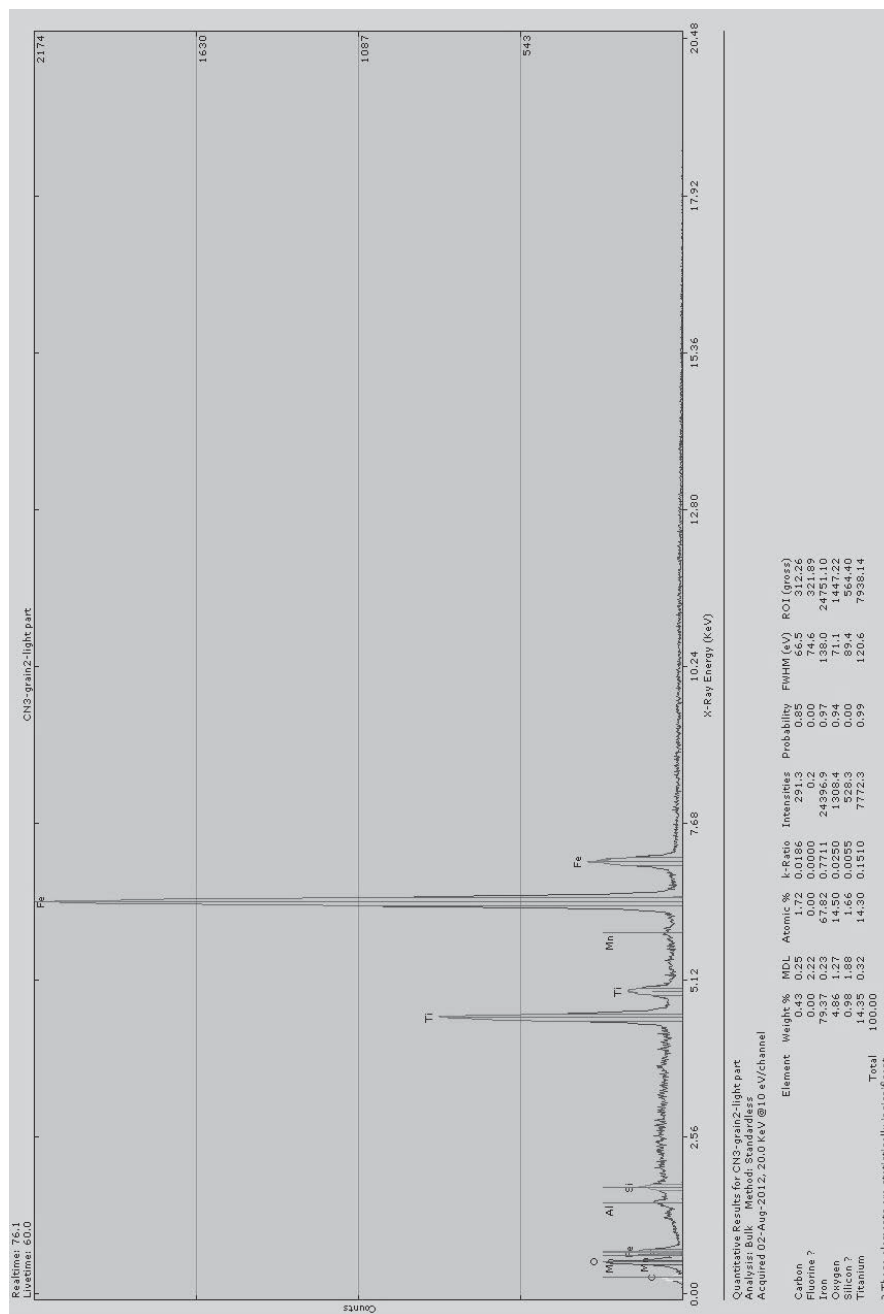


Figure 8.10: Phase #3. EDS spectra of the lightest phase of the mineral on the BEI

8.5. Appendix 8.5:

EDS spectra of the different phases in TB-CN5 sample observed in the BEI. All the peaks are labeled on the figures and the results of the standardless analyses are shown on the bottom of each spectrum.

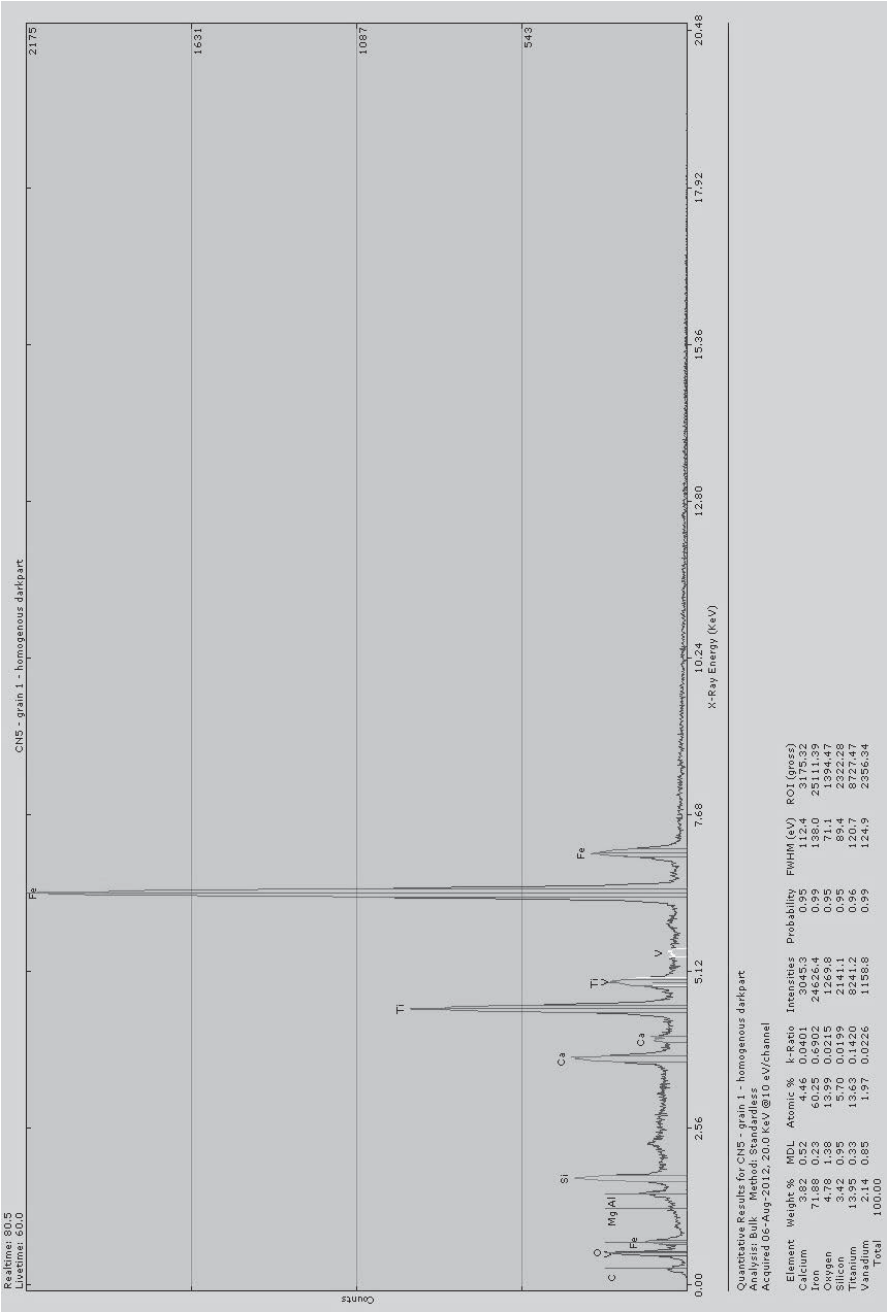


Figure 8.11: Phase #1. EDS spectra of the darkest phase of the mineral on the BEI

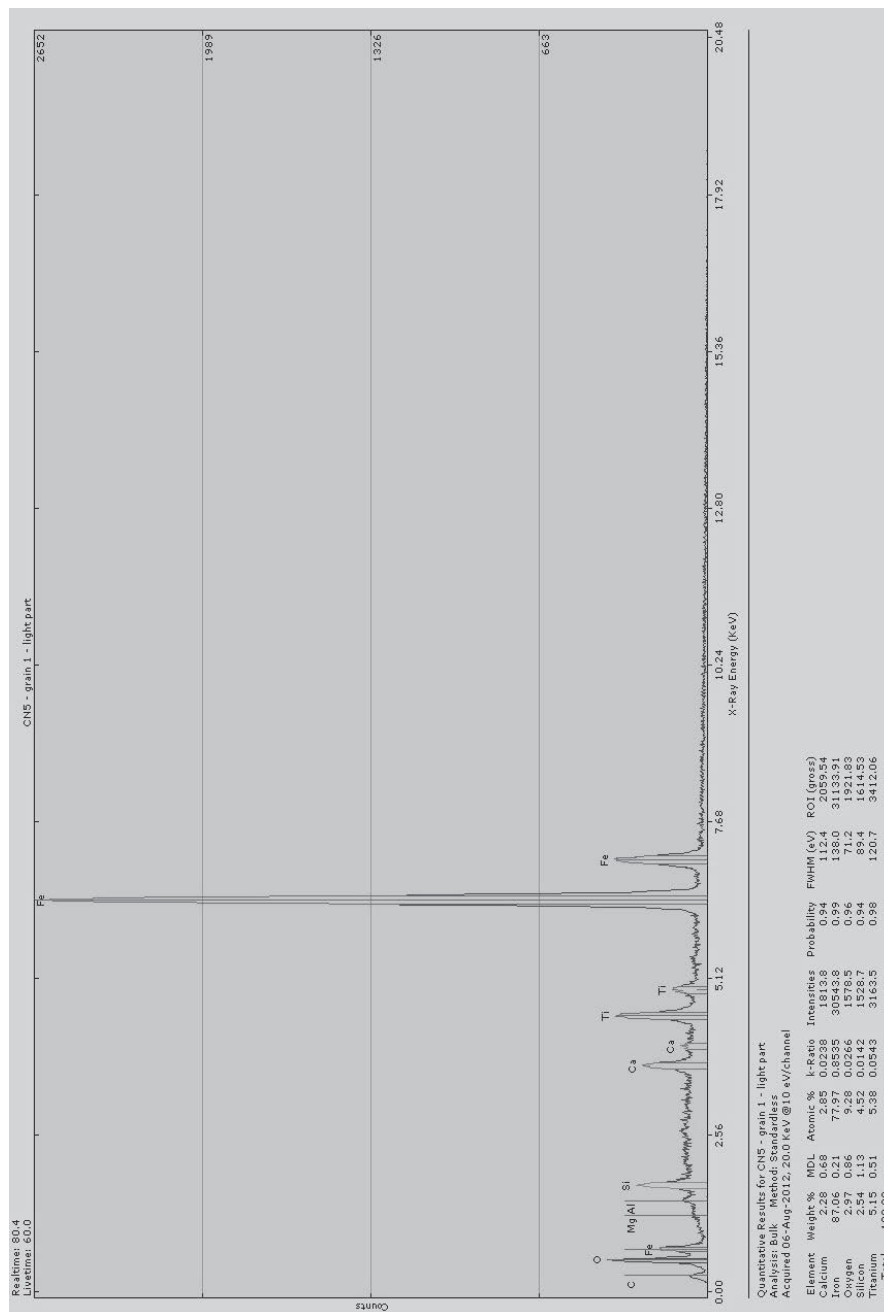


Figure 8.12: Phase #2. EDS spectra of the lightest phase of the mineral on the BEI

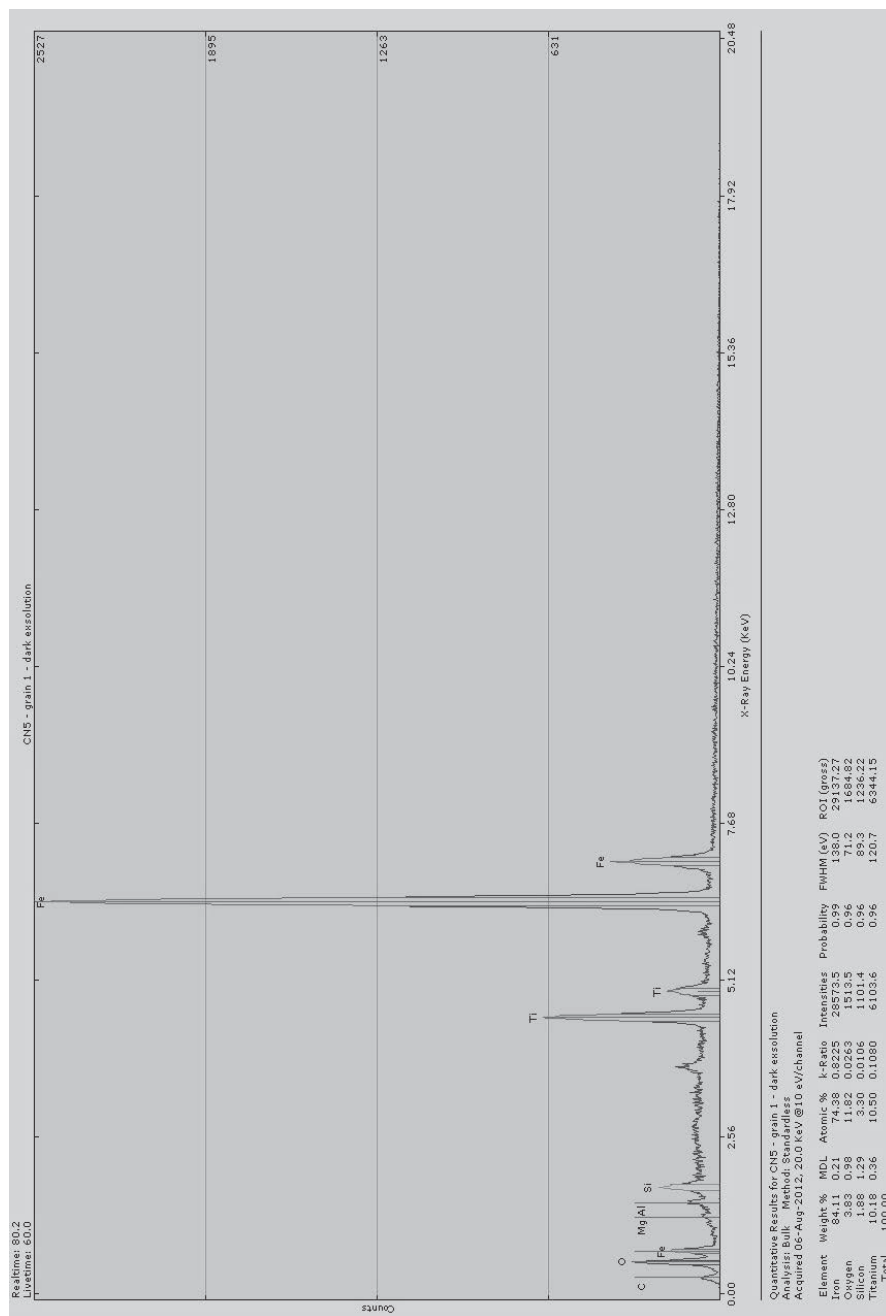


Figure 8.13: Phase #3. EDS spectra of the exsolutions in the mineral on the BEI

8.6. Appendix 8.6:

EDS spectra of the different phases in NM-CM3A sample observed in the BEI. All the peaks are labeled on the figures and the results of the standardless analyses are shown on the bottom of each spectrum.

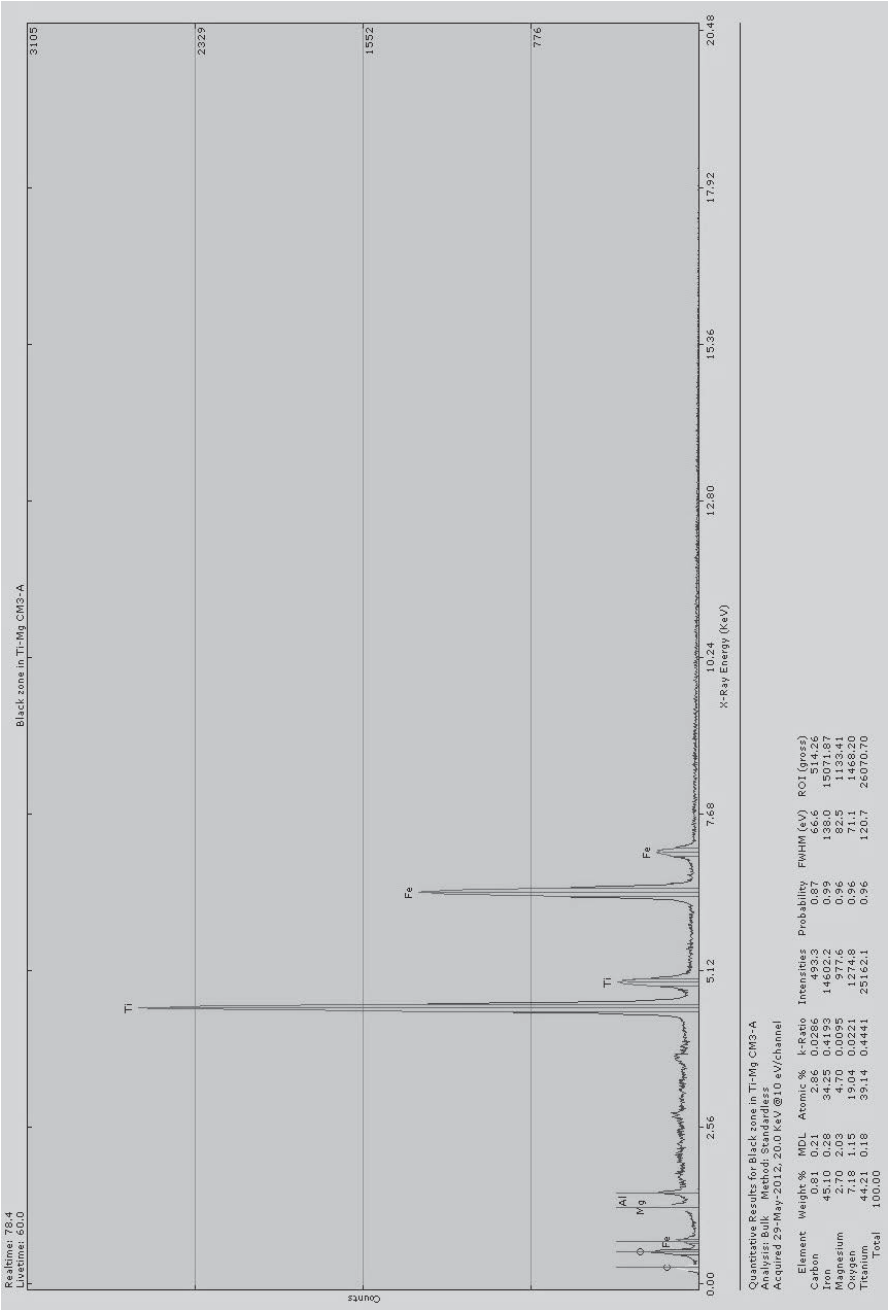


Figure 8.14: Phase #1. EDS spectra of the darkest phase of the mineral on the BEI

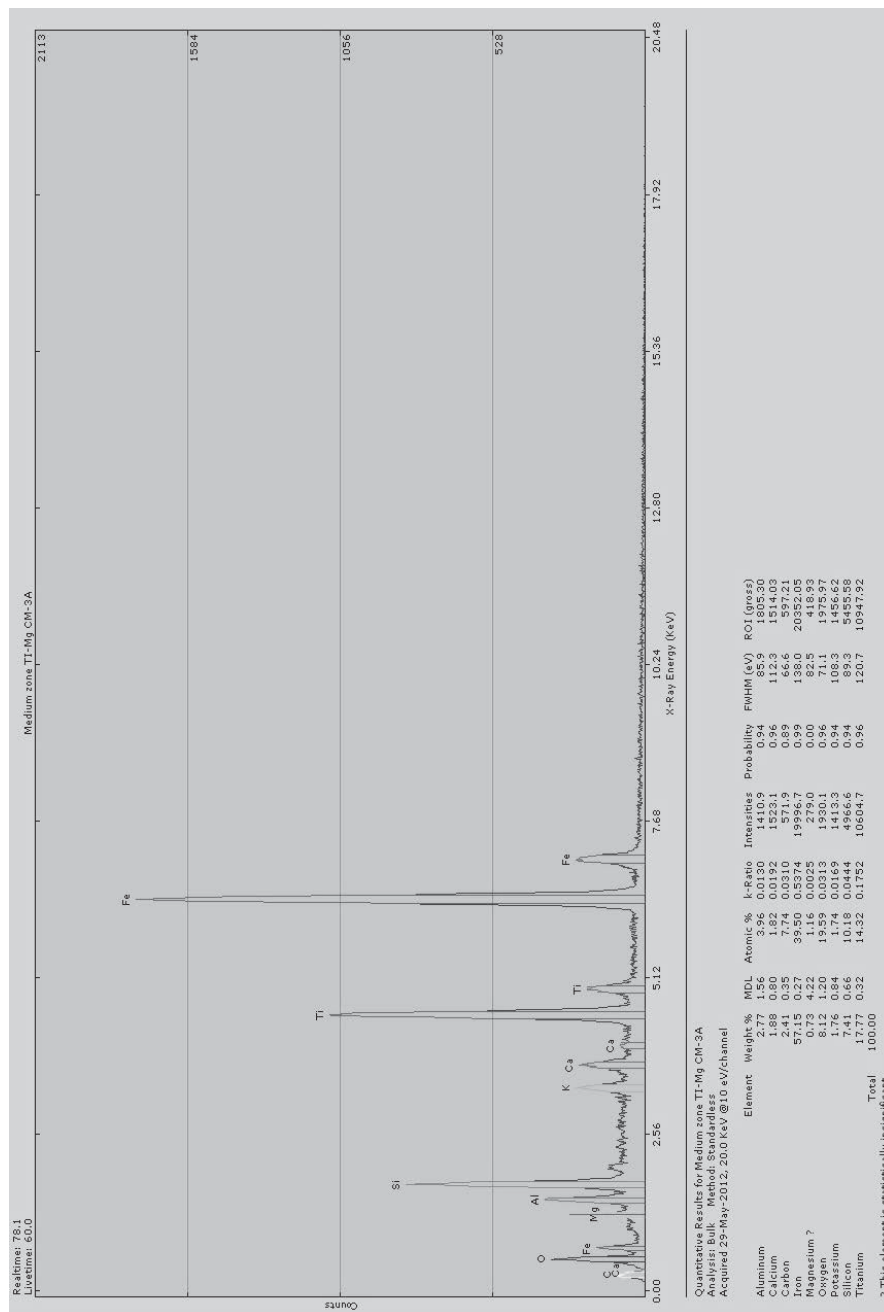


Figure 8.15: Phase #2. EDS spectra of the medium gray phase of the mineral on the BEI

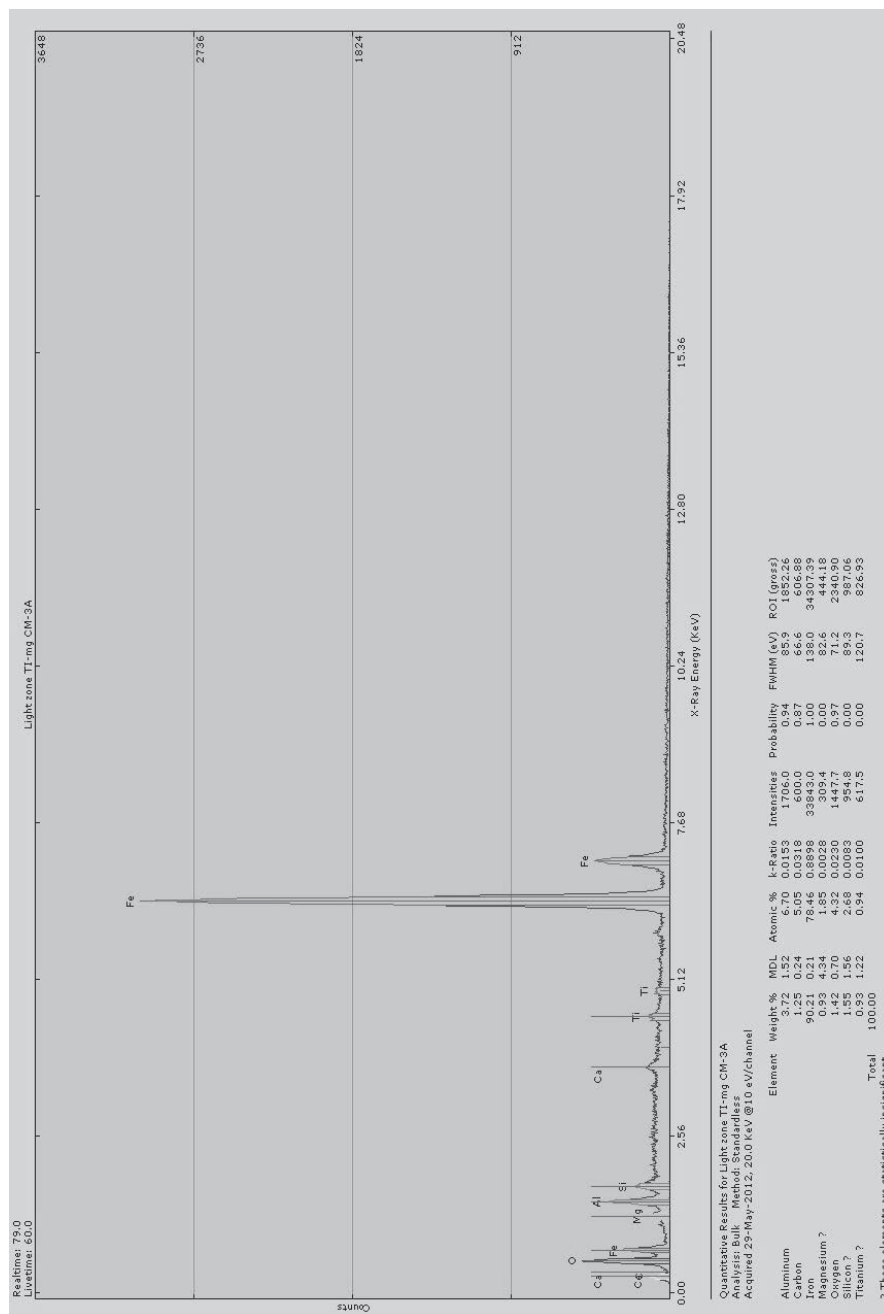


Figure 8.16: Phase #3. EDS spectra of the lightest phase of the mineral on the BEI

8.7. Appendix 8.7:

EDS spectra of the different phases in NM-CMB1 sample observed in the BEI. All the peaks are labeled on the figures and the results of the standardless analyses are shown on the bottom of each spectrum.

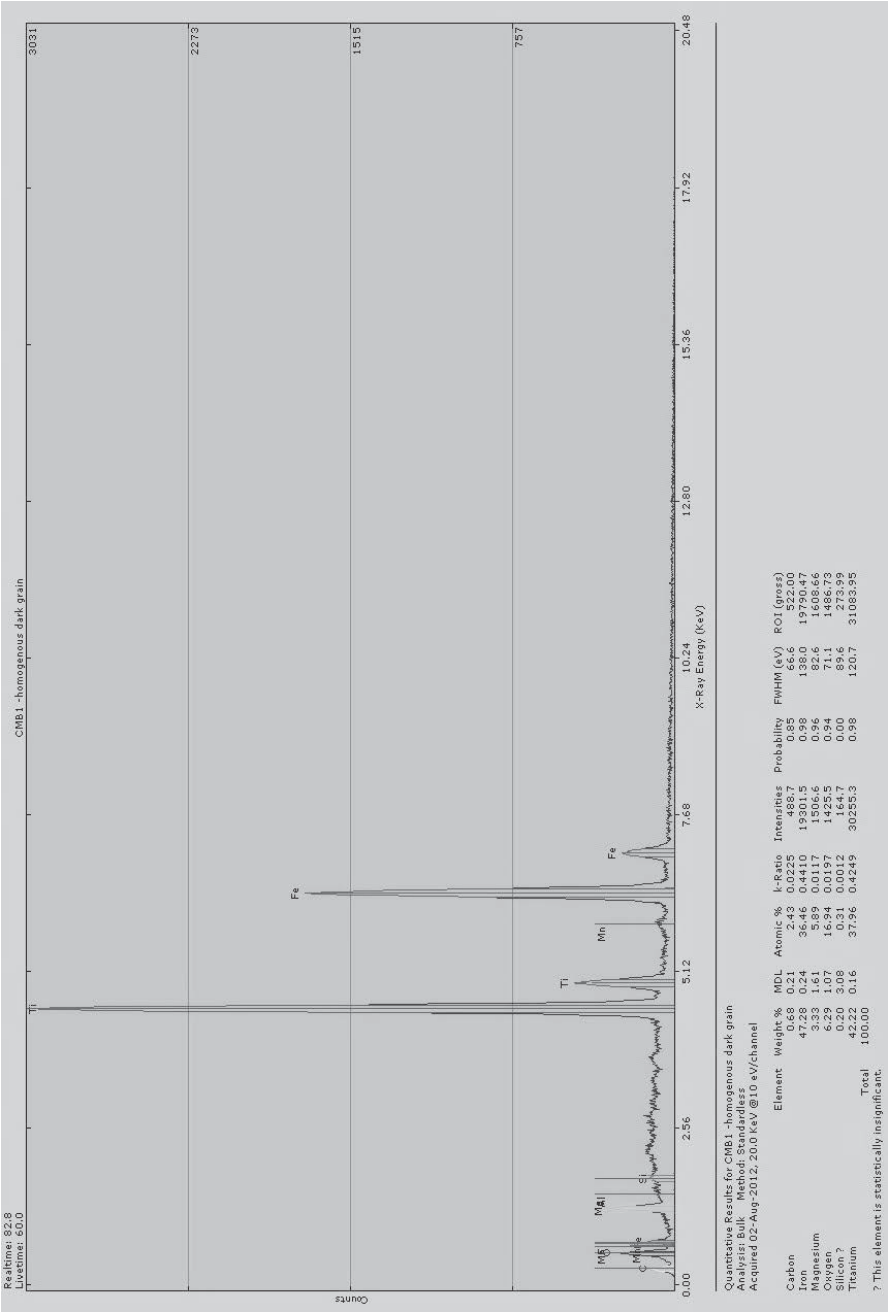


Figure 8.17: Phase #1. EDS spectra of the darkest mineral on the BEI

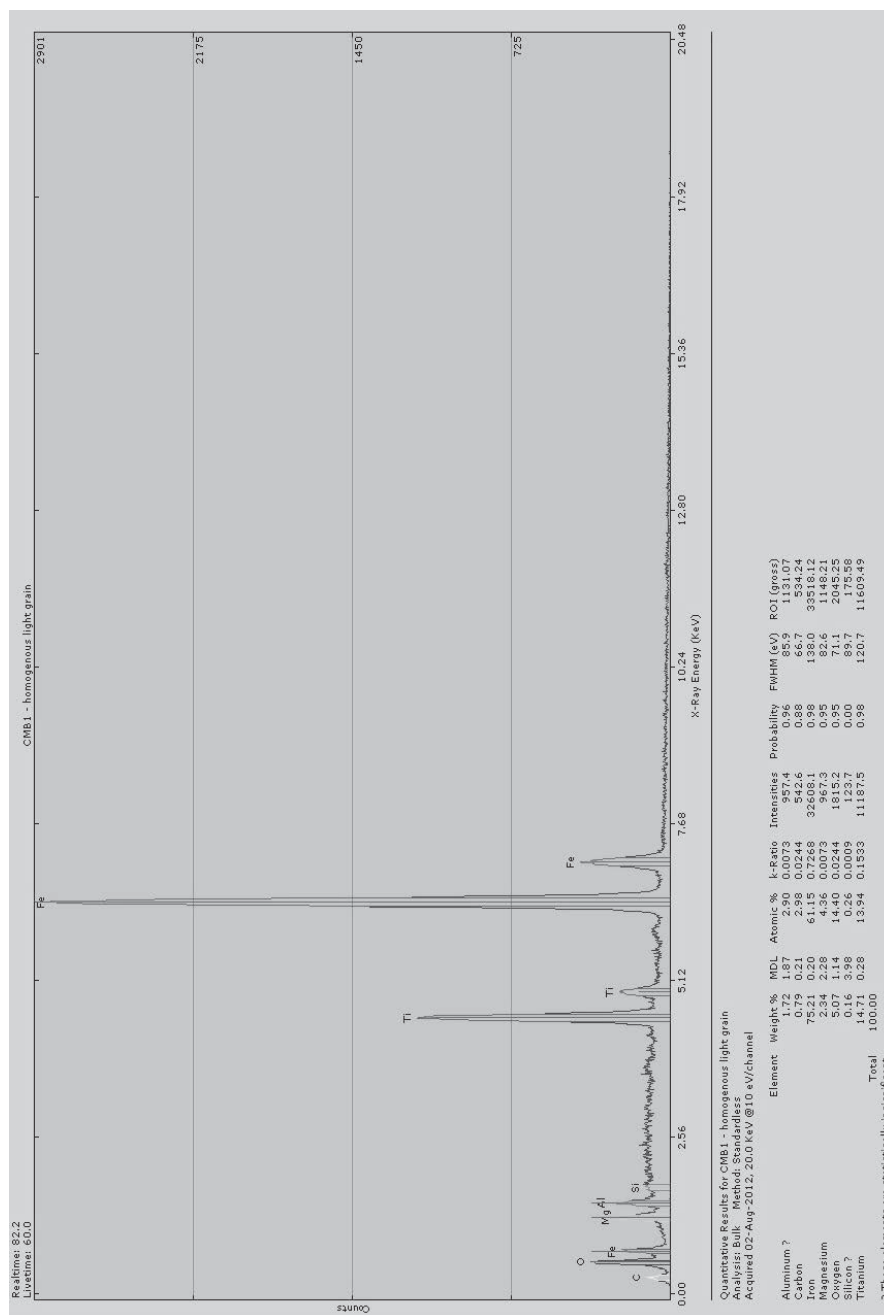


Figure 8.18: Phase #2. EDS spectra of the lightest mineral on the BEI

8.8. Appendix 8.8:

EDS spectra of the different phases in NM-CMB1 sample observed in the BEI. All the peaks are labeled on the figures and the results of the standardless analyses are shown on the bottom of each spectrum.

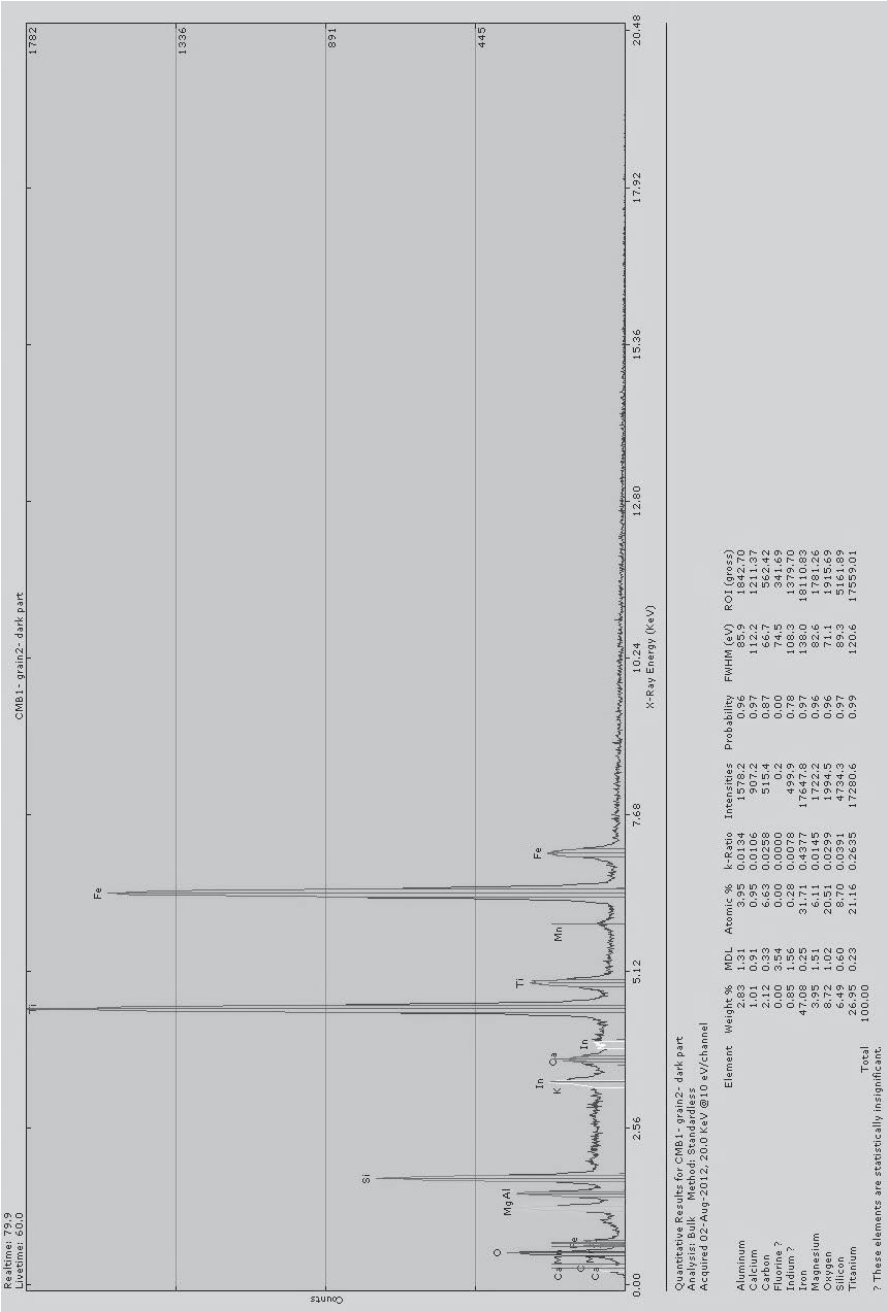


Figure 8.19: Phase #1. EDS spectra of the darkest phase of the mineral on the BEI

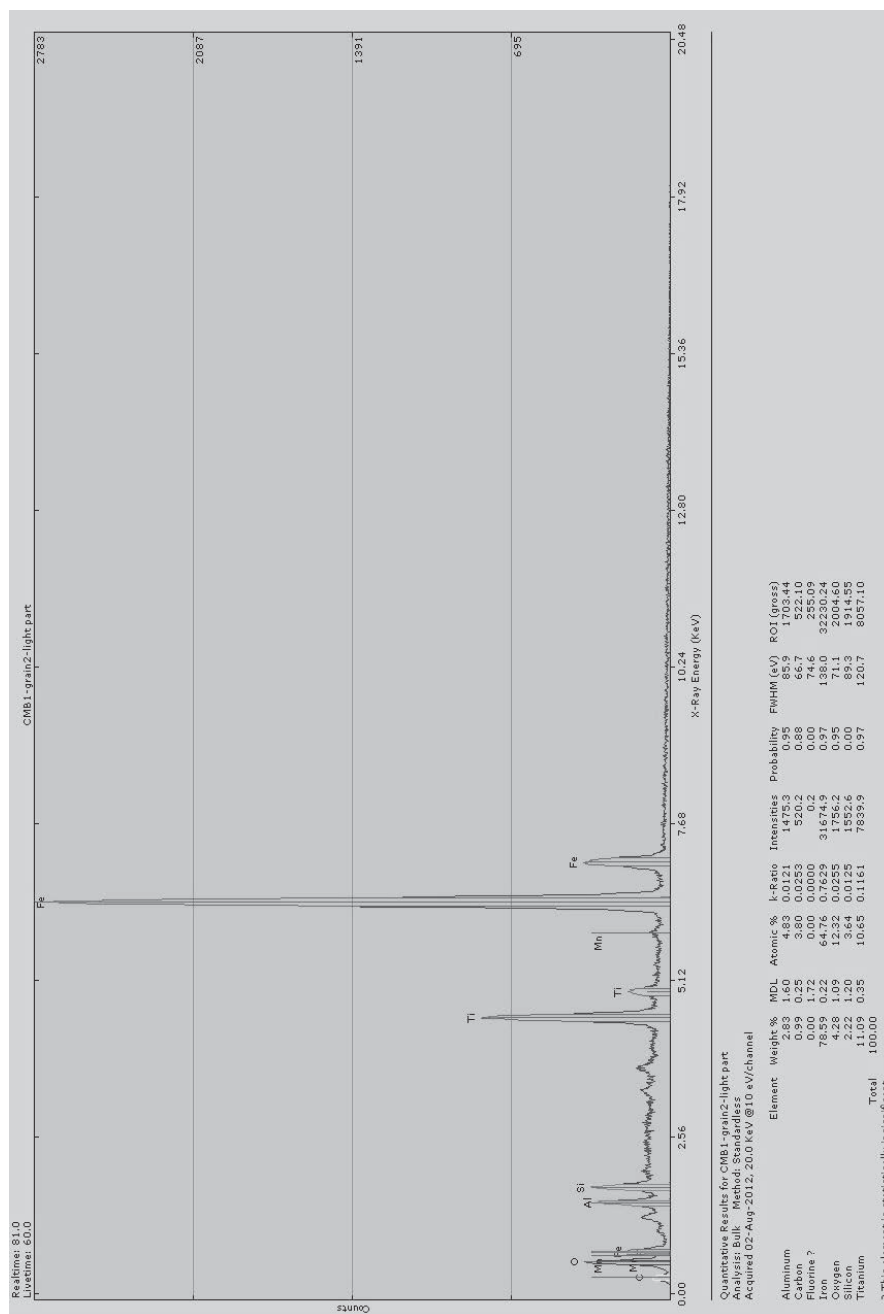


Figure 8.20: Phase #2. EDS spectra of the lightest phase of the mineral on the BEI

8.9. Appendix 8.9:

EDS spectra of the different phases in NM-CMB1 sample observed in the BEI. All the peaks are labeled on the figures and the results of the standardless analyses are shown on the bottom of each spectrum.

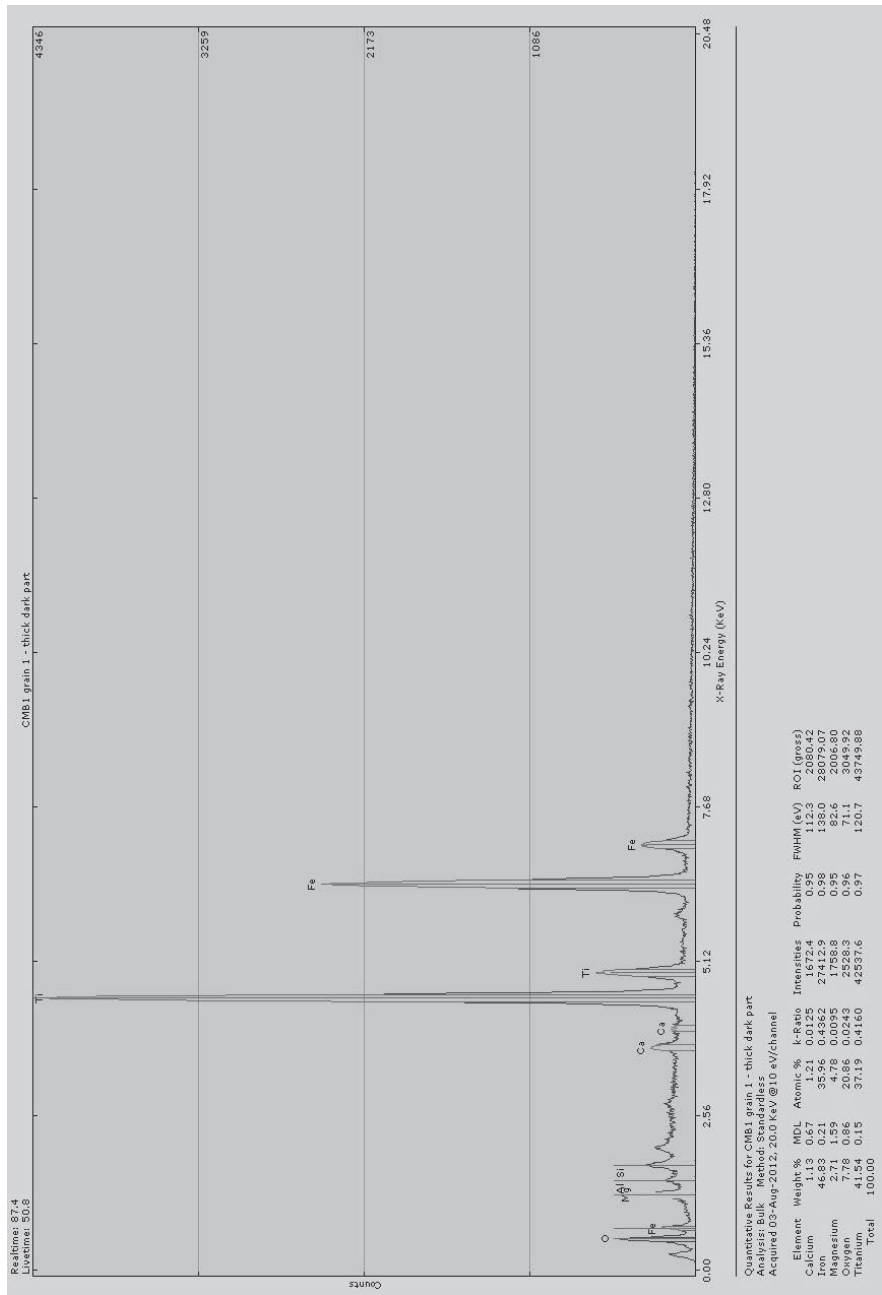


Figure 8.21: Phase #1. EDS spectra of the dark and large exsolution of the mineral on the BEI

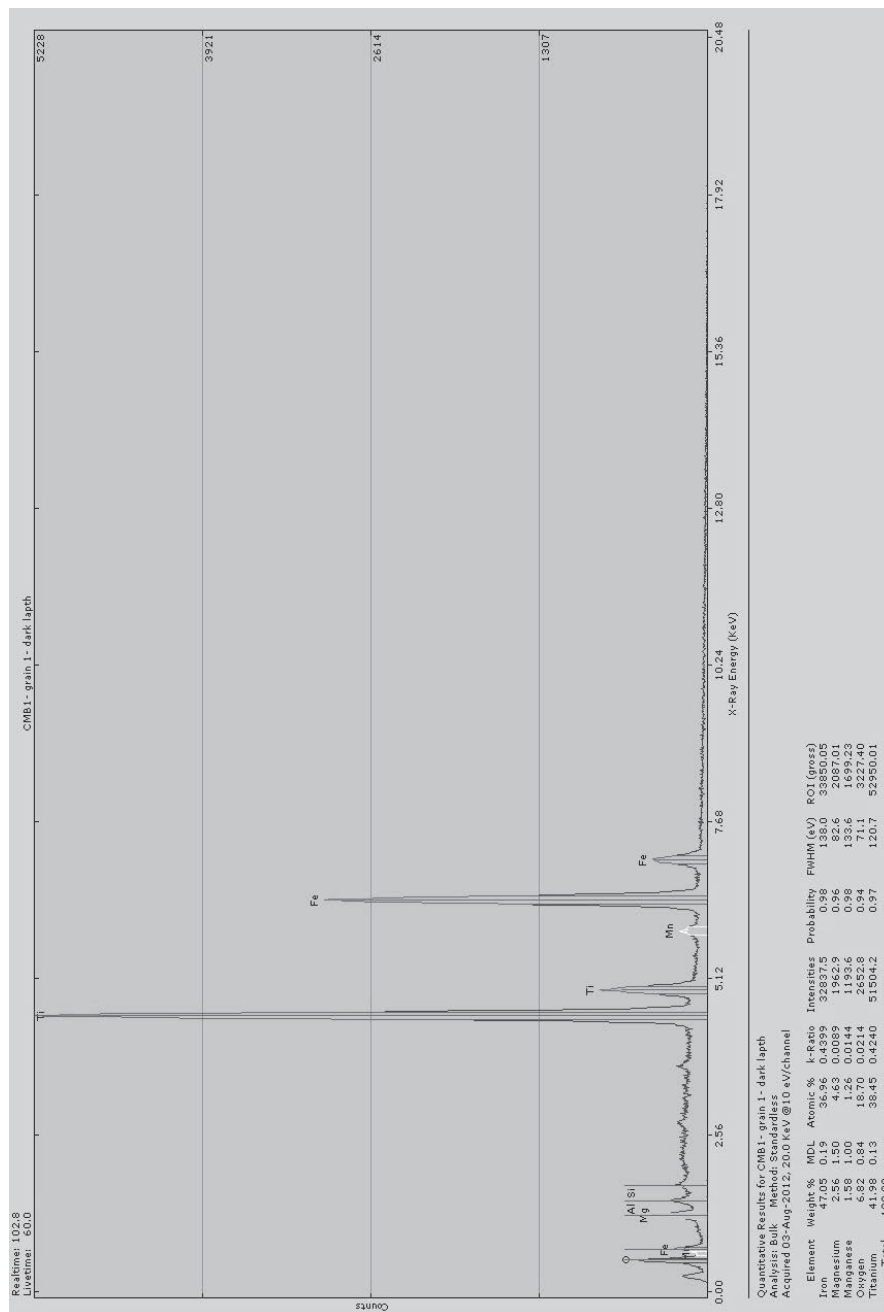


Figure 8.22: Phase #2. EDS spectra of the dark and thin exsolution phase of the mineral on the BEI

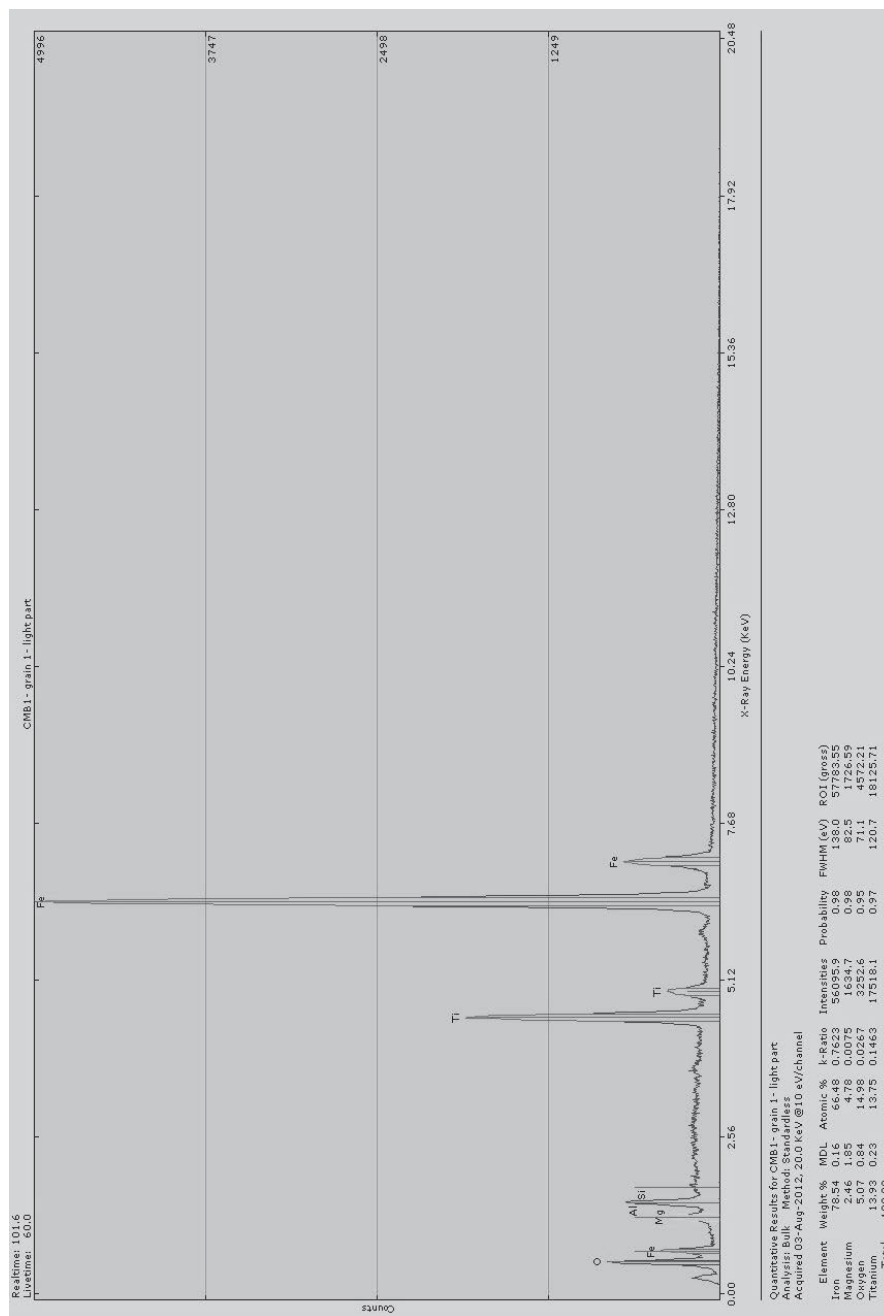


Figure 8.23: Phase #3. EDS spectra of the lightest phase of the mineral on the BEI

8.10.Appendix 8.10:

EDS spectra of the different phases in NM-CMB2 sample observed in the BEI. All the peaks are labeled on the figures and the results of the standardless analyses are shown on the bottom of each spectrum.

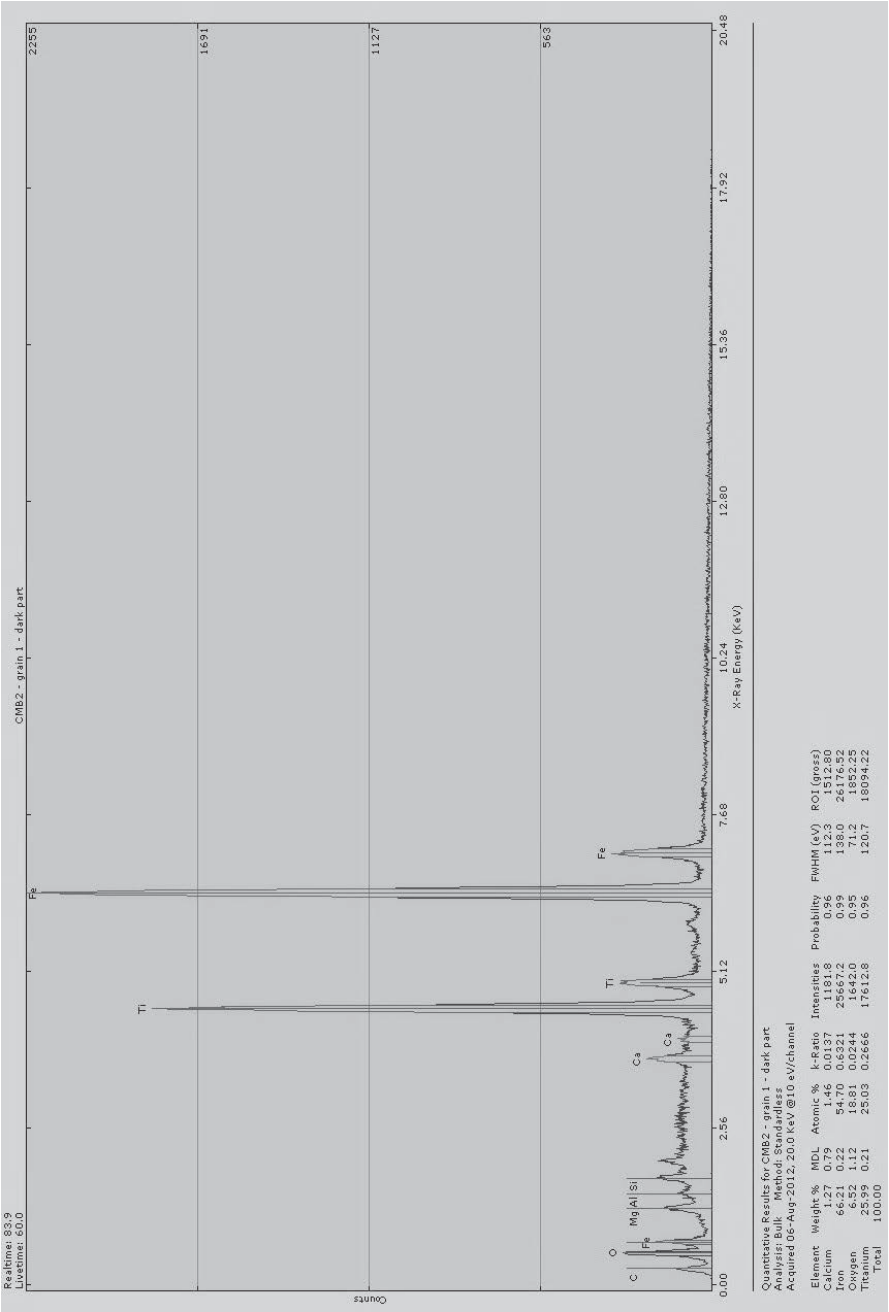


Figure 8.24: Phase #1. EDS spectra of the darkest phase of the mineral on the BEI

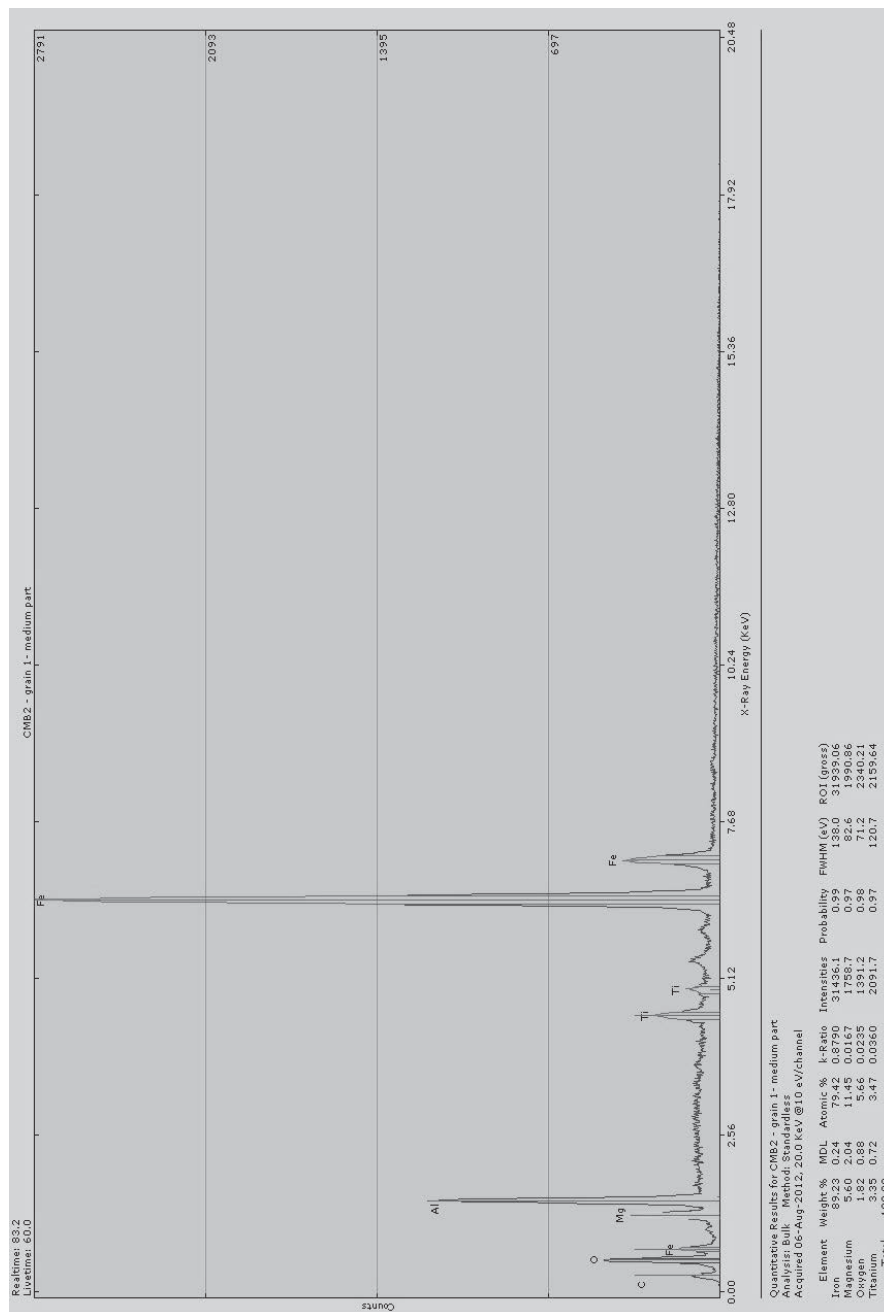


Figure 8.25: Phase #2. EDS spectra of the medium phase of the mineral on the BEI

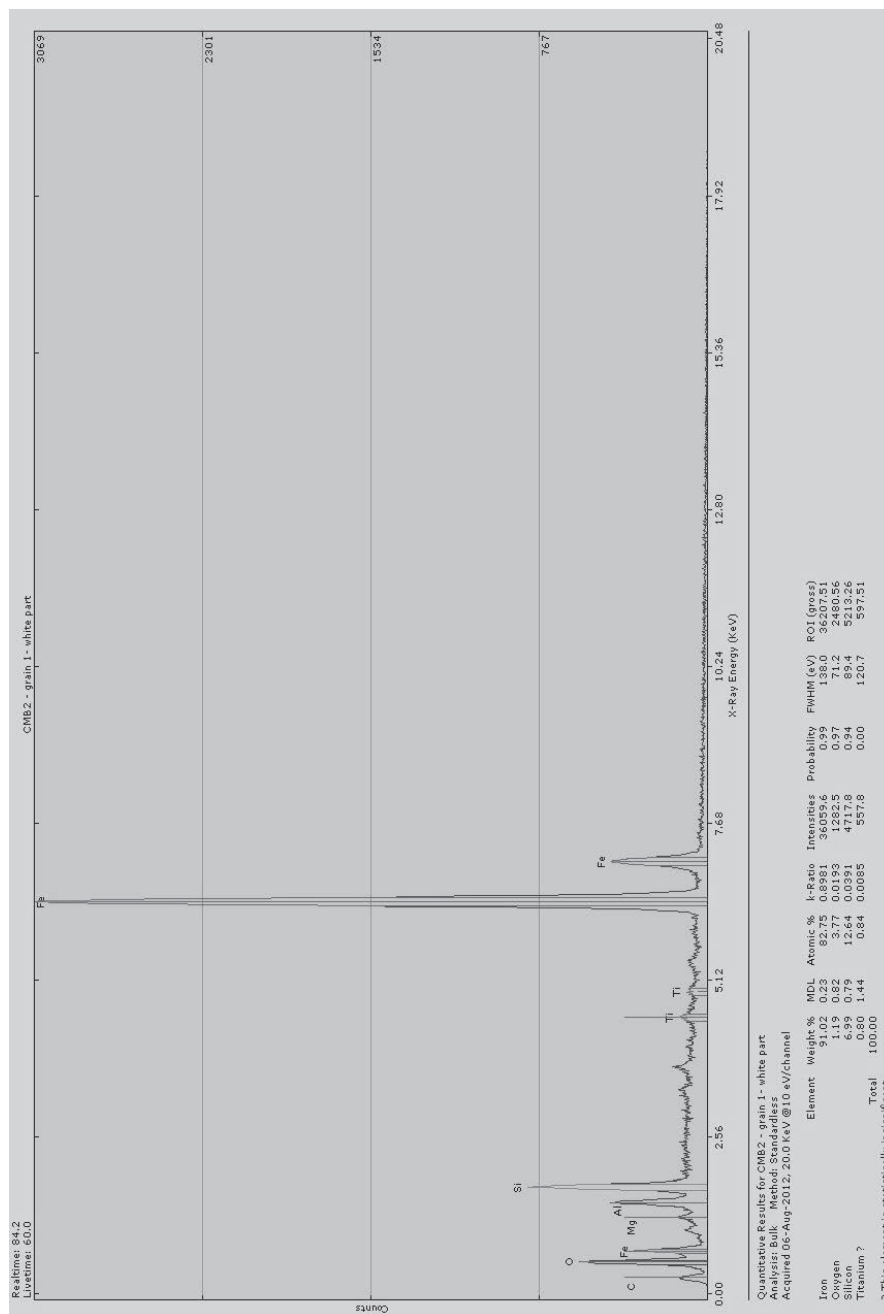


Figure 8.26: Phase #3. EDS spectra of the fractured and lightest phase of the mineral on the BEI

8.11.Appendix 8.11:

EDS spectra of the different phases in NM-CMB2 sample observed in the BEI. All the peaks are labeled on the figures and the results of the standardless analyses are shown on the bottom of each spectrum.

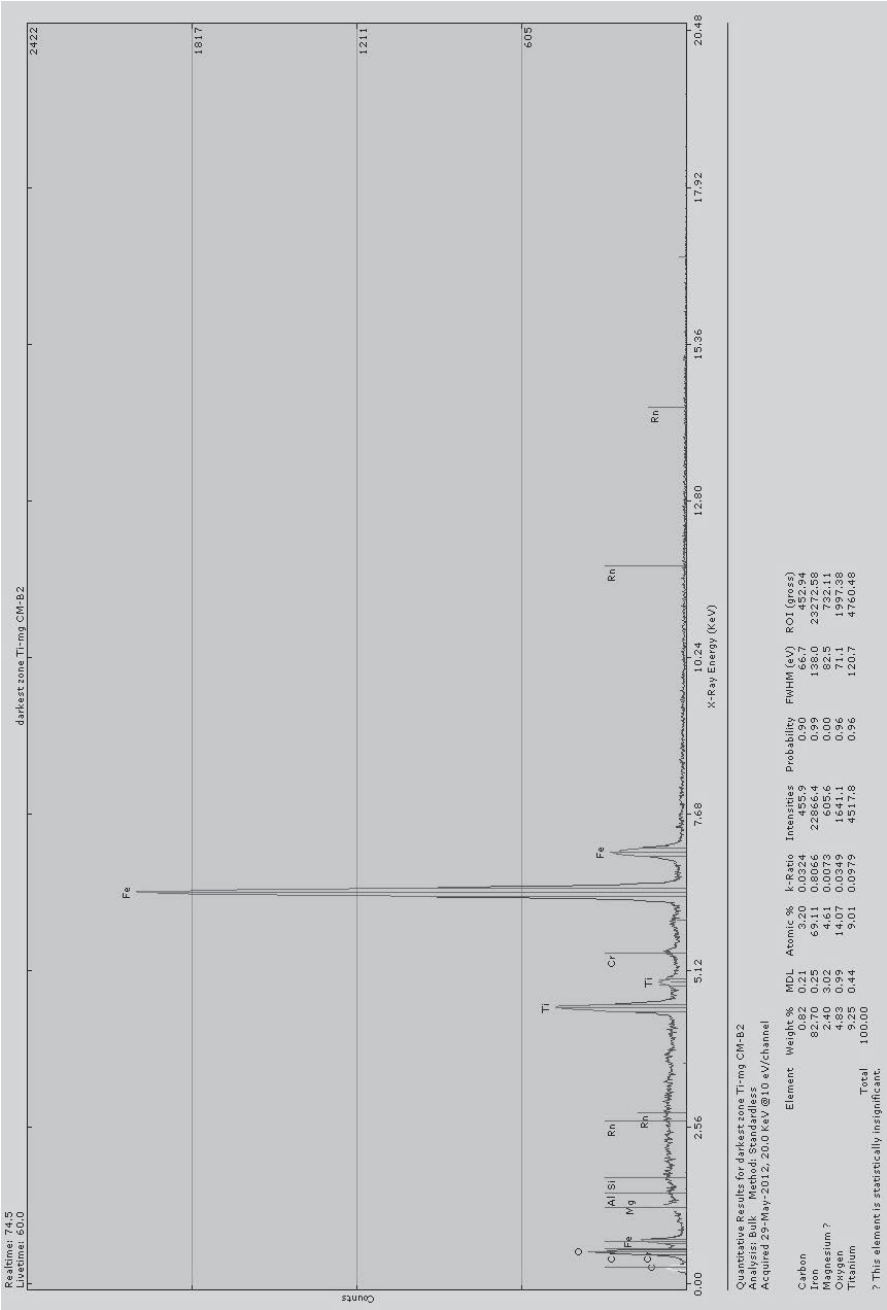


Figure 8.27: Phase #1. EDS spectra of the darkest phase of the mineral on the BEI

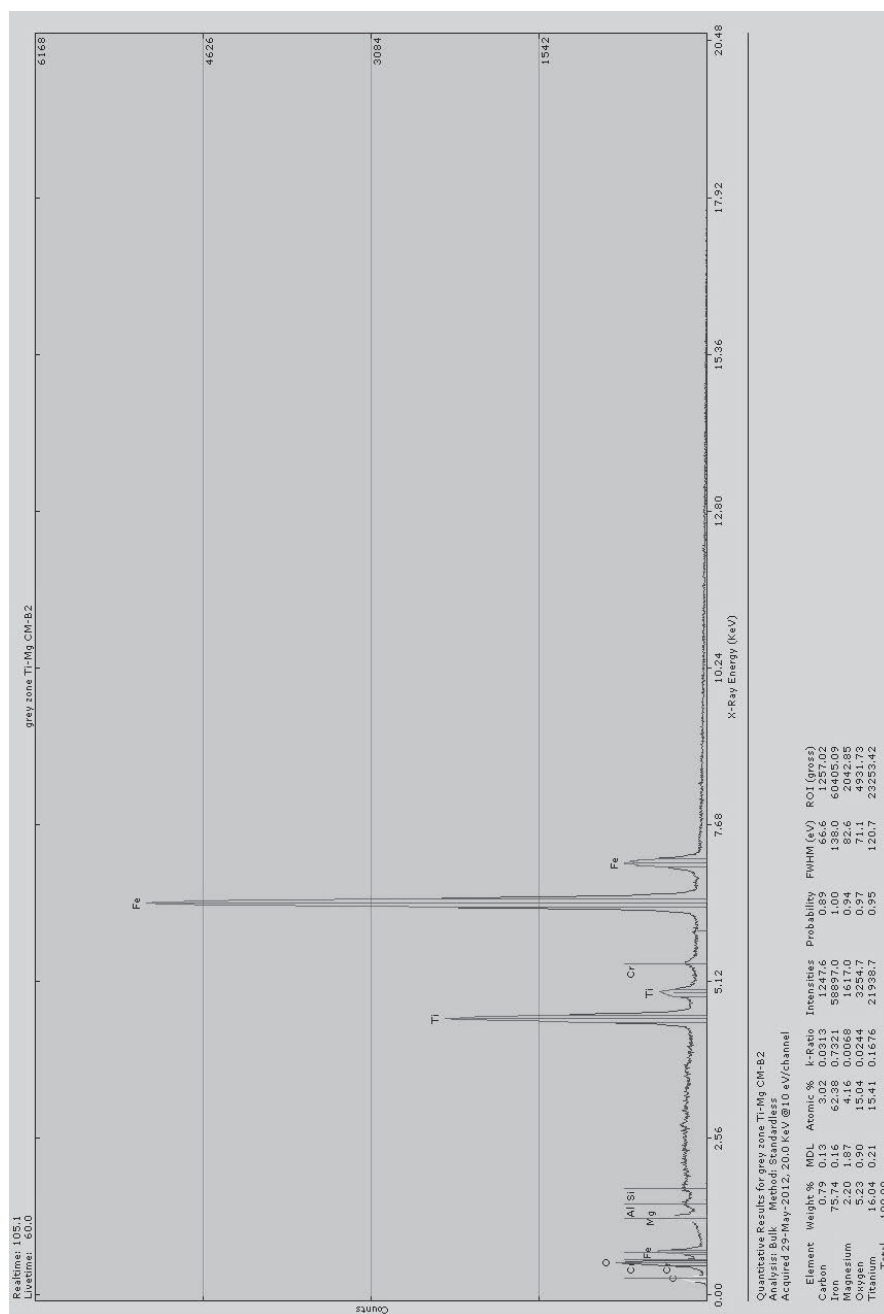


Figure 8.28: Phase #2. EDS spectra of the second darkest phase of the mineral on the BEI

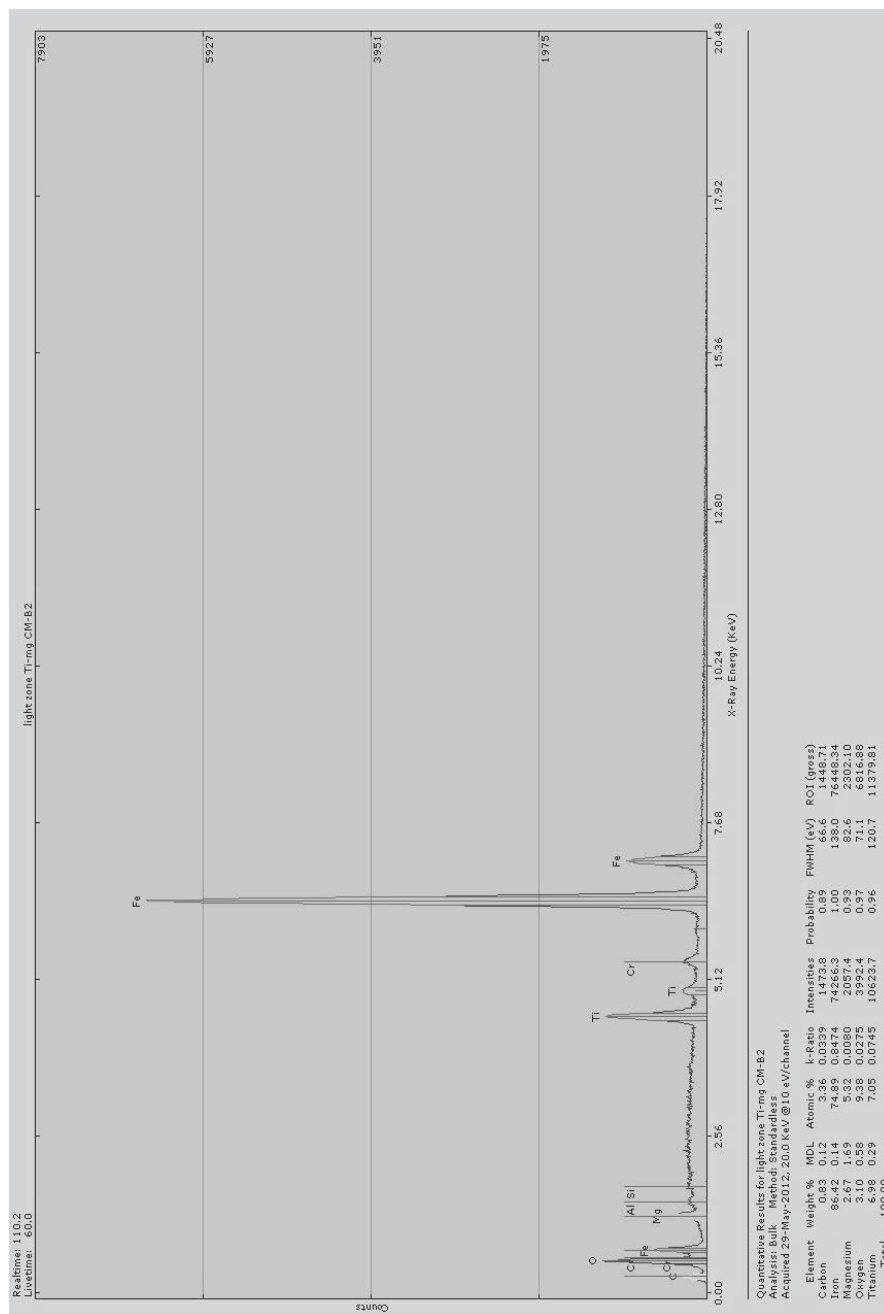


Figure 8.29: Phase #3. EDS spectra of the second lightest phase of the mineral on the BEI

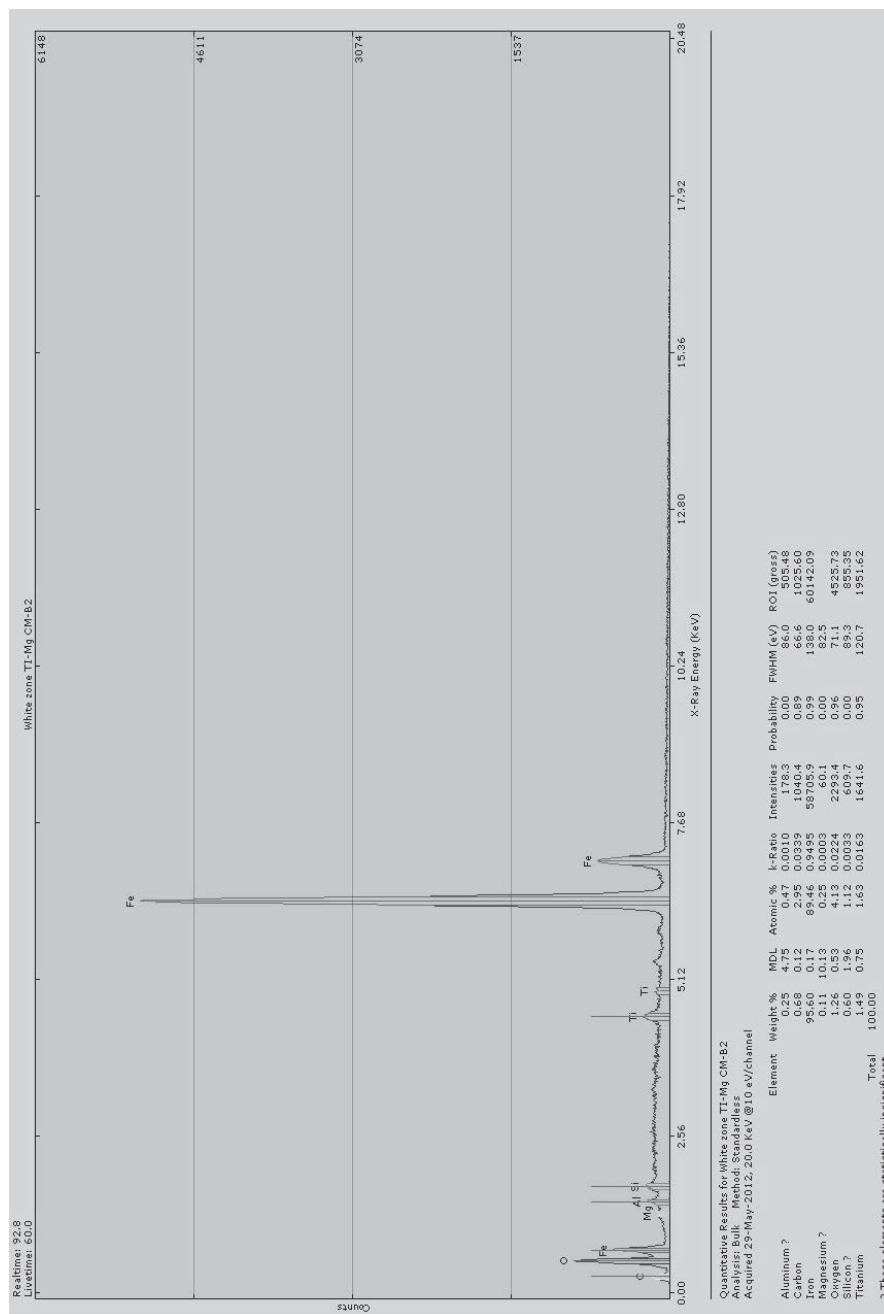


Figure 8.30: Phase #4. EDS spectra of the lightest phase of the mineral on the BEI

8.12.Appendix 8.12:

Copyright permissions

PERMISSION GRANTED FOR THE
USE REQUESTED ABOVE:

[Type name of company]

By: Elisa Piispa

Title: DEM of Thunder Bay area

Date: 08/10/12

Figure 8.31: Copyright permission for Figure 3.1: Digital Elevation Model (DEM) of the study area shows that some dykes can be traced based on the elevation in Thunder Bay area. The red circle shows the location of the dyke and lava flow. (By Piispa et al. (2011)

PERMISSION GRANTED FOR THE
USE REQUESTED ABOVE:

By: Marine Foucher

Title: Figure 9: Field photograph of the Cienega mine, view to south from the Cerro Grande.

Date: 08/12/2012

Figure 8.32: Copyright permission for Figure 3.3: Field photograph of the south of La Cienega volcano. The arrow shows the samples location. (By Foucher (2012)